



UNIVERSITY OF TRENTO - Italy
Department CIBIO

International PhD Program in Biomolecular Sciences

**Department of Cellular, Computational
and Integrative Biology – CIBIO**

XXXII Cycle

**Exploring DHX30, an RNA helicase that coordinates cytoplasmic
translation and mitochondrial function contributing to cancer cell
survival**

Tutor

Alberto Inga

Laboratory of Transcriptional Networks

Ph.D. Thesis of

Bartolomeo Bosco

Laboratory of Transcriptional Networks

Academic Year 2018-2019

Original authorship:

Declaration:

I Bartolomeo Bosco confirm that this is my own work and the use of all material from other sources has been properly and fully acknowledged.

Trento, 15/09/2020

A handwritten signature in dark ink, appearing to read 'Bartolomeo Bosco', written in a cursive style.

ACKNOWLEDGEMENTS

First of all, I thank Professor Alberto Inga for his help in all experiments of this work. Furthermore, he gets me in touch with other groups abroad from Italy, collaborating with them on different projects, resulted in publications. He was very kind, patient, and always available to help me in and out of the working environment, teaching me a lot of notions on cancer and p53, making this Ph.D. period very helpful for my future career in academic research. He is the best supervisor that a Ph.D. student could wish.

I want to thank Erik Dassi, Annalisa Rossi, and Dario Rizzotto for their help in some important experiments of this thesis and their collaboration and helpful discussions.

Next, I thank my bachelor students Nicoletta Di Bernardo, Alicia Perzoli, and Sebastiano Giorgetta for their technical assistance in some experiments and for making their period in the lab very funny.

Thanks to all CIBIO facilities, in particular, the High-Throughput Screening facility team for their support in several important experiments.

Then I want to say a special thank to the Nuclear Domains and Pathologies laboratory in Cancer Research Center of Lyon, in particular to professor Jean-Jacques Diaz, Dr. Frédéric Catez, and Angeline Gaucherot for hosting me in the laboratory, thought me important notions on translation and helped me in some important experiments. Even if the time that I spent there was short, they made me feel like I was at home.

A special thanks go to professor Lucilia Saraiva and the team of the Drug Discovery & Development Research Unit to allow us to collaborate with them on important projects. In particular thanks to Helena Ramos, a very kind heart friend to make me happy with her merrily and kindly presence.

Finally, thanks to my family for supporting me in every aspect of my life and because it is thanks to them that I have become the man that I am; thanks also to all my friends (old and new) for all the funny moments (...and all fatty dinners!) spent together.

Last but first for importance, the bigger thanks go to my girlfriend Giulia, whom I met at the beginning of my Ph.D. and accompanied me in every moment until now, making it the best period of my life. In my opinion, the doctorate is very useful because give us an idea of which future we want to undertake, both in working and non-working terms; I learned two things: the first is that I want to continue with academic career becoming a scientist known all over the world; the second is that I

want to spend all my life, success, and failures, with Giulia, a very special person, and a great scientist.

This work was supported and financed by the Italian Association for Cancer Research (Fondazione AIRC).

CONTENTS

Exploring DHX30, an RNA helicase that coordinates cytoplasmic translation and mitochondrial function contributing to cancer cell survival

List of Tables	8
List of Figures.....	9
Thesis structure.....	15
Abstract.....	16

Chapter 1: Introduction

1.1	Cancer epidemiology.....	18
1.2	Hallmarks of cancer.....	19
1.3	TP53: 40 years of study.....	21
1.3.1	The p53 function in repairable stress conditions.....	24
1.3.2	The p53 function in irreparable stress conditions.....	25
1.3.3	Uncanonical role of p53 in translational control.....	26
1.3.3.1	p53 in post-transcriptional control: miRNAs and lncRNAs.....	27
1.3.3.2	p53 in post-transcriptional control: Ribosome biogenesis.....	29
1.3.3.3	p53 in post-transcriptional control: Ribosome assembly.....	29
1.3.3.4	p53 in post-transcriptional control: RNA-binding-proteins.....	30
1.4	DExH-Box Helicase (DHX) proteins.....	31
1.4.1	DHX30: The protagonist of our story.....	32
1.5	Aim of the thesis.....	33

Chapter 2: Materials and Methods

2.1	Human cell lines and growth conditions.....	35
2.2	RNA-Seq data analysis.....	36
2.3	Western blot.....	36
2.4	Translation assays.....	37
2.4.1	Polysome profiling.....	37

2.4.2	Ribosomes isolation.....	38
2.4.3	Global translation.....	38
2.4.4	Fluorescent In Situ Hybridization on rRNA.....	39
2.4.5	rRNA biogenesis.....	40
2.5	Cell proliferation analysis.....	41
2.5.1	Colony formation.....	41
2.5.2	Cell count.....	41
2.5.3	Real-Time Cell Analysis (RTCA).....	41
2.5.4	Spheroid formation assay.....	41
2.6	Immunofluorescence.....	42
2.7	Cell metabolism assays.....	43
2.7.1	XFp Seahorse analyzer: Compensatory glycolysis test.....	43
2.8	RNA extraction and RT-qPCR.....	43
2.9	Droplet digital PCR.....	45
2.10	RNA immunoprecipitation.....	45
2.11	Cytoplasm-mitochondria fractionation.....	46
2.12	Flow cytometry apoptosis analysis.....	47
2.13	Exploration of TGCA data using the GEPIA web resource...	47
2.13	Statistical analyses.....	47

Chapter 3: Results

3.1	Silencing of DHX30 enhances translation in the HCT116 colorectal cancer cell line.....	48
3.2	DHX30 silencing negatively impacts on the expression of nuclear encoded mit-ribosome components.....	51
3.2.1	Impact of cytoplasmic and mitochondrial DHX30 variants on the expression of mito-ribosome components in HCT116 p53 ^{+/+} and p53 ^{-/-}	52
3.3	Impact of cytoplasmic and mitochondrial DHX30 variants on the expression of oxidative phosphorylation (OXPHOS) components.....	57

3.4	Silencing of DHX30 impaires cell proliferation rate and increases apoptosis proneness.....	61
3.5	Impact of DHX30 depletion in other cell line models.....	63
3.6	Expression of DHX30 in human tissues and prognostic significance in human cancer.....	66

Chapter 4: Discussion and future perspectives..... 71

References..... 76

Appendix..... 87

Secondary projects

- *SLMP53-2 Restores Wild-Type-like Function to Mutant p53 through Hsp70: Promising Activity in Hepatocellular Carcinoma.*
- *MANIO: Mechanism of wild-type and mutant p53 activation and therapeutic potential in colorectal cancer.*

Other publications..... 125

List of Tables

Table 1.1: cancer death in the European Union: number of people who died in 2016 in European Union due to cancer (https://ec.europa.eu/eurostat/statisticsexplained/index.php?title=Cancer_statistics#Deaths_from_cancer)

Table 2.1: siRNAs used to silence DHX30 variants in HCT116 cells and their sequences.

Table 2.2: Primary and secondary antibodies used in immunoblots performed.

Table 2.3: Probes used to hybridize and visualize 28S and 18S rRNA. Probes sequences and conjugated fluorophores are reported.

Table 2.4: List of primary and secondary antibodies with the dilutions used in immunofluorescence experiments.

Table 2.5: Compounds preparation for loading into the ports of sensor cartridge. In the table are reported the stock concentrations and volumes of drugs used to perform the Seahorse glycolytic rate assay program.

Table 2.6: List of primers and their sequence used in RT-qPCR experiments.

List of Figures

Figure 1.1: Estimated incidence and mortality of different types of tumors worldwide in 2018 [Pie charts derived from GLOBOCAN 2018 (<https://gco.iarc.fr/today/online-analysis>)].

Figure 1.2: Tumor microenvironment, cells that compose it and processes in which they are implicated (by Butturini E *et al.*, 2019).

Figure 1.3: p53 pathway: p53 targets and cellular responses after its activation upon stressor signals (Hao Q *et al.*, 2014).

Figure 1.4: p53 protein structure, its domains and their length: the p53 structure comprises two transcriptional activating domains (TAD1 and TAD2), a proline-rich domain, a DNA-binding domain, an oligomerization domain and a regulatory domain (Millau JF *et al.*, 2009).

Figure 1.5: p53 pathway in repairable stress response: upon DNA damage p53 is able to activate different factors able to inhibit cell cycle and activate DNA repair systems (adapted by Subramanian M *et al.*, 2013).

Figure 1.6: p53 pathway in irreparable stress response: p53 is able to activate pathways that trigger apoptosis upon severe and irreparable cellular damage (George P, 2014).

Figure 1.7: Role of p53 in translational control: Translation is regulated by several *cis*- and *trans*- acting elements and some of them, such as miRNA, lncRNA, ribosome biogenesis and others could be regulated by p53 (Marcel V *et al.*, 2015).

Figure 2.1: Example of AHA click-it chemistry reaction to analyse cellular global translation.

Figure 2.2: Example of 5-EU assay procedure to analyse cellular rRNA biogenesis.

Figure 3.1: Bio-informatic analysis of RNA sequencing data. a) Most significant terms by Gene Set Enrichment Analysis (GSEA) along with the number of modulated genes (leading edge) in each pathway. **b)** Translation Efficiency (TE) was calculated from the RNA-seq normalized read counts obtained in polysomal over total RNA. Presented is the data for ribosome and mito-ribosome components, grouped by large or small subunits and for HCT116 control or DHX30 stably depleted clones, as indicated. * $p < 0.05$; *** $p < 0.001$.

Figure 3.2: Amount of cytoplasmic ribosome in HCT116_shDHX30 and HCT116_shNT. Data are normalized on shNT control cells and are mean \pm SD (n=3); * $p < 0.05$.

Figure 3.3: rRNA production in HCT116_shDHX30. **a)** Amount of ribosomal RNA based on 5-EU incorporated in nascent rRNA in the nucleoli revealed by click-it chemistry reaction. Data are mean \pm SD (n=3); *p < 0.05 **b)** (Left) Representative images of one of three independent experiments of FISH for the 18S rRNA. (Right) Box plot of 18S rRNA intensity Data are mean \pm SD (n=30 nucleoli in three biological replicates for each cell line); *p < 0.05.

Figure 3.4: Analysis of translation in DHX30-depleted HCT116 cells. **a)** Analysis of AHA click-it chemistry to analyse global translation in HCT116_shDHX30 cells compared to the shNT control clone. 100mM 5-FU was used as positive control. Data are mean \pm SD (n=6 to 9); ***p < 0.005. **b)** (Left) Polysome profiling of HCT_shDHX30 and HCT_shNT, through sucrose-gradient fractionation and revealed by the measurement of absorbance at a wavelength of 260 nm. (Right) Box plot of the relative quantification of the areas under the curve corresponding to polysomes (POL) and ribosomal subunits or 80S monosome (SUB). Mean \pm SD and individual values (n=7) are shown; *p < 0.05. **c)** Western blot to visualize DHX30 in the different fractions of polysome profiling. RPS6, RPL26 and HNRNPA1 were used as controls.

Figure 3.5: DHX30 impacts on nuclear encoded mito-ribosome components. **a)** RNA immunoprecipitation experiments to study the binding of DHX30 to MRPL11 and MRPS22 transcripts [*performed in collaboration with Annalisa Rossi*]. Results obtained with a primary antibody targeting DHX30 (blue) or the IgG control (grey) are plotted relative as % of input. Data are mean and individual points (n=2); **p < 0.01. **b)** Relative mRNA levels of MRPL11 and MRPS22 in HCT116_shDHX30 compared to the shNT control clone. **c)** (Left) Protein levels of MRPL11 and MRPS22. β -Tubulin was used as loading control. Immunoblots represent one of three independent experiments. (Right) MRPL11 and MRPS22 protein quantification in HCT116_shDHX30 normalized on shNT control clone. In all experiments data are mean \pm SD (n=3); *p < 0.05; **p < 0.01; ***p < 0.001.

Figure 3.6: DHX30 localization and abundance in cellular compartments. **a)** (Upper panel) Cartoon of mitochondrial and cytoplasmic DHX30 isoforms and their predicted protein masses. (Lower panel) Acetylation of lysine on histone H3 analysis performed by Encode that indicates the presence of active promoters. **b)** Representative images of immunofluorescence to co-localize DHX30 (red) with MT-ATP6 (green). Staining with Hoechst was used to visualise nuclei. **c)** Relative mRNA levels of cytoplasmic DHX30 (cDHX30) and the mitochondrial variant (mDHX30, set to 1). Data are mean \pm SD (n=3); ***p < 0.005. **d)** (Left) Representative western blot of cytoplasm-mitochondria fractionation. One of three independent experiments is shown. (Right) Relative quantification of DHX30 protein levels in cytoplasm and mitochondria normalized on mDHX30.

Figure 3.7: Control of stable and transient silencing in colorectal cancer cell lines. **a)** Relative mRNA levels of cytoplasmic (cDHX30) and mitochondrial (mDHX30) DHX30 transcript variants in HCT116_shDHX30 compared to the shNT control clone. **b)** and **c)** qRT-PCR to verify the transient silencing of DHX30 variants in b) HCT116 and c) HCT116 p53^{-/-}, using primers annealing to: (i) a portion of the

coding sequence that is present in all transcript variants (DHX30); (ii) the first exon specific of cytoplasmic DHX30 (cDHX30) or (iii) the alternative first exon specific of mitochondrial DHX30 (mDHX30). All experiments data are analysed 96 hours post silencing and are mean \pm SD (n=3); *p<0.05; **p < 0.01; ***p < 0.001.

Figure 3.8: Transient silencing of DHX30 confirms the reduction in the expression of mito-ribosome components but only in wild-type p53 cells. a) mRNA and b) representative western blot of MRPL11 and MRPS22 in HCT116 silenced transiently for cytoplasmic DHX30 (HCT_siDHX30-C) or for both cytoplasmic and mitochondrial variants (HCT_siDHX30-C+M). qRT-PCR data are compared to the siRNA negative control (HCT_siNC) and are mean \pm SD (n=3); *p < 0.05. c) mRNA and d) representative western blot of MRPL11 and MRPS22 protein levels in HCT116 p53^{-/-} silenced for cytoplasmic DHX30 (HCT_siDHX30-C) or for both cytoplasmic and mitochondrial variants (HCT_siDHX30-C+M). RT-qPCR data are compared to the siRNA negative control (HCT_siNC) and are mean \pm SD (n=3).

Figura 3.9: DHX30 impacts on the expression of mitochondrially encoded oxidative phosphorylation (OXPHOS) components. a) Relative mitochondrial genome copy number in HCT116_shDHX30 and -shNT measured by droplet digital PCR. MT-RNR1 and MT-ATP8 were amplified along with the nuclear diploid marker gene CTDSP1. Bars plot mean \pm SD (n=3). [*Digital PCR experiments were developed with contributions from Viktoryia Sidarovich and Pamela Gatto, CIBIO HTS core facility*]. b) Scheme of the mammalian mitochondrial genome comprising 13 mitochondrially encoded genes and 2 rRNA and 22 tRNAs (Nissanka N *et al.*, 2018). c) Relative mRNA levels of mitochondrially encoded OXPHOS components in HCT116_shDHX30 compared to HCT116_shNT (dashed line, set to 1). Data are mean \pm SD (n=3); *p < 0.05; **p < 0.01. d) Protein levels of MT-ATP6 and MT-ATP8 in mitochondrial lysates of HCT116_shDHX30 and the shNT control clone. Ponceau-S was used as loading control. Immunoblots represent one of three independent experiments. e) Representative images of one of three independent immunofluorescence experiments to visualize DHX30, MT-ATP8 (red), or MT-ATP6 (green) expression in HCT116_shDHX30 and HCT116_shNT.

Figure 3.10: DHX30 might directly bind mitochondrially encoded transcripts. RNA immunoprecipitation (RIP) experiments, [*performed in collaboration with Annalisa Rossi*], to study the binding of DHX30 to mitochondrially encoded OXPHOS components transcripts with (Left) or without (Right) UV-crosslinking. Results obtained with a primary antibody targeting DHX30 (blue) or the IgG control (grey) are plotted relative to the input (1%, dashed line). Data are mean \pm SD (n=3); **p < 0.01; ***p < 0.001. Evidence of binding was obtained with crosslinking, but not in native conditions.

Figure 3.11: DHX30 depletion reduces mitochondrial respiration but does not lead to compensatory glycolysis in HCT116 cells. (Left) Measurement of the oxygen consumption rate (OCR) to evaluate mitochondrial respiration by Seahorse XF analyzer. Points before the Rotenone/Antimycin-A (Rot/AA) treatment correspond to the basal mitochondrial respiration. (Right) Extracellular acidification

rate measurement was used as a means to measure glycolysis. Points before and after the Rotenone/Antimycin-A (Rot/AA) treatment correspond respectively to basal and compensatory glycolysis -in response to the block of mitochondrial respiration-. 2-Deoxyglucose (2-DG) is then used to block glycolysis. For both panels, one of three independent replicates is presented. Data are mean \pm SD (n=3 wells in the Seahorse cartridge); *p < 0.05.

Figure 3.12: DHX30 depletion decreases the expression of mitochondrially encoded OXPHOS components but only when p53 is expressed. a) and b) Relative mRNA levels of the indicated mitochondrially encoded OXPHOS components in a) HCT116 p53^{+/+} and b) HCT116 p53^{-/-} transiently silenced for DHX30 expression (siDHX30-C, siDHX30-C+M) compared to siNC (dashed line, set to 1). Data are mean \pm SD (n=3); *p < 0.05; **p < 0.01; ***p < 0.001. c) and d) Protein levels of MT-ATP6 and MT-ATP8 in c) HCT116 p53^{+/+} and d) HCT116 p53^{-/-} transiently silenced for DHX30 variants. α -actinin was used as loading control. Immunoblots represent one of three independent experiments.

Figure 3.13: DHX30 depletion impairs cell proliferation and enhances apoptosis upon drug treatments. a) (Left) Representative image of colony formation assays. (Right) Colony quantification by ImageJ software. Data are mean \pm SD (n=3). b) Relative cell proliferation measured by high-content microscopy in digital phase contrast. Data are mean \pm SD (n=3). c) Estimates of relative proliferation by an impedance-based Real-Time Cell Analyser. Data are mean \pm SD (n=3). d) Spheroid formation and growth assay. (Left) A representative image at the indicated time points is shown in the left panel. (Right) Spheroid area measured by ImageJ software. Data are mean \pm SD (n=3). e) (Left) Representative image of HCT116_shNT and shDHX30 cell cycle profile [performed by Dario Rizzotto]. (Right) Quantification of cell cycle profile in HCT116_shDHX30 cells compared to shNT control. Data are mean \pm SD (n=3). f) Relative expression of the Annexin-V apoptosis markers in cells treated for 48 hours with the indicated drugs or DMSO control. For all panels, data are mean \pm SD (n=3); *p < 0.05; **p < 0.01; ***p < 0.001.

Figure 3.14: Efficacy of transient DHX30 silencing in U2OS and MCF7. a) and b) qRT-PCR to verify the transient silencing of DHX30 in a) U2OS and b) MCF7 using primers annealing to: (i) a portion of the coding sequence that is present in all transcript variants (DHX30); (ii) the first exon specific of cytoplasmic DHX30 (cDHX30) or (iii) the alternative first exon specific of mitochondrial DHX30 (mDHX30). Experiments are performed after 96 hours post silencing and data are mean \pm SD (n=3); *p < 0.05; **p < 0.01; ***p < 0.001.

Figure 3.15: The effect of DHX30 depletion on nuclear encoded mitoribosome components in MCF7 and U2OS. a) and b) qRT-PCR of MRPL11 and MRPS22 in a) U2OS and b) MCF7 cells transiently silenced for cytoplasmic DHX30 (siDHX30-C) or for both cytoplasmic and mitochondrial variants (siDHX30-C+M). Data are compared to the siRNA negative control (siNC) and are mean \pm SD (n=3); **p < 0.01. c) (Upper panel) representative western blot of MRPL11 and MRPS22 in U2OS silenced transiently as in a). (Lower panel) Relative protein quantification of nuclear

encoded mitoribosome components in U2OS transiently silenced for DHX30. Data are mean \pm SD (n=3); **p < 0.01. **d**) (Upper panel) representative western blot of MRPL11 and MRPS22 in MCF7 silenced transiently for both cytoplasmic and mitochondrial variants (MCF7_siDHX30-C+M). (Lower panel) Relative protein quantification of nuclear encoded mitoribosome components in MCF7 transiently silenced for DHX30. Data are mean \pm SD (n=3); *p < 0.05.

Figure 3.16: The effect of DHX30 depletion on mitochondrially encoded OXPHOS components in MCF7 and U2OS. **a**) and **b**) qRT-PCR of selected mitochondrially encoded genes in a) U2OS and b) MCF7 cells transiently silenced for cytoplasmic DHX30 (siDHX30-C) or for both cytoplasmic and mitochondrial variants (siDHX30-C+M). Data are compared to the siRNA negative control (siNC) and are mean \pm SD (n=3); *p < 0.05; ***p < 0.005. **c**) (Up) representative western blot of MT-ATP6 in U2OS transiently silenced as in a). (Down) Relative protein quantification of MT-ATP6 in U2OS. Data are mean \pm SD (n=3). **d**) (Up) representative western blot of MT-ATP6 in MCF7 transiently silenced for both cytoplasmic and mitochondrial variants (MCF7_siDHX30-C+M). (Down) Relative protein quantification of MT-ATP6. Data are mean \pm SD (n=3).

Figure 3.17: Impact of DHX30 depletion in U2OS and MCF7. **a**) and **b**) Relative cell proliferation measured by high-content microscopy in digital phase contrast in a) U2OS and b) MCF7 transiently silenced for DHX30 variants. Data are mean \pm SD (n=3); *p < 0.05.

Figure 3.18: DHX30 expression in human tissues. DHX30 protein expression data is shown for 44 human tissues. Color-coding is based on tissue groups. Data obtained from the protein atlas web resource.

Figure 3.19: The percentage of DHX30 tumor positive patients correlates with DHX30 expression in tissues. Percentage of patients (maximum 12) with high or medium DHX30 expression. Cancer types are color-coded according to which type of normal organ the cancer originates from. Data obtained from the protein atlas web resource.

Figure 3.20: Prognostic value of a gene signature comprising DHX30 and its target mitoribosome transcripts. See also Figure 3.21. TCGA data was interrogated through the Gepia web resource to evaluate the correlation between the expression of DHX30 and that of 14 mitoribosomal transcripts that are predicted are direct targets. Presented are two examples among a cluster of eleven cancer types where a positive correlation is apparent. See Figure 3.21 for the complete data and additional examples. **a**) Adrenocortical Carcinomas (ACC). **b**) Liver Hepatocellular Carcinomas (LIHC). Left panels, Pearson correlation; right panels, Overall Survival Kaplan-Meier. The correlation value, the Hazard Ratio, p values and sample sizes are shown.

Figure 3.21: DHX30 expression positively correlates with the expression of mitoribosomal protein transcripts and can have prognostic significance. **a**) Pearson correlations between the expression of DHX30 and of each mitoribosomal

protein transcripts in cancer samples. Data was extracted from the Gepia web server. Unsupervised clustering revealed two major clusters based on the level of gene expression correlation and two main clusters among cancer types. Boxed in red are the names of the fourteen transcripts that are candidate DHX30 direct targets **b)** The expression correlation data (R value and p value) between DHX30 and the combined group of 14 mitoribosomal protein transcripts is listed for each cancer type presented in the same order as for panel a). Data from Kaplan-Meier outcome analysis for the aggregated 15-gene signature (DHX30 + the 14 mitoribosomal protein transcripts). Significant differences are highlighted in bold font. **c)**, **d)** Correlation and Overall Survival Kaplan-Meier curves for two negative examples from cluster 2; colon adenocarcinoma (COAD); breast cancer (BRCA). As for panel b), Hazard Ratio for the high expression group, and p values, and sample size are indicated.

Figure 4.1: Graphical scheme of the DHX30 functions inferred by the results in this thesis. DHX30 depletion by short hairpin or siRNA reduces mitoribosome biogenesis as well as OXPHOS components expression in mitochondria; in contrast it enhances ribosome biogenesis and global translation in the cytoplasm. Those phenomena cause a reduction in proliferation and are associated with higher apoptosis proneness upon p53-activation or the treatment with mitochondrial damaging agents.

Thesis structure

This work focuses on an RNA-binding protein (RBP) called DHX30. The first chapter of my PhD thesis is an introduction that starts from a general overview on cancer epidemiology and hallmarks, before presenting p53 as a critical transcription factor for cellular stress responses. Then, I briefly reviewed the more recent discovery of a role of p53 in translation control and its links with RNA-binding proteins. I continued the chapter with an introduction of DExH-Box RNA Helicases, and a review of what is known about DHX30, and closed it by stating the aims of the PhD project.

Chapter 2 contains all molecular and phenotypic analysis and methods used in this work.

In chapter 3, I present the results acquired during my PhD. Starting with bio-informatic analysis based RNA-seq data, performed in a previous study, followed by the investigation of the role of DHX30 in cell translation and mitochondrial energy regulation in cancer cell line models. At the end of this chapter, I explored phenotypic responses regulated by DHX30, such as constitutive cell proliferation and apoptosis upon cancer treatments.

Chapter 4 contains the discussion of all results obtained, a summary of the mechanism proposed and future perspectives.

I finished the thesis with references and an appendix containing my publications. In particular, the appendix is divided in two parts: in the first I highlighted my contributions to a publication, and I also present my contributions to a second publication that is in preparation. Both studies contain some aspects that are complementary to the topic of my PhD thesis. In the second part of the appendix I included only the references to three other publications I contributed to.

Abstract

Many recent studies established a potential role for p53 in translational control of many transcripts through the modulation of the expression of several microRNAs, RNA binding proteins (RBPs), translation factors, or of ribosome biogenesis factors. To establish the relevance of translation control in p53-dependent apoptosis our group recently compared by polysome profiling two cell lines, SJS1 and HCT116, undergoing respectively p53-dependent apoptosis and cell cycle arrest in response to the treatment with Nutlin-3, a selective activator of p53. Examining the markedly different, treatment-induced translation landscapes, the RNA helicase DHX30 was identified as a protein able to bind only in HCT116 cells to a 3'-UTR sequence motif, labeled as CGPD-motif. The motif had been identified as highly over-represented among translationally enhanced mRNAs in nutlin-treated SJS1 cells, among which apoptosis effectors were enriched. Since the binding of DHX30 to the CGPD-motif transcripts is observed in cell cycle arresting HCT116, where those mRNA are not translationally enhanced, we reasoned that DHX30 could be part of an RBP complex responsible for reduced translation of specific pro-apoptotic mRNAs. To pursue this hypothesis, HCT116-shDHX30 clones were obtained and I studied the functions of this relatively unknown RNA helicase in this and other cell models. A translome analysis by RNA-seq of HCT116-shDHX30 cells showed higher activation of ribosome biogenesis pathways, according to GSEA. Consistently, eCLIP data from ENCODE indicate that DHX30 can bind to most ribosomal protein transcripts, and those showed higher relative translation efficiency in HCT116-shDHX30 cells. In fact, the cells exhibited increased rRNA synthesis and higher global translation as well as a large expansion of the number of transcripts showing higher polysome-association in response to Nutlin. The DHX30 gene features two promoters, one of which can produce a transcript containing a mitochondrial localization signal. I confirmed that DHX30 has both a cytoplasmic and a mitochondrial localization by both cell fractionation and immunofluorescence. HCT116_shDHX30 cells have reduced mitochondrial metabolism, based on oxygen consumption rates but do not show evidence of compensatory glycolytic activity. Impaired mitochondrial functions could be related also to decreased expression of mitochondrial oxidative phosphorylation (OXPHOS) components as well as reduced expression of nuclear encoded mitoribosome proteins. Based on RIP assays DHX30 appears to target

directly mitoribosome transcripts. Depletion of DHX30 showed reduced proliferation in various assays both in 2D and 3D culture conditions and sensitized cells to the treatment with the mitochondrial uncoupler FCCP. A similar role was observed also on mitochondrially encoded OXPHOS components as well as mitoribosome components in MCF7 breast cancer cell line silenced for DHX30 with a consistent reduction in cell proliferation. In contrast, U2OS osteosarcoma cells did not show a change in the expression in mitochondrial components as well as an impact on proliferation after transient DHX30 silencing. Hence, it appears that DHX30 can exert a broad general control on cell metabolism and translation as well as a cis-element mediated control of the translation of specific mRNAs impacting both on cell fitness and apoptosis.

Chapter 1: Introduction

1.1 Cancer epidemiology

Cancer is one of the highest causes of death worldwide, particularly in developed countries. In fact, in 2018, 18.1 million new cancer cases were estimated, with a mortality of about 53% (<https://gco.iarc.fr/>). For example, only in the European Union, 1.3 million people died from cancer in 2016 with a slightly higher percentage among men (29.2%) than among women (22.9%) (**Table 1.1**).

	Number of deaths (number)	Share of all deaths			Standardised death rates (per 100 000 inhabitants)				
		Total	Males	Females	Total	Males	Females	Persons aged < 65 years	Persons aged ≥ 65 years
		(%)							
EU-28	1 334 772	26.0	29.2	22.9	259.5	343.3	200.5	76.2	1 016.2
Belgium	27 239	25.4	28.8	22.0	246.5	326.3	190.5	68.4	981.8
Bulgaria	17 235	16.2	18.0	14.2	232.1	318.0	172.2	97.1	789.1
Czechia	27 276	25.4	27.6	23.1	277.0	370.3	214.8	77.1	1 102.3
Denmark	15 780	30.0	31.3	28.7	293.5	349.5	255.4	72.2	1 207.3
Germany	231 068	25.3	27.8	22.8	253.2	324.0	204.1	71.5	1 003.4
Estonia	3 762	24.6	27.2	22.1	287.6	448.5	210.2	85.3	1 122.6
Ireland	9 170	29.9	30.7	29.0	277.2	328.9	240.4	64.3	1 156.4
Greece	30 014	25.4	29.9	20.7	249.5	338.3	178.7	74.1	973.4
Spain	108 510	26.6	31.9	21.0	229.8	329.7	155.3	69.7	890.9
France	163 919	27.6	31.5	23.8	243.8	332.4	180.3	77.4	930.8
Croatia	14 081	27.3	31.9	22.8	333.9	477.5	240.7	101.6	1 292.7
Italy	169 714	27.6	32.1	23.5	241.0	321.0	185.0	62.5	978.0
Cyprus	1 274	23.3	25.7	20.5	193.7	254.7	145.6	47.8	796.1
Latvia	5 903	20.9	23.6	18.4	294.6	466.1	211.7	97.2	1 109.3
Lithuania	8 144	20.0	22.4	17.7	280.5	438.7	197.0	104.2	1 008.5
Luxembourg	1 076	27.1	30.5	23.5	235.5	314.4	179.6	64.7	940.3
Hungary	32 971	26.0	28.8	23.2	345.3	478.1	262.2	132.4	1 224.6
Malta	928	27.8	30.5	25.1	220.7	269.8	184.9	64.7	864.9
Netherlands	45 397	30.7	34.4	27.2	285.1	358.2	236.0	73.9	1 156.8
Austria	20 214	25.4	28.2	22.9	237.2	302.7	192.8	65.8	944.7
Poland	100 025	25.7	27.2	24.0	297.4	417.1	224.4	94.6	1 134.7
Portugal	27 344	24.7	29.3	20.1	245.8	356.0	168.8	79.8	931.0
Romania	51 598	20.2	22.9	17.3	277.0	386.4	197.9	117.2	936.9
Slovenia	6 275	32.0	36.7	27.4	308.5	436.3	228.6	78.3	1 259.0
Slovakia	13 716	26.3	28.9	23.6	315.1	448.9	233.3	95.6	1 221.2
Finland	12 489	23.2	24.9	21.6	219.7	282.6	179.4	54.1	903.4
Sweden	22 550	24.9	26.9	23.1	229.4	275.0	198.9	50.8	966.7
United Kingdom	167 100	27.8	30.1	25.6	275.4	334.9	233.1	67.4	1 133.8
Iceland	671	29.3	29.2	29.4	269.8	304.1	245.3	58.9	1 140.2
Liechtenstein	66	25.4	22.6	28.3	197.4	204.4	194.1	49.5	807.8
Norway	10 869	27.0	29.7	24.4	242.7	299.1	205.9	55.6	1 015.2
Switzerland	17 256	26.6	30.2	23.3	216.2	277.6	174.5	53.1	889.9
Serbia	21 540	21.4	24.2	18.5	298.5	387.7	232.4	118.3	1 042.7
Turkey	78 899	19.2	23.0	14.7	198.3	294.4	124.8	65.2	747.6

Table 1.1: Number of cancer death in European Union: Number of people died in 2016 in European Union due to cancers (https://ec.europa.eu/eurostat/statisticsexplained/index.php?title=Cancer_statistics#Deaths_from_cancer)

Among all types of cancers, lung, breast, and colorectal are the three most common, with an incidence of 11.6%, 11.6%, and 10.2% respectively. In particular, lung and colorectal cancers are associated with the highest mortality in the world, mostly because of their aggressiveness, invasion capacity, and treatment resistance (**Figure 1.1**) (Ferlay J *et al*, 2012). In this study, we focused our attention on a colorectal cancer cell model. Colorectal cancer develops in the colon or rectum, causing the presence of blood in the stool, changes in bowel movements, weight loss, and

persistent tiredness (www.cancer.gov). As for the majority of tumors, the main risk factors include aging, diet, alcohol, and smoking (Watson AJM *et al*, 2011).

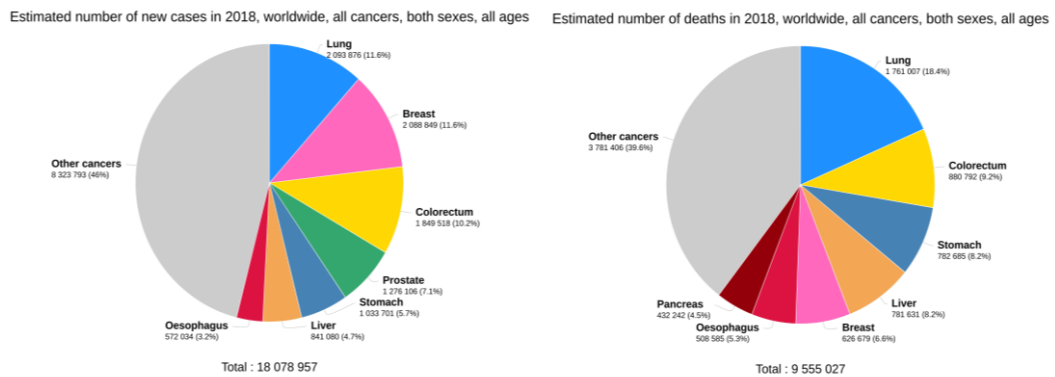


Figure 1.1: Estimated incidence and mortality of different types of tumor worldwide in 2018 [Pie charts derived from GLOBOCAN 2018 (<https://gco.iarc.fr/today/online-analysis>)]

Moreover, people affected by inflammatory bowel disease have a higher risk of colon cancer directly proportional to the severity of inflammation (Jewad N *et al*, 2011).

Most colorectal cancer diagnoses are done through colonoscopy or sigmoidoscopy, sampling of areas of the colon suspicious for possible tumor development (Cunningham D *et al*, 2010), while treatments include surgery, chemotherapy, or radiotherapy, depending on the stage of tumor development. In detail, in colon cancer stage I and II, surgery is the most used treatment, while in stage III and IV chemotherapeutic agents like Fluorouracil, Capecitabine, Irinotecan and Oxaliplatin are used, sometimes together with radiotherapy. Unfortunately, when colorectal cancer is found at late stages, treatment is often palliation, to relieve symptoms caused by the tumor and keep the person as comfortable as possible (Cunningham *et al*, 2010).

1.2 Hallmarks of cancer

Nowadays it is known that cancer is not a simple mass of proliferating cells, but a very complex tissue composed by distinct cell types involved in interactions between them and evolving a “tumor microenvironment” (Hanahan D *et al*, 2011). One of the deeply studied hallmarks of cancer is the upregulation of angiogenesis. Usually, in humans, angiogenesis is largely quiescent except for processes like wound healing and female reproductive cycling in which it turns on, but only transiently. In contrast,

a form of pathological angiogenesis is activated in tumors, causing the development of new vessels able to sustain cancer cells with nutrients and oxygen and remove wastes and carbon dioxide (**Figure 1.2**), thus increasing neoplastic growth.

Cancer stem cells are important components of the tumor mass (Hanahan D *et al*, 2011; **Figure 1.2**). Like stem cells, they have the ability to efficiently seed new tumors for example upon inoculation in mice, and these secondary tumors show similar features of the primary, as revealed for example by transcriptional profiles (Cho RW *et al*, 2008). Cancer stem cells are responsible for cancer initiation, are essential for progression, contribute to cancer heterogeneity, resistance to treatments, and recurrence (Singh A *et al*, 2010).

Another important component of the tumor microenvironment is represented by cells derived from the immune system that have different functions (**Figure 1.2**). In detail, they can inhibit tumor progressions, such as Natural Killer cells (NK) and cytotoxic T lymphocytes (CTLs), or promote its progressions, such as some macrophages, mast cells, neutrophils, and T and B lymphocytes.

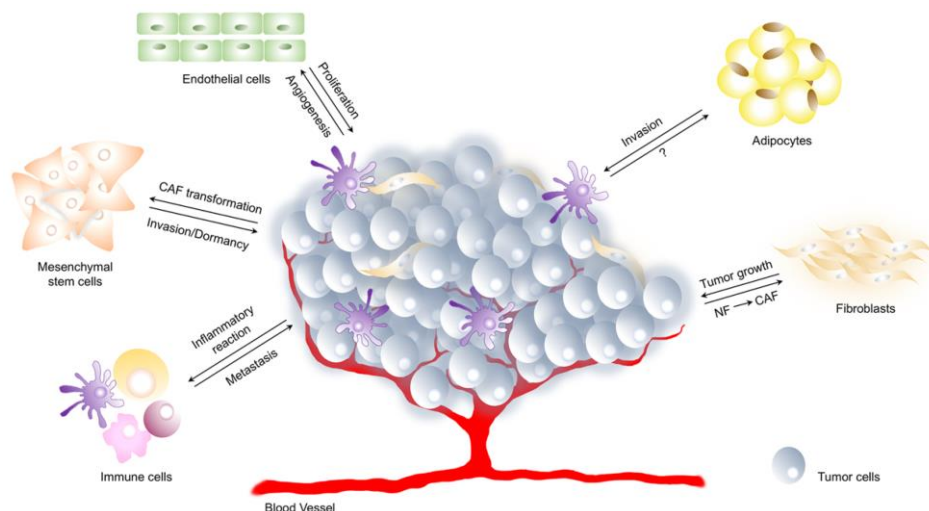


Figure 1.2: Tumor microenvironment, cells that compose it and processes in which they are implicated (by Butturini E *et al*, 2019)

Moreover, the inflammatory state promotes the presence in the tumor microenvironment of several signaling molecules released by inflammatory cells, stromal cells, and cancer cells, such as Epidermal Growth Factor (EGF), Vascular Epithelial Growth Factor (VEGF), chemokines, cytokines, and other pro-invasive enzymes that enhance tumor angiogenesis, proliferation, invasion and metastasis (Hanahan D *et al*, 2011; DeNardo DG *et al*, 2010).

Many years of discoveries on tumor biology led to the formalization of specific acquired features, defined as the eight hallmarks and enabling characteristics of

cancer: 1) Genome instability and mutations; 2) reprogramming of anti-tumor immune cells into tumor-promoting ones that secrete pro-survival, pro-migration, and anti-detection factors, allowing tumor growth and metastasis; 3) hyper-active signaling to sustain a chronic proliferation; 4) growth suppressors evasion, including TGF-beta but also TP53, one of the most important tumor suppressor genes; 5) apoptosis or necrosis inhibition or down-regulation; 6) replicative immortality by telomerase over-expression and the abolishment of senescence; 7) angiogenesis induction and 8) invasion and metastasis activation by modulation of cadherins and integrins, matrix metalloproteases and other molecules able to regulate cell-to-cell and cell-to-matrix interactions and cell migration (Figure 1.3; Hanahan D *et al*, 2011). In 2011, two other emerging hallmarks were included: 7) the deregulation of cell energy production, through cell metabolism modifications, both glycolytic and mitochondrial, to most effectively support neoplastic proliferation; and 8) the avoidance of immune destruction by “hiding” epitopes that could be recognized by, for example, NK cells or CTLs (Figure 1.3; Hanahan D *et al*, 2011).

1.3 TP53: 40 years of study

One of the most important proteins that plays a crucial tumor-suppressive role in the majority of cancer types is p53. This transcription factor was discovered 41 years ago in a protein complex with the simian virus 40 (SV40) large T-antigen in murine embryonal carcinoma cells, but the homologous protein was found also in other species such as hamster, monkey and human (Linzer DIH *et al*, 1979; Lane DP *et al*, 1979). Only in the following years, the importance of p53 was determined. Initially, it was classified as an oncogene, due to the high levels of expression in tumors (DeLeo AB *et al*, 1979) and the capacity of the first cloned cDNA to promote immortalization when overexpressed in cultured cells. In the following years, a very important role of this protein as a tumor-suppressor was revealed. In fact, the original p53 clone was discovered to be a mutated form, the gene was shown to be frequently mutated in human cancer, and a cancer predisposition syndrome associated with germline p53 mutations was discovered (Levine AJ *et al*, 2009; Freed-Pastor WA *et al*, 2012). Indeed, the wild type form of p53 was shown to inhibit cancer cell proliferation, inducing cell cycle arrest and apoptosis, and the p53 protein function was shown to be finely tuned and modulated, for example in response to DNA damage or other stressful situations for proliferating cells (Harris LH *et al*, 2005). Indeed p53, which

started to be called “*the guardian of the genome*” from 1992, is a transcription factor able to induce the transcription of many genes controlling and preventing malignant transformation or, in case of severe cellular damage, activating apoptosis. p53 can be activated by many stresses such as DNA damage, hypoxia, oxidative stress, nutrient deprivation, telomere erosion, and ribosomal stress (**Figure 1.3**) (Hao Q *et al*, 2014).

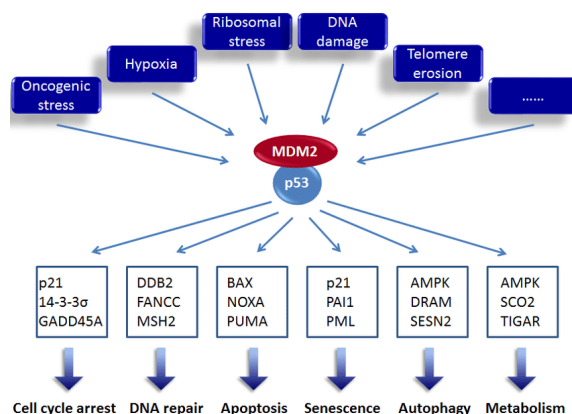


Figure 1.3: p53 pathway: p53 targets and cellular responses after its activation upon stressor signals (Hao Q *et al.*, 2014)

In normal condition p53 is bound by Mouse Double Minute 2 (MDM2), an E3 ubiquitin-protein ligase that ubiquitinates itself and p53 facilitating its degradation mediated by the proteasome. Cellular stresses activate this pathway starting from the phosphorylation in multiple sites of both MDM2 and p53 that change their conformational structure, binding affinity, and result in p53 protein stabilization. But the control of p53 mediated by MDM2 is a very elegant example of regulation because these two proteins are members of a negative feedback control loop. Indeed, when p53 is activated, the transcription of MDM2 is also induced, resulting in higher levels that normalize the level of p53 back to a physiological condition. p53 undergoes also different post-translation modifications such as acetylation, methylation, phosphorylation, and sumoylation able to increase its half-life, from 6-20 minutes to hours, and concentration, by 3-10 fold (Huun J *et al.*, 2017).

p53 protein is composed by 393 amino acids (a.a.) divided in different functional domains: two N-terminal transcriptional activating domains TAD1 (1-42 a.a.) and TAD2 (43-63 a.a.), a proline-rich domain (64-97 a.a.), a DNA-binding domain (102-292 a.a.), an oligomerization domain (323-356 a.a.), and a basic or regulatory domain (363-393 a.a.) (**Figure 1.4**; Millau JF *et al*, 2009).

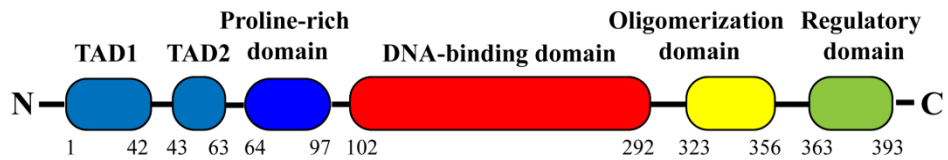


Figure 1.4: p53 protein structure, its domains their length: the p53 structure comprises two transcriptional activating domains (TAD1 and TAD2), a proline-rich domain, a DNA-binding domain, an oligomerization domain and a regulatory domain (Millau JF *et al.*, 2009).

The TADs regulate p53 activity through the interaction with regulatory proteins such as MDM2 (Momand J *et al.*, 1992), and with acetyltransferases, such as p300 and CREB-binding protein (CBP) (Harris SL *et al.*, 2005). The proline-rich domain seems to also have an important role in the regulation of p53 activity, sustaining the binding between MDM2 with the transcriptional activating domains. Moreover, it has been observed that p53 truncated of this domain showed increase sensitivity to MDM2-dependent degradation and decreased transactivation capacity, associated with a reduction in cell cycle arrest and apoptosis response (Toledo F *et al.*, 2006). The p53 central core is the DNA-binding domain, a highly conserved region that specifically binds double-strand target DNA, enabling the transcriptional modulation of many target genes. The majority of missense mutations that affect p53 function in cancer cells are in this region. Those mutations produce a protein that fails to activate transcription of its target genes, removing a major tumor-suppressive function (Harris SL *et al.*, 2005; Hao Q *et al.*, 2014). Based on x-ray crystallography and NMR, it was found that the p53 structure is organized in tetramers in a reversible equilibrium with unfolded form. This tetrameric structure is known to be the most active transcriptional form of p53 and an essential role is played by the oligomerization domain in C-terminal that allows this conformation (Jeffrey PD *et al.*, 1995; Veprintsev DB *et al.*, 2006). Finally, the regulatory domain (consisting of a lysine-rich region) is the site in which many post-translational modifications that positively or negatively regulate p53 activity occurs (Huun J *et al.*, 2017).

When activated, p53 enters into the nucleus where it can perform its transcription factor role, binding the target gene promoters and activating their transcription. The elements that allow the p53 nuclear/cytosolic shuttling are three Nuclear Localization Signals (NLS), present at the C-terminal, and two Nuclear Export Signals (NES), one

localized at TAD1 and other at C-terminal (Liang SH *et al.*, 1999; Stommel JM *et al.*, 1999).

1.3.1 The p53 function in repairable stress conditions.

Under low-stress conditions, the cell tends to activate cell cycle arrest and DNA repair machinery. The inhibition of cell cycle progression can be controlled by p53 and, in fact, it is one of its most important functions.

The cell cycle is a highly regulated process divided in four phases: Gap1 (G1), Synthesis (S), Gap2 (G2), and Mitosis (M). The entire process allows coordination between cell growth, DNA replication, faithful chromosome segregation, and cell division. To avoid the occurrence and the transmission of DNA errors, the cell cycle is regulated by three main checkpoints: one between G1 and S phases, another in S phase, and the last one between G2 and M phases. They are regulated by modulators of the Cyclin-Dependent Kinase complexes (CDKs), whose enzyme activity is controlled by the respective cyclins, and by kinases activated by DNA damage, such as ATM, ATR, DNAPK, CHK1, CHK2 (Nurse P *et al.*, 2000).

Acting upstream of CDKs, p53 can induce either G1 or G2/M arrest, depending on the type of cellular stress. In detail, p53 as a transcription factor promotes the transcription of the CDKN1A gene, which encodes p21. This protein binds cyclin E/CDK2 and cyclin D/CDK4/6 complexes, inhibiting phosphorylation of a critical cell cycle regulator called the retinoblastoma protein (Rb), and the subsequent cell cycle progression into the S phase (Adams PD *et al.*, 1996; El-Deiry, 1998). p21 has also an important role in p53-mediated G2/M arrest. Indeed, this protein can interact with cyclin B/CDK1 complex, blocking the phosphorylation and subsequent activation of CDK1 (Smits VA *et al.*, 2000).

Moreover, included among the many targets of p53 are Growth Arrest and DNA Damage inducible 45 (GADD45) and 14-3-3 σ that, like p21, arrest cell cycle in the G2/M phase acting on cyclin B/CDK1 complex. In particular, GADD45 binds CDK1, inhibiting the complex formation with cyclin and its subsequent kinase activity, while high levels of 14-3-3 σ remove the cyclin B/CDK1 from the nucleus, separating this complex from its target proteins (Zhan Q *et al.*, 1999; Hermeking H *et al.*, 1997) **(Figure 1.5).**

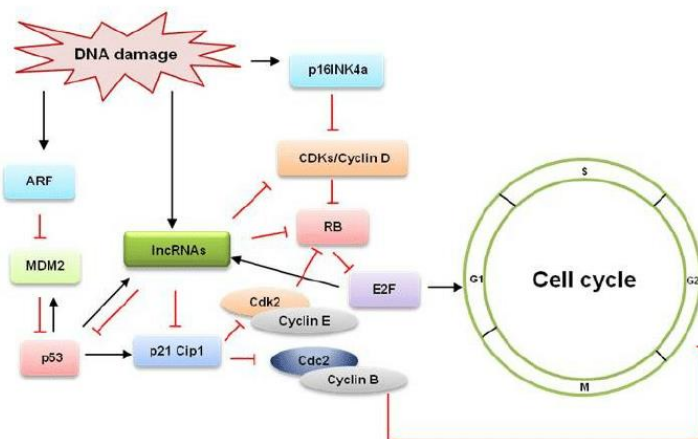


Figure 1.5: p53 pathway in repairable stress response: Upon DNA damage p53 is able to activate different factors able to inhibit cell cycle and activate DNA repair system (adapted by Subramanian M *et al*, 2013)

1.3.2 The p53 function in irreparable stress conditions.

Under severe stress conditions, cells can activate apoptosis, a programmed cell death pathway, or senescence, a permanent cell cycle arrest that can culminate in phagocytosis (Xue W *et al.*, 2015). Apoptosis is divided in two main pathways, the extrinsic and intrinsic, although both converge into the same terminal pathway. The extrinsic pathway starts with the binding of external ligands to a family of so-called death receptors, such as type 1 of tumor necrosis factor receptor (TNFR1), Fas (also called CD95/Apo-1), and TNF-related apoptosis-inducing (TRAIL). These receptors activate caspase 8 cleavage, with the induction of apoptotic events (Guicciardi ME *et al.*, 2009). In contrast, the intrinsic mitochondrial pathway is dependent on intracellular stimuli, like genotoxic stress, and unfolded protein response (Ryan KM, 2011). In detail, BH3 interacting-domain death antagonist (BID), a member of the Bcl-2 family, interacts with another member of the same family called Bax, leading its insertion in the outer mitochondrial membrane. Then, activated BAX and/or BAK play an important role in mitochondria membrane permeability, forming a mitochondrial apoptosis-inducing channel (MAC) that allow for cytochrome c (cyt c) release from this organelle (Dejean LM *et al.*, 2005). The released protein interacts with apoptosis protease-activating factor 1 (Apaf-1), forming a complex called apoptosome that leads to a waterfall of caspases activation, such as caspase-9 and then caspase 3, 6, and 7 (Yip KW *et al.*, 2008) (**Figure 1.6**). At the end of this pathway, chromatin is condensed and fragmented, the membrane is broken and

mitochondria become swelled. The dying cells or cell bodies are finally recognized and engulfed by phagocytosis, and the post-apoptosis process can also be modulated by p53 (Edinger AL *et al.*, 2004). p53 transcriptional activity is essential for triggering extrinsic and intrinsic apoptotic pathways. Indeed, regarding the extrinsic pathway, p53 increases the expression levels of Fas, death receptor 5 (DR5/Killer, a TRAIL receptor), and p53-induced protein with a death receptor domain (PIDD) (Amaral JD *et al.*, 2010).

In the intrinsic apoptotic pathway, p53 increases the expression levels of several proteins of the Bcl-2 family, such as BAX and Bcl-2-antagonist/killer (BAK), together p53 Upregulated Modulators of Apoptosis (PUMA) and NOXA, two important pro-apoptotic targets.

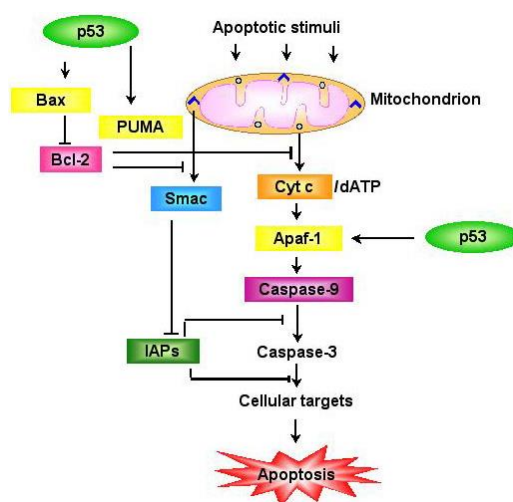


Figure 1.6: p53 pathway in irreparable stress response: p53 is able to activate pathways that trigger apoptosis upon severe and irreparable cellular damage (George P, 2014).

1.3.3 Unconventional role of p53 in post-transcriptional control

For many decades, cancer research has been focused on the modulation of transcriptional programs caused by cancer-promoting proteins to stimulate cell proliferation or by tumor-suppressor genes, to stop cell cycle arrest or induce cell death. The transcriptional network induced by activation of p53 has certainly been one of the most extensively studied (Levine AJ *et al.*, 2009; Freed-Pastor WA *et al.*, 2012). However, it is now clearly established that the deregulation of translation has a key role in cancer development (Silvera D *et al.*, 2010). Translational is one of the last levels of gene expression regulation that allow proteins synthesis by ribosomes. Its control is mediated by both *cis*- and *trans*- regulatory elements well identified.

Included among *cis*-elements are sequence elements in regulatory regions, mainly in untranslated regions (UTRs) of mRNAs, epitranscriptomic modifications in RNA 5'cap such as N⁶-methyladenosine (m⁶A) and N¹-methyladenosine (m¹A), secondary structures of mRNA such as hairpin or internal ribosome entry site (IRES) and *trans*-acting factors binding sites. Instead, *trans*-elements include eukaryotic initiation factors (eIFs), IRES-transactivating factors (ITAFs), microRNAs (miRNAs), long non-coding RNAs (lncRNAs), and many RNA-binding proteins (RBPs). In this scenario, a few studies focused their attention on an important translational regulatory role mediated by p53 (Marcel V *et al.*, 2015) (**Figure 1.7**).

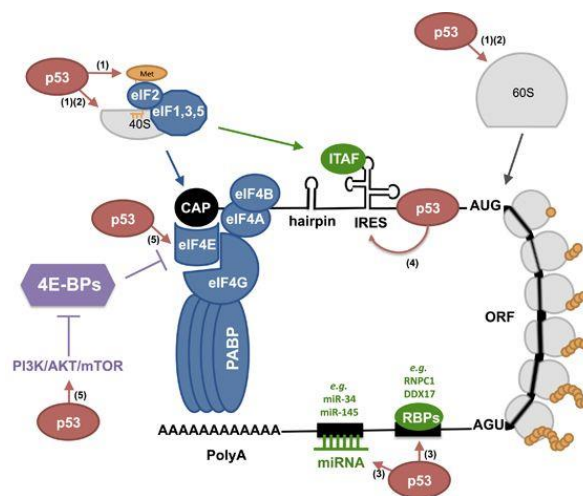


Figure 1.7: Role of p53 in translational control: Translation is regulated by several *cis*- and *trans*- acting elements and some of them, such as miRNA, lncRNA, ribosome biogenesis and others could be regulated by p53 (Marcel V *et al.*, 2015).

1.3.3.1 p53 in post-transcriptional control: miRNAs and lncRNAs

Several studies reported that p53 regulates miRNAs expression and processing. Those biological molecules are small non-coding RNAs of about 20 nucleotides that act as negative *trans*-regulators of mRNA metabolism and translation. miRNAs, binding through partial sequence complementarity, promotes both translation inhibition and the degradation of target mRNAs (Kong YW *et al.*, 2012). In humans, more than 1000 miRNAs are expected to be expressed and can impact on the regulation of more than 60% of all genes. There is a high potential for fine-tuning and coordinated regulation of groups of mRNAs given the ability of miRNAs to regulate more than one mRNA target and on the presence of many miRNA binding sites in a given UTR.

Indeed, a single miRNA can regulate an average of 400 mRNA targets (Hermeking H, 2012).

Initially, p53 entered in the miRNA world with the miR-34 family discovery and their identification as direct p53 targets in response to DNA damage or oncogenic-induced stress (Chang TC *et al.*, 2008; He L *et al.*, 2007). Since then, p53 has been involved in the transcriptional regulation of several miRNA families (Hermeking H, 2012). Their transcriptional regulation involves the direct binding of p53 to responsive elements present within their promoters, equivalent to the classical protein-coding p53-target genes. Moreover, p53 in response to DNA damage could promote miRNAs processing by enhancing the interaction between the RNA helicase p68 and the DROSHA complex, an essential step for the cleavage of primary miRNAs into the miRNA precursors (Suzuki HI *et al.*, 2009).

Several studies demonstrated that the regulation of miRNAs by p53 occurs in both basal and stress conditions, meaning that miRNAs could contribute to both physiological and stress-mediated functions of p53. Furthermore, there is complex crosstalk, given that a single miRNA can regulate several mRNAs involved in different p53-regulated cellular functions, such as: cell cycle arrest, cell viability, differentiation, epithelial to mesenchymal transition, and energetic metabolism (Raver-Shapira N *et al.*, 2007; Chang CJ *et al.*, 2011). In addition, miRNAs can contribute to robustness or attenuation in p53-induced transcriptional responses, by being part of feed-forward or negative feedback loops (Le MTN *et al.*, 2009; Sinha AU *et al.*, 2008).

In addition to the regulation of miRNAs, it has been found that p53 is involved also in the control of several lncRNAs transcription in response to DNA damage (Deng G *et al.*, 2013). LncRNAs are RNAs that are longer than 200 nucleotides and participate in many functions, including chromatin organization, transcriptional, and post-transcriptional regulation by directly interacting with DNA, RNA, or proteins. For example, among the different p53-induced lncRNAs, lincRNA-p21 associates with JUNB and CTNNB1 mRNAs, a proto-oncogene, and beta-catenin gene respectively, causing their silencing and decreasing their amount on polysomes, impacting their translation (Yoon JH *et al.*, 2012).

1.3.3.2 *p53 in post-transcriptional control: Ribosome biogenesis*

Translation is performed by a complex machinery composed of ribosomes, ribosomal proteins (RPs), and ribosomal RNA (rRNA). Several structural studies demonstrate that the core ribosome is sufficient to perform translation although additional RPs and rRNAs segments have been selected through evolution. These elements made the process more precise, increasing translation efficiency and specificity. Indeed, molecular analysis revealed that translation activity strongly depends on ribosome composition and its defect could result in distinct developmental disorders in human and animal models. In particular, rRNAs exhibit chemical modification such as pseudo-uridylation, base methylation, and 2'-O-ribose methylation, catalyzed respectively by dyskerin (DKC1), by specific rRNA methyl-transferase, and by fibrillarin (FBL) (Jenner L *et al.*, 2012; Xue S *et al.*, 2012).

Many studies demonstrated a p53 regulatory role in some of those rRNAs modifications, impairing the translation of a subset of IRES-containing mRNAs encoding for example p27, Bcl-XL, or XIAP (Simeonova I *et al.*, 2013; Yoon A *et al.*, 2006).

2'-O-ribose methylation is another rRNA modification that could be affected by p53 status, through the regulation of its indirect target gene FBL. It was demonstrated that mutant p53 or its knock-down, using a stable expression of a short hairpin RNA, increases FBL expression at both transcriptional and translational levels, while p53 activation in response to DNA damage reduces it. Indeed, p53 binds to the DNA response elements located in FBL first intron, repressing the promoter activity of this gene. Lower levels of FBL are associated with a modification of rRNA 2'-O-ribose methylation pattern involved in the intrinsic activity of ribosomes. This phenomenon increases the translation of a subset of IRES-containing mRNAs (i.e. c-Myc and VEGF-A) with defects in translation fidelity (Marcel V *et al.*, 2015).

1.3.3.3 *p53 in post-transcriptional control: Ribosome assembly*

Global protein synthesis is mainly regulated by translation initiation through the presence of chemical modifications at the 5'-end of all mRNA called the CAP. Initially, the ribosome assembly starts when two eukaryotic initiation factors (eIFs) called eIF4E and eIF4G bind the mRNA CAP, forming a protein:RNA complex that is critical to recruiting the mRNA to the small ribosome subunit. Then, eIF4E:eIF4G interaction is abolished through the sequestration of eIF4E by the unphosphorylated

forms of 4E-BP1 and its phosphorylation by mammalian target of rapamycin (mTOR) pathway releases eIF4E and promotes translational initiation (Sonenberg N *et al.*, 2009).

Several studies demonstrate that p53 plays a translational control role in this process through the inhibition of eIF4E by different mechanisms. It has been reported that the transcription of this initiation factor could be repressed when c-myc, a positive regulator of eIF4E expression, is sequestered by p53 (Zhu N *et al.*, 2005). Moreover, the p53-target gene TRIM22 has been shown to interact with eIF4E and its overexpression inhibits the formation of eIF4E:eIF4G complex, reducing the global protein synthesis (Pettersson J *et al.*, 2012). Further, p53 promotes eIF4E sequestration by enhancing the dephosphorylation of 4E-BP1, even if the exact molecular mechanism remains unknown (Horton LE *et al.*, 2002). Finally, it has been shown that p53 controls the rate of protein synthesis through mTOR pathway modulation (Budanov AV *et al.*, 2008). p53 activation by nutlin-3a treatment inhibits the translation of mRNAs encoding several translational factors, including eIF4E. It has been demonstrated that the inhibition of selective translation is abolished by the silencing of both Sestrin-1 and Sestrin-2, two p53-target genes that inhibit mTOR signaling (Budanov AV *et al.*, 2008).

1.3.3.4 p53 in post-transcriptional control: RNA-binding proteins

RNA-binding proteins (RBPs) are defined as proteins that have an RNA-binding domain which allows the direct binding to RNA on specific sequences. Their main role is to control different aspects of RNA processing, including degradation, splicing, transport, and translation (Wurth L, 2012).

Several studies revealed that p53 regulates the expression of a large number of RBPs, at transcriptional and translational levels, both in untreated and p53-activating treatment conditions. For example, DDX17 (p72) is an RBP that participates in miRNAs processing, whose translation is inhibited by p53 activation (Zaccara S. *et al.*, 2014). Even if many p53-regulated RBPs were identified (Marcel V. *et al.*, 2015; Scoumanne A. *et al.*, 2011), the identity and the number are dependent upon the nature of the stress, meaning that they may participate in defining the different p53-induced gene networks necessary to trigger the multiple p53 cellular functions (Zaccara S. *et al.*, 2014). It has been even proposed that p53 could act as an RBP itself, directly binding RNA (Riley KJL *et al.*, 2007). Moreover, part of the

cytoplasmic p53 protein could be associated with the polysomal fraction, maybe linked to the 5' end of 5.8S rRNA (Fontoura BM *et al.*, 1992). Furthermore, p53 can also be regulated by RBPs. For example, the p53-target gene RNPC1 is an RBP that binds the p53 mRNA UTRs repressing its translation (Zhang J *et al.*, 2011).

Another important role of RBPs is the regulation of mRNA half-life. This process is finely controlled together with non-coding RNAs (miRNAs and lncRNAs) that regulate the balance between mRNAs polyadenylation/deadenylation or exosome-induced mRNA degradation. Thus, by regulating RBPs and non-coding RNAs, p53 can control mRNAs metabolism in addition to their translation efficiency (Muller-McNicoll M *et al.*, 2013).

1.4 DExH-Box Helicase (DHX) proteins

RNA-binding proteins (RBPs) are able to bind to single or double-stranded RNA molecules through various types of structural domains, forming ribonucleoprotein complexes (Lunde BM *et al.*, 2007). DExH-Box ATP-dependent RNA helicases are an important group of RBPs that regulate many aspects of RNA processing and, in particular, translation. Their structure is composed of nine conserved motifs: Q-motif, motif-I, motif-Ia, motif-Ib, motif II, motif III, motif IV, motif V and motif VI (Linder P *et al.*, 1989). Motif II is also known as the Walker B motif and, together with motif-I, Q-motif, and motif VI, is able to bind and hydrolyze ATP while motif Ia, Ib, III, IV, and V are involved in intramolecular rearrangement and RNA interaction (Tanner NK *et al.*, 2003).

DHX9 is one well-studied member of this family, also known as Nuclear DNA Helicase II and RNA Helicase A, capable of unwinding both RNA and DNA. It has a predominantly nuclear localization and it has been seen to play an important regulatory role in gene expression, interacting with many proteins and nucleic acids partners (Lee T *et al.*, 2016). Its loss in primary human fibroblast results in premature p53-dependent senescence (Lee T *et al.*, 2014). It has been seen that DHX9 can interact with proteins binding 5'UTR structural elements of many mRNAs, including IRES as well as inverted-repeat ALU elements. In this context, DHX9 can facilitate mRNA association with polysomes and stimulate their translation (Cai L *et al.*, 2010; Jin J *et al.*, 2011; Grover R *et al.*, 2009; Aktas T *et al.*, 2017).

Another DHX family protein that plays an important role in mRNA translation is DHX36. Indeed, the first 105 amino acid of this RBP have been shown to be critical for RNA binding and re-localization to specific cytoplasmic foci called Stress

Granules (SGs), composed by a dense aggregation of proteins and RNAs, that appear under cell stress condition (Chalupniková K *et al.*, 2008). They play important functions storing or degrading untranslated mRNAs (Mollet S *et al.*, 2008). Moreover, it was established that DHX36 is able to bind DNA and RNA G-quadruplex, important structures that have a role in replication, transcription, and translation. It was demonstrated that DHX36 had an ATP-independent unfolding property on G-quadruplex, followed by an ATP-dependent refolding, regulating DNA replication, transcription, and RNA translation (Chen MC *et al.*, 2018; Tippana R *et al.*, 2019).

1.4.1 DHX30: The protagonist of our story

DExH-Box Helicase 30 (DHX30) is a poorly studied ATP-dependent RNA helicase. It is strongly expressed in neural cells and somites during embryogenesis in mice. It plays an important role in the development and its homozygous mutation is lethal for embryos (Zheng HJ *et al.*, 2014). It has been shown that human DHX30 is involved in the antiviral function of the zinc-finger ZAP protein. Indeed, it was demonstrated that these two proteins directly interact each other via the N-terminal domain and that DHX30 is necessary for the optimal antiviral activity of ZAP (Ye P *et al.*, 2010). Moreover, it has been shown that the N-terminal 152 amino-acids residue segment of DHX30, containing the dsRNA-binding domain, possesses all the antiviral activity of this RBP. A work by Chen and collaborators showed that this portion of DHX30 binds NS1, an Influenza A virus non-structural protein that inhibits host antiviral response. The DHX30:NS1 complex inactivates the function of viral protein NS1, allowing cellular antiviral response upon Influenza A virus infection (Chen G *et al.*, 2020).

Recently, six de novo missense mutations were identified in DHX30 in twelve unrelated patients affected by global developmental delay (GDD), intellectual disability (ID), severe speech impairment, and gait abnormalities. All mutations caused amino acid changes in the highly conserved helicase motif, impairing protein's ATPase activity, or RNA recognition. Moreover, cells that carry these mutations in DHX30 exhibit an increased propensity to trigger stress granules (SG) formation decreasing global translation (Lessel D *et al.*, 2017). Furthermore, it has been shown that DHX30 could play an important role also in the mitochondrial inner membrane based on studies with human fibroblasts and osteosarcoma cells. Indeed, in that compartment it interacts with a Fas-activated serine-threonine kinase

(FASTKD2), modulating mitochondrial ribosome maturation and assembly, regulating in this way mitochondrial translation and cell energy outcome (Antonicka H *et al.*, 2015; Wang Y and Bogenhagen D, 2006).

1.5 Aim of the thesis

Starting from an observation by Tovar and collaborators (Tovar C *et al.*, 2006), in a recent work from our laboratory, the p53-mediated response to Nutlin treatment was examined in two different cancer cell lines: HCT116 and SJSA1. It was observed that p53 activation caused cell cycle arrest in HCT116, but massive apoptosis in SJSA1. An intermediate phenotype had been observed in MCF7. Then, analyzing the translomes of HCT116 and SJSA1 cells, *i.e.* the ensemble of transcripts loaded on polysomes and in active translation, only 0.2% of the differentially expressed genes (DEGs) were in common. Many genes were translationally upregulated by Nutlin exclusively in SJSA1 cells, with enrichment for pro-apoptotic transcripts, which shared instance of a CG-rich motif in 3'UTR (dubbed CGPD-motif). The motif was shown to be sufficient for conferring mRNA translation upregulation when placed inside a 3'UTR of a reporter transcript in SJSA1 cells treated with nutlin. Investigating on RBPs that could bind this motif, the DExH box RNA helicase DHX30 was found. In detail, DHX30 was more abundant in HCT116 than SJSA1 and was shown to play a negative role in translation control of transcripts containing the CGPD-motif. Indeed, its depletion in HCT116 increased the translation efficiency of CGPD-mRNAs and also the apoptosis proneness after p53 activation, mimicking in part the apoptotic phenotype of SJSA1 cells after Nutlin treatment (Rizzotto D *et al.*, 2020).

Based on these evidence, the first aim of my thesis work consists of exploring the role of DHX30 in cytoplasmic translation control. Specifically, I studied how DHX30 impacts ribosomes biogenesis and what are the consequences on both global and mRNA specific translation.

Furthermore, since it has been shown that DHX30 plays an important role also in mitochondrial translation (Antonicka H *et al.*, 2015), a second aim is to explore in our cell models the role of this RBP in mitochondria. In particular, I explored if the silencing of DHX30 can impact mitochondrial gene expression at the level of transcription and/or translation and what are the consequences for mitochondrial function.

Then, exploiting isoform-selective transient silencing, I also explored which are the specific contributions of cytoplasmic and mitochondrial DHX30 to cell translation, energy balance, and cell fitness in culture, and also considered the p53 status.

Finally, after the observations made by Rizzotto *et al* in which Nutlin increases cell apoptosis when DHX30 is silenced, the final aim consists in exploring if the DHX30 silencing reduces cancer cells' survival upon others treatments able to activate p53 or damaging the mitochondria, moving the first step towards a possible cancer treatment that considers or perturbs DHX30 expression. I have also explored whether DHX30 expression and a signature of its regulated transcripts can have prognostic value in human cancers.

Chapter 2: Materials and Methods

2.1 Human cell lines and growth conditions

HCT116 and MCF-7 shNT and DHX30 silenced clones were obtained as described by Rizzotto D *et al*, 2020. In detail, HCT116 cells were transduced with lentiviral vectors containing a pLK0.1 plasmid expressing a shRNA sequence against DHX30 (GCACACAAATGGACCGAAGAA, targeting exon 5) or scramble sequence SHC206, under the constitutive promoter hU6. Puromycin (Sigma Aldrich, St. Louis, MO, USA) was used to maintain the selection, at 0.1 mg/mL as final concentration and single clone isolates were then obtained by limiting dilution.

HCT116 p53^{-/-} was obtained from Sur S. *et al*, 2009. All cell lines were cultured in RPMI pH 7.4 (Thermo Fisher Scientific, Waltham, MA, USA) supplemented with 10% Fetal Bovine Serum (Thermo Fisher Scientific, Waltham, MA, USA), 1X L-Glutamine, and Pen/Strep (Thermo Fisher Scientific, Waltham, MA, USA) at 37 °C with 5% CO₂ in a humidified atmosphere. For HCT116 shNT and shDHX30, 0.2 µg/mL Puromycin (Sigma Aldrich, St. Louis, MO, USA) was added to the culture medium to maintain the selection of the vectors. Puromycin was removed 24 hours before starting a specific experiment to avoid confounding effects.

U2OS cells were cultured in DMEM pH 7.4 (Thermo Fisher Scientific, Waltham, MA, USA) supplemented with 10% Fetal Bovine Serum, 1X L-Glutamine and Pen/Strep at 37 °C with 5% CO₂ in a humidified atmosphere.

MCF-7, U2OS, and HCT116 parental and p53^{-/-} cells were silenced for cytoplasmic and mitochondrial DHX30 variants using 25nM siRNAs (Trifecta, IDT, Coralville, IA, USA) (Table 2.1) transfected with Interferin (Polyplus-transfection, Illkirch, France). All experiments were performed at least 24 hours post-silencing.

SiRNA	Silenced variant	Sequence
siRNA NC	Negative Control	Does not recognize any sequences in the human transcriptome.
siRNA 13.1	DHX30-C	3'-AGU AACG AAAAAUAUCCUAAGGUCGAA-5'
siRNA 13.3	DHX30-C+M	3'-UGUCCUUCUUGCGAUACUGGACUUCU-5'

Table 2.1: siRNAs used to silence DHX30 variants in HCT116 cells and their sequences

2.2 RNA-seq data analyses

[Performed by Erik Dassi]

Reads were first quality filtered and trimmed with trimmomatic (minimum quality 30, minimum length 36nt) (Bolger AM. *et al.*, 2014). Then, each Gencode v27 (<http://www.gencodegenes.org/releases/>) transcript was quantified with Salmon (Srivastava A. *et al.*, 2016). Eventually, edgeR (Robinson MD. *et al.*, 2010) was used to call Differentially Expressed Genes (DEGs) between conditions at the polysomal and total levels (shDHX30 DMSO vs shNT DMSO), using a 0.05 threshold on the adjusted p-value. GSEA was performed with the fgsea R package (Sergushichev AA. *et al.*, 2016), including the Hallmark, Canonical Pathways, and GO gene sets. We used 1000 permutations to compute the significance p-value and used a BH adjusted p-value threshold of 0.05. Translational efficiency (TE) was computed on normalized expression data (counts per million reads, CPM) as the ratio of polysomal CPMs over total CPMs for each replicate and transcript in the annotation. Differences in TE (between conditions and groups of genes) and between polysomal and total samples were assessed by the Wilcoxon test.

2.3 Western Blot

Cells were cultured in 6-well tissue culture plates. Cells were treated as required for a specific endpoint, collected detaching them by trypsin-EDTA followed by centrifugation and one washed in PBS 1X. Samples were then lysed by RIPA buffer and proteins were quantified by BCA assay (Thermo Fisher Scientific). Usually, 30 µg of extracted proteins were loaded on 12% or 15% Bis-Tris acrylamide Gels and transferred after an electrophoretic run onto nitrocellulose membranes using a Tris-Glycine buffer. Transfer was checked used the Ponceau S solution (Sigma Aldrich). Blocking was performed with 5% non-fat dry milk, 0.1% TWEEN in PBS 1X (PBS-T) for at least 1 hour at room temperature (RT). Immunodetection was obtained incubating a primary antibody (**Table 2.2**) diluted in PBS-T 1% milk overnight at 4°C under mild orbital shaking. The day after, membranes were washed three times with PBS-T and then incubated with secondary antibodies (Table 2.2), also diluted in PBS-T milk 1%, for 1 hour at RT. Finally, membranes were washed three times with PBS-T and analyzed by ECL (GE Healthcare, Chicago, IL, USA) using a

ChemiDoc™ XRS+ (Bio-Rad, Hercules, CA, USA) and the ImageLab software ver. 3.0 (Bio-Rad).

Primary Antibody	Host	Dilution	Brand
DHX30	Rabbit	1:5000	Abcam
MT-ATP6	Goat	1:2000	Invitrogen
MT-ATP8	Rabbit	1:2000	Invitrogen
MRPL11	Rabbit	1:2000	Invitrogen
MRPS22	Rabbit	1:2000	Invitrogen
Alfa-actinin	Mouse	1:10000	Santa Cruz
Tubulin	Mouse	1:10000	Santa Cruz

Secondary Antibody	Host	Dilution	Brand
Anti-rabbit	Mouse	1:10000	Santa Cruz
Anti-mouse	Rabbit	1:10000	Santa Cruz
Anti-goat	Donkey	1:7000	Santa Cruz

Table 2.2: Primary and secondary antibodies used in immunoblots performed.

2.4 Translation assays

2.4.1 Polysome profiling

Polyribosome analysis was performed as described in Provenzani A. *et al*, 2006. Briefly, HCT116 cells were grown on 15 cm Petri dishes with standard DMEM and serum. When the cells reached 80% of confluence, cycloheximide (0.01 mg/ml) was added and kept in incubation for 10 min. Then cells were washed three times with cold PBS containing cycloheximide (0.01 mg/ml) and lysed with the following lysis buffer: 20 mM Tris-HCl (pH 7.5), 100 mM KCl, 5 mM MgCl₂, 0.5% Nonidet P-40, 100 U/ml RNase inhibitors. Mitochondria and nuclei-free lysates were loaded onto 15–50% (w/v) density sucrose gradients in a salt solution (100 mM NaCl, 5 mM MgCl₂, 20 mM Tris-HCl pH 7.5), and ultracentrifuged at 180 000 × g for 100 min at 4°C. The sedimentation profiles were monitored by absorbance at 254 nm using a Teledyne ISCO UA-6 fractionator coupled to an UV detector, collecting thirteen 1 ml fractions. RNA from pooled polysomal fraction was extracted and processed as described in (Rizzotto D *et al.*, 2020). For Western blot analysis, proteins were precipitated with TCA plus acetone and the pellets were solubilized directly in Laemmli buffer pH 8.

2.4.2 Ribosome isolation

Cell fractionation to isolate ribosomes was performed following the protocol described by Belin S *et al*, 2010. Briefly, 8×10^6 cells were seeded in a T150 flask, 48 hours before the procedure. At 80% of confluence, cells were detached and counted. 1×10^7 cells were then pelleted by $500 \times g$ centrifugation for 5 minutes at 4°C and washed once with cold PBS. The supernatant was discarded and the pellet was re-suspended gently with $300\mu\text{L}$ of cold buffer A (sucrose 250mM, KCl 250mM, MgCl_2 5mM, and Tris-Cl 50mM pH 7.4), added in three sequential steps, pipetting after every adding. To perform cell lysis, an appropriate volume of NP-40 was added to the homogenized cellular solution, to obtain a 0.7% (v/v) final concentration of the detergent, and cells were incubated on ice for 15 minutes, homogenizing the suspension by gentle pipetting every 5 minutes. Then the cell lysate was centrifuged at $750 \times g$ for 10 minutes at 4°C to pellet nuclei; the recovered cytoplasmatic fraction (supernatant) was centrifuged again at $12.500 \times g$ for 10 minutes at 4°C to obtain a mitochondria pellet. The supernatant containing ribosomes was collected and its volume was accurately measured using a graduated pipet. KCl 4M solution was then slowly added to reach a final concentration of 0.5M. Meanwhile, 1mL of the sucrose cushion solution (sucrose 1M, KCl 0.5M, MgCl_2 5mM, and Tris-Cl 50mM pH 7.4) was added into a 3-mL polycarbonate tube for an ultracentrifuge TL100.3 rotor (Beckman Coulter, Brea, CA, USA). The KCl-adjusted ribosome-containing solution was carefully added above the sucrose cushion and tubes were balanced by weight using buffer B (sucrose 250mM, KCl 0.5M, MgCl_2 5mM, and Tris-Cl 50mM pH 7.4). Then, they were ultracentrifuged at $250.000 \times g$ for 2 hours at 4°C . At the end of centrifugation, the supernatant was discarded and a very compact and dense translucent pellet containing ribosomes was quickly rinsed twice by carefully adding $200\mu\text{L}$ of cold water. Then, the pellet was re-suspended in $300\mu\text{L}$ of buffer C (KCl 25mM, MgCl_2 5mM, and Tris-Cl 50mM pH 7.4), adding the solution in three sequential steps and gently homogenized by pipetting after every $100\mu\text{L}$ addition. Finally, to estimate the amount of ribosomes, the optical density of the suspension was measured with the spectrophotometer nanodrop at 260nm.

2.4.3 Global translation

Global translation assay was performed using Click-iT[®] AHA Alexa Fluor[®] 488 Protein Synthesis HCS Assay (Thermo Fisher Scientific) (**Figure 2.1**). Briefly, cells were cultured in 96-well plates and were treated with 100mM 5-Fluorouracil (Sigma

Aldrich) as the positive control. After 24 hours of treatment, the culture medium was removed and 50 μ M L-azidohomoalanine prepared in pre-warmed L-methionine-free medium (Lonza) was added and cells were incubated for 1 hour. Cell fixation was performed using 3.7% formaldehyde (Sigma Aldrich) incubating the plate at RT for 15 minutes. After two washes with 3% BSA in PBS 1X cells were permeabilized with 0.5% Triton[®] X-100 (Sigma Aldrich) and incubated for 15 minutes at room temperature. Cells were then washed twice with 3% BSA in PBS 1X and Click-iT[®] reaction cocktail was added incubating for 30 minutes at room temperature, protected from light. After this incubation the reaction cocktail was removed, cells were washed twice with 3% BSA in PBS 1X and stained with 5 μ g/mL Hoechst (Sigma Aldrich). Samples' images were acquired and analyzed by high content fluorescence microscope Operetta[®] (PerkinElmer, Waltham, MA, USA) using the following filter set: Alexa Fluor[®] 488: Ex495/Em519 nm; Hoechst: Ex350/Em461 nm.

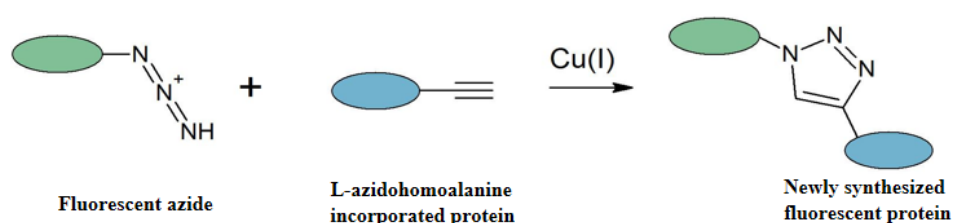


Figure 4.1: Example of AHA click-it chemistry reaction to analyse cellular global translation.

2.4.4 Fluorescent In Situ Hybridization on rRNA

For Fluorescent In Situ Hybridization (FISH) assay, cells were cultured on a coverslip place onto a 48-well plate and after 48 hours they were washed with PBS and fixed with 4% Paraformaldehyde (PFA) (Sigma Aldrich) for 30 minutes at RT. Then, cells were washed twice with PBS 1X and incubated in 70% ethanol overnight at 4°C. The day after, cells were rehydrated with 10% formamide in 2X SSC (Sigma Aldrich), twice for 5 minutes at RT. Meanwhile, buffer A [5 μ L formamide, 2.5 μ L SSC 2X, 2.5 μ L tRNA (10ng/ μ L), water up to 20.25 μ L and then 2.5 μ L of each probe (10ng/ μ L) (**Table 2.3**)] was incubated for 5 minutes at 90°C and then mixed quickly together with buffer B [25 μ L Dextran sulfate 20% in SSC 4X, 1.25 μ L Bovine Serum Albumin (BSA) (10ng/ μ L) and 2.5 μ L ribonucleoside vanadyl complex (RVC) (200mM)]. Then, 50 μ L A+B probe solution was dropped onto the coverslip and it

was incubated in a humidified chamber for 3 hours at 37°C. When the incubation was finished, the coverslip was washed twice with 10% formamide in SSC 2X for 30 minutes at RT and once with PBS 1X for 5 minutes. Cells were stained with a solution of 0.5µg/mL DAPI (Sigma Aldrich) in PBS 1X for 5 minutes, washed three times with PBS 1X and the coverslip was finally placed with mounting medium on a glass slide. Finally, images were acquired using Zeiss Observer z1 fluorescent microscope (Carl Zeiss, Oberkochen, Germany) with ZEN 2 blue edition software ver. 2.3 (Carl Zeiss). Images' fluorescence intensity was measured using Cell Profiler software ver. 3.1.9 (Broad Institute, Cambridge, MA, USA).

Probe	Fluorophore	Sequence
18S	Alexa-Fluor 555	5'-ATCGGCCCGAGGTTATCTAGAGTCACCAA-3'

Table 2.3: Probe used to hybridize and visualize 18S rRNA. Probe sequences and conjugated fluorophores are reported in table.

2.4.5 rRNA biogenesis

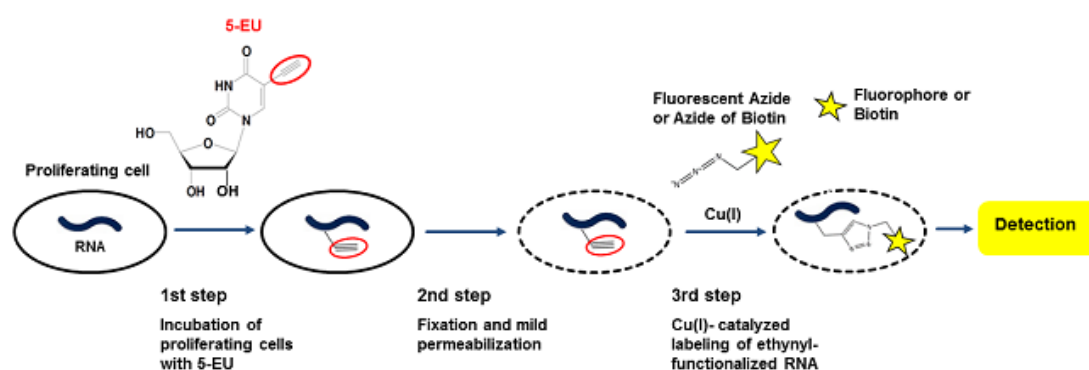


Figure 2.2: Example of 5-EU assay procedure to analyse cellular rRNA biogenesis.

rRNA biogenesis was performed following the protocol described by Cornella N *et al*, 2017. Briefly, cells were cultured in 96-well tissue culture plates and after 24 hours were treated with Actinomycin D 100nM (Sigma Aldrich) as positive control. After 24 hours of treatment, 1mM 5-Ethyluridine (Sigma Aldrich) was added to the culture medium and the plate was incubated for 2 hours. This short incubation with 5-EU allows a higher rate of incorporation in rRNAs than mRNAs, reducing the background signal. Then, cells were fixed using a working solution 1 (WR1) composed by 125mM Pipes pH 6.8 (Sigma Aldrich), 10mM EGTA (Sigma Aldrich), 1mM MgCl₂ (Merck Millipore, Burlington, MA, USA), 0.2% Triton[®] X-100 (Sigma Aldrich), and 3.7% formaldehyde (Sigma Aldrich). Cells were washed twice with

TBS 1X and stained for 30 minutes at room temperature using a working solution 2 (WR2) composed by 100mM Tris-HCl pH 8.5 (Sigma Aldrich), 1mM CuSO₄ (Merck Millipore), 10µM fluorescent azide (Sigma Aldrich), and 100mM ascorbic acid (Merck Millipore). After four washes with TBS containing 0.5% Triton X-100, cells were stained with 0.5µg/mL Hoechst (Sigma Aldrich), and samples' images were acquired and analyzed by high content fluorescent microscope Operetta® (PerkinElmer) using the following filter set: Alexa Fluor® 488: Ex495/Em519 nm; Hoechst: Ex350/Em461 nm.

2.5 Cell proliferation analysis

2.5.1 Colony formation

1.0x10³ cells/well were seeded in 6-well plates and incubated. Culture medium was changed every three days. Colonies were fixed after 14 days with 3.7% formaldehyde and stained with a solution containing 30% Methylene blue (Sigma Aldrich) in water, then washed five times for 5 minutes under agitation. Finally, images were acquired and analyzed using ImageJ software 1.8.0.

2.5.2 Cell count

To analyze cell proliferation by cell count, 1.0x10³ cells/well were seeded in 96-well plates and incubated. Images were acquired by high content fluorescent microscope Operetta® in digital phase-contrast every 24 hours for a total of three days.

2.5.3 Real-Time Cell Analysis (RTCA)

To analyze cell proliferation by Real-Time Cell Analyser Xcelligence® (RTCA) (Roche, Basel, Switzerland) the background was set adding only the cell culture medium in each well of an E-plate and incubating it 30 minutes. After the incubation, the background was read. Then, 1.0x10³ cells/well were seeded and incubated for 30 minutes, and then the E-plate was inserted in the RTCA and impedance-based cell proliferation was estimated by RTCA readings every 15 minutes in the course of three days.

2.5.4 Spheroid assay formation

To measure spheroid formation and 3D cell proliferation, 3.0x10³ cells/well were seeded in U-bottom ultra-low attachment 96-well plates (Corning Incorporated, Corning, NY, USA), centrifuged at 3000 rpm for 5 minutes and incubated. For MCF-

7, 100 μ L of cold medium containing 3.0x10³ cells/well were mixed with 2.5% of Cultrex® BME (Trevigen, Gaithersburg, MD, USA), centrifuged at 5000 rpm for 10 minutes at 4°C and incubated. Starting after three days of incubation, images were acquired every 24 hours for eight additional days by microscope (Leica, Wetzlar, Germany). The spheroids' area was measured by ImageJ software.

2.6 Immunofluorescence

3.0x10⁵ cells/well were seeded on glass coverslip inserted in 6-well plates and incubated overnight. The days after, cells were fixed in 4% Paraformaldehyde (PFA) for 15 min. Then the PFA solution was removed and cells were rinsed twice with PBS 1X. After washing, cells were incubated for 1 hour with a blocking solution (PBS 1X, 5% BSA, and 0.5% Triton X-100). Next, cells were incubated overnight at 4°C with primary antibodies (**Table 2.4**) diluted in blocking solution. The following day, after three washes with PBS 1X, the anti-mouse and anti-rabbit secondary antibodies conjugated with AlexaFluor 488 or AlexaFluor 594 (Invitrogen, Carlsbad, CA, USA) (**Table 2.4**) were added to the samples and incubated for 1 hour at RT under agitation. Cells were washed with PBS 1X three times and cell nuclei were stained with 0.5 μ g/mL Hoechst (Sigma Aldrich). Finally, coverslips were mounted on glass slides and images were acquired using Zeiss Observer Z1 fluorescent microscope and Zen software.

Primary Antibody	Host	Dilution	Brand
DHX30	Rabbit	1:500	Abcam
MT-ATP6	Goat	1:200	Invitrogen
MT-ATP8	Rabbit	1:200	Invitrogen

Secondary Antibody	Host	Dilution	Brand
Anti-rabbit	Mouse	1:1000	Santa Cruz
Anti-mouse	Rabbit	1:1000	Santa Cruz
Anti-goat	Donkey	1:1000	Santa Cruz

Table 2.4: List of primary and secondary antibodies with the dilutions used in immunofluorescence experiments performed.

2.7 Cell metabolism assays

2.7.1 XFp Seahorse analyzer: Compensatory glycolysis test

Compensatory glycolysis analysis was based on Seahorse XFp glycolytic rate assay protocol. Briefly, 3.0×10^3 cells/well were seeded in XFp cell culture microplate (Agilent Technologies, Santa Clara, CA, USA) in cell culture medium and incubated overnight. Meanwhile, XF calibrant solution was added in each well of an extracellular flux cartridge (Agilent Technologies) incubated overnight without CO₂. The day after, cells were washed twice with XF assay medium. Then, 200 μ L of assay medium was added to each well and the cartridge was incubated 45 minutes at 37°C without CO₂. In the meantime, an XFp sensor cartridge was prepared adding drugs, diluted in XF assay medium, in respective ports (**Table 2.5**), and the cartridge was calibrated by Seahorse XFp analyzer (Agilent Technologies) setting the Seahorse glycolytic rate assay program. When the calibration was finished, the cell microplate was inserted in Seahorse XFp analyzer and the analysis was started. To normalize data obtained by Seahorse, at the end of the analysis cells were stained with 2.5 μ g/mL Hoechst, added directly into the medium, and cell number was calculated by Operetta[®] (PerkinElmer).

Port	Drug	Stock concentration	Volume added to port	Final concentration
A	Rotenone/Antimycin a	5 μ M	20 μ L	0.5 μ M
B	2-Deoxyglucose	500mM	22 μ L	50mM
C	-	-	-	-
D	-	-	-	-

Table 2.5: Compounds preparation for loading into the ports of sensor cartridge. In the table are reported the stock concentrations and volumes of drugs used to perform the Seahorse glycolytic rate assay program

2.8 RNA extraction and RT-qPCR

To extract RNA, 3.0×10^5 cells/well were seeded in 6-well plates and incubated overnight. After a specific treatment or timepoint, cells were detached by trypsin and the pellet was lysed by β -mercaptoethanol containing lysis buffer. RNA was extracted using the Illustra RNAspin Mini RNA Isolation kit (GE-Healthcare, Chicago, IL, USA) following the kit protocol. Then, RNA was retro-transcribed using RevertAid RT Kit (Thermo Fisher Scientific), random hexamers, and the retrotranscription

program conditions described in the kit protocol. Finally, RT-qPCR was performed using 25ng of cDNA and 2X qPCR SyGreen master mix (PCR Biosystems, London, England) in Cfx96™ Real-Time System or Cfx384™ Real-Time System Thermocyclers (Bio-Rad). RT-qPCR program conditions were: (i) 95°C, 180 sec; (ii) 95°C, 10 sec; (iii) 60°C, 20 sec; (iv) 72°C, 5 sec with plate reading; (v) go to (ii) for 39 cycles; (vi) melt curve from 72°C to 95°C with an increment of 0.5°C for 5 sec and plate reading. The list of all primers used is reported in **Table 2.6**. All RT-qPCR experiments are normalized using both B2M and YWHAZ housekeeping genes because they are not modulated by different expression of DHX30.

Primer	Sequence
DHX30_Fw	5'-AGCGTGGAGGTAGAAGGCTA-3'
DHX30_Rv	5'-CGGCCTAAAGAGCGGGATAG-3'
CytoDHX30_Fw	5'-GACGGAAGCTTGGTGAACG-3'
MitoDHX30_Fw	5'-TTCCACCCATGTGTGTCAAC-3'
C&MDHX30_Rv	5'-TTCGGTCCATTTGTGTGCAC-3'
MRPL11_Fw	5'-TGAGATTGCCCGCATCAAAG-3'
MRPL11_Rv	5'-TTCTTGGGCAGCCAAATCTG-3'
MRPS22_Fw	5'-TGACAGGCTTGAACCTGCAG-3'
MRPS22_Rv	5'-AATAAAACGCTCCCGGTGTG-3'
MT-RNR1_Fw	5'-CCAGAACACTACGAGCCACA-3'
MT-RNR1_Rv	5'-CATGGGCTACACCTTGACCT-3'
MT-RNR2_Fw	5'-ACTTTGCAAGGAGAGCCAAA-3'
MT-RNR2_Rv	5'-TGGACAACCAGCTATCACCA-3'
MT-CYB_Fw	5'-GCCCTCGGCTTACTTCTCTT-3'
MT-CYB_Rv	5'-GACGGATCGGAGAATTGTGT-3'
MT-ND1_Fw	5'-ATGGCCAACCTCCTACTCCT-3'
MT-ND1_Rv	5'-GGTAGATGTGGCGGGTTTTA-3'
MT-ND2_Fw	5'-AAGCAACCGCATCCATAATC-3'
MT-ND2_Rv	5'-TCAGAAGTGAAAGGGGGCTA-3'
MT-ND3_Fw	5'-ACCACAACCTCAACGGCTACA-3'
MT-ND3_Rv	5'-TAGGGCTCATGGTAGGGGTA-3'
MT-ND4_Fw	5'-GCTCCCTCCCCTACTCATC-3'
MT-ND4_Rv	5'-GTTTTGTCAGGGGGTTGAGA-3'
MT-ND4L_Fw	5'-TCGCTCACACCTCATATCCTC-3'
MT-ND4L_Rv	5'-GGCCATATGTGTTGGAGATTG-3'
MT-ND5_Fw	5'-ACATCTGTACCCACGCCTTC-3'
MT-ND5_Rv	5'-TCGATGATGTGGTCTTTGGA-3'
MT-ND6_Fw	5'-CCACAGCACCAATCCTACCT-3'
MT-ND6_Rv	5'-TGATTGTTAGCGGTGTGGTC-3'
MT-ATP6_Fw	5'-AATGCCCTAGCCCCTTCTT-3'
MT-ATP6_Rv	5'-TTAAGGCGACAGCGATTCT-3'
MT-ATP8_Fw	5'-ATGGCCCACCATAATTACCC-3'
MT-ATP8_Rv	5'-GCAATGAATGAAGCGAACAG-3'
MT-COX2_Fw	5'-CCATCCCTACGCATCCTTTA-3'
MT-COX2_Rv	5'-CGGGAATTGCCTTGTTTT-3'
MT-COX3_Fw	5'-CCCGCTAAATCCCCTAGAAG-3'

MT-COX3_Rv	5'-GGAAGCCTGTGGCTACAAAA-3'
B2M_Fw	5'-AGGCTATCCAGCGTACTCCA-3'
B2M_Rv	5'-ATGGATGAAACCCAGACACA-3'
YWHAZ_Fw	5'-CAACACATCCTATCAGACTGGG-3'
YWHAZ_Rv	5'-AATGTATCAAGTTCAGCAATGGC-3'

Table 2.6: List of primers and their sequence used in RT-qPCR experiments performed.

2.9 Droplet digital PCR

The Droplet PCR protocol used was based on that developed by Bio-Rad. Briefly, 1×10^5 cells were seeded in 6-well plates and grown for 1 day. Next cells were detached, counted, and solubilized in DireCtQuant 100ST solubilization reagent (DireCtQuant, Lleida, Spain) at the concentration of 1000 cells/ μ L. Lysates were obtained by incubation for 3 minutes at 90°C under shaking at 750 rpm and then centrifuged for 1 minute at 10000 g. The lysate was diluted 1:4 in solubilization reagent and for every target to analyze, a PCR mix was prepared comprising 2 μ L of the diluted sample, forward and reverse primers at 10 μ M final concentration in a final volume of 95 μ L. PCR mix without lysate was used as the negative control. Then, 10.5 μ L of each PCR reaction was mixed with 11 μ L of 2xQX200 ddPCR EvaGreen SuperMix (Bio-Rad) and 0.5 μ L of HindIII restriction enzyme (NEB, Ipswich, MA, USA). Sample DNA was digested at 37°C for 15 minutes and loaded in ddPCR DG8™ Cartridge with QX200™ droplet generation oil (Bio-Rad). Droplets were made using the QX200™ droplet generator (Bio-Rad) and then loaded in a 96-well PCR plate. Sample DNA was amplified and finally, droplets with amplified DNA were analyzed using the QX200™ droplet reader and QuantaSoft 1.7.4 (Bio-Rad).

2.10 RNA immunoprecipitation

HCT116 cells were cultured in standard medium in P150 plates till they reached ~80% confluence. $\sim 10^7$ cells were lysed in 1mL of Lysis buffer (100mM KCl, 5mM MgCl₂, 10mM HEPES pH 7, 0.5% NP-40, 1mM DTT, 1U/ μ l RNase Inhibitors, 1X Protease Inhibitor Cocktail) using a scraper. Lysates were transferred in a falcon tube, placed for at least two hours at -80°C, and centrifuged at 10000 rpm for 30 minutes. Supernatants were collected in a new tube. Dynabeads ProteinA or ProteinG (depending on the antibody species, Thermo Fisher Scientific) were prepared by washing them twice with NT2 Buffer (50mM Tris-HCl pH7.4, 150mM NaCl, 1mM

MgCl₂; 0.05% NP40) and resuspended in the same buffer. Beads were distributed in different tubes, supplemented with twice their initial volume of NT2 Buffer. The DHX30 specific antibody (5 µg, Abcam, Cambridge, UK) or IgGs were added to the beads and incubated for 2 hours on a rotating wheel at 4°C. Lysates were pre-cleared by adding a mix containing ProteinA and ProteinG Dynabeads in equal amounts and incubating for 1 hour at 4°C on a wheel. After placing the tubes on a magnet, supernatants were collected and 1% of their volume was used as input to be directly extracted with TRIzol. The remaining supernatant was added to the antibody-coated beads and incubated overnight on a wheel at 4°C. The day after, beads were resuspended in 1ml NT2 buffer, transferred in a new tube, and washed with 1ml NT2 buffer for 10 minutes on a wheel at 4°C. All the washes were performed on a magnet. Three additional washes were performed again with 1ml NT2 Buffer supplemented with 0.1% Urea + 50mM NaCl (10 minutes each at 4°C on a wheel). Beads were washed one more time in 500µl of NT2 buffer, 50µl were collected for WB analysis and the remaining supernatant was discarded. RNA was extracted by adding TRIzol to the beads, according to the manufacturer's protocol. The RNA pellets were resuspended in 15µl DEPC water and cDNAs were synthesized using the RevertAid First Strand cDNA Synthesis Kit (Thermo Fischer Scientific).

2.11 Cytoplasm-Mitochondria fractionation

For cytoplasm-mitochondria fractionation, 2x10⁶ cells were seeded in P150 Petri dishes and incubated for 2 days. Then, they were detached using trypsin and re-suspended in 750µL of Mitochondrial Isolation Buffer (MIB) (0.32M Sucrose, 1mM EGTA pH 8.0, 20mM Tris-HCl pH 7.2) with 0.1% fatty acid-free BSA. Cells were homogenized in a Potter-Elvehjem homogenizer (DWK Life Sciences, Mainz, Germany) applying more than 60 strokes. Homogenate (A) was centrifuged for 5 minutes at 1000g at 4°C and supernatant was collected. Cell debris were re-suspended in 750µL of MIB + BSA and re-homogenized with more than 20 strokes. New homogenate (B) was centrifuged for 5 minutes at 1000g at 4°C and the supernatant was collected and pooled with supernatant A. Two mixed supernatants (A+B) were centrifuged at 12000g for 10 minutes at 4°C to pellet the mitochondria. The supernatant was discarded and mitochondria were washed twice with 1mL of MIB + BSA and once with 1mL of MIB, centrifuging the mitochondria pellet every time at 12000g for 10 minutes at 4°C. Finally, the supernatant was discarded and

mitochondria were lysed in RIPA buffer and mitochondrial proteins were quantified by BCA assay.

2.12 Flow cytometry apoptosis analysis

Apoptosis analysis was based on FITC Annexin-V Apoptosis Detection Kit protocol (BD Biosciences, San Jose, CA, USA). Briefly, 3×10^5 cells/well were seeded in a 6-well plate, incubated for one day, and then treated with drugs under investigation for 48 hours. 0.1% DMSO was used as the negative control. Cells were detached using trypsin and washed twice with PBS 1X. Then, 1.5×10^5 cells were re-suspended in 100 μ L of Binding Buffer 1X, stained with FITC-Annexin V and PI, and incubated for 15 minutes at room temperature in the dark. Finally, samples were analyzed by FACSCanto™ flow cytometer and BD Diva Software 6.1.3. Unstained, PI-only, and FITC-only stained samples were used to set the cytometer's parameters.

2.13 Exploration of TGCA data using the GEPIA web resource

The GEPIA API (Tang Z. *et al.*, 2019) was used to extract correlations between DHX30 and mitochondrial genes (either as individual genes or for the 14-genes signature) in all available tumor datasets (correlation mode). Survival analysis was performed with the same tool and in the same datasets, using the survival mode. Only results within the p-value threshold of 0.05 were considered, with the others being set to R=0 and HR=1 in the heatmap for visualization purposes.

2.14 Statistical analysis

Data are presented as mean \pm SD of three independent biological experiments. GraphPad Prism 5 software (GraphPad Software, La Jolla, CA, USA) was used and a two-tailed Student's t-test was performed, unless specified otherwise. Statistical significance was indicated as: *p < 0.05; **p < 0.01; ***p < 0.001.

Chapter 3: Results

3.1 Silencing of DHX30 enhances translation in the HCT116 colorectal cancer cell line.

The RNA-seq data analysis and GSEA were performed by Erik Dassi, CIBIO.

In previous work from our laboratory, we identified DHX30 as an RNA-binding protein able to negatively modulate p53-dependent apoptosis. That result was obtained starting from polysomal profiling experiments followed by RNA-sequencing using HCT116 cell clones stably depleted for DHX30 (shDHX30) and treated with the MDM2 inhibitor Nutlin-3 (Rizzoto D *et al*, 2020). In this thesis work, I started from re-analyzing the gene expression changes but instead of examining the impact of the Nutlin treatment, I focused on the comparison between DHX30-depleted and control (shNT) HCT116 cells in the untreated condition, intending to explore the constitutive effect that the depletion of this RNA-binding protein has on gene expression and, particularly, on translation efficiency. Gene set enrichment analysis (GSEA) revealed a clear enrichment for ribosomal genes at the polysomal level, with a positive normalized enrichment score (**Figure 3.1a**). Consistently, analysis of translation efficiency (TE), measured as the ratio between relative RNA abundance in polysomal and total fractions, revealed that DHX30 depletion is associated with higher TE for transcripts coding for ribosomal protein subunits (RPL, RPS, **Figure 3.1b**). Interestingly, HCT116_shDHX30 showed a reduced TE of transcripts coding for nuclear-encoded mitochondrial ribosomal proteins compared to the shNT control clone. It was also apparent that cytoplasmic and mitochondrial ribosome protein genes exhibited different intrinsic translation efficiency, that was lower for the cytoplasmic ribosomal transcripts (RPL, RPS, **Figure 3.1b**).

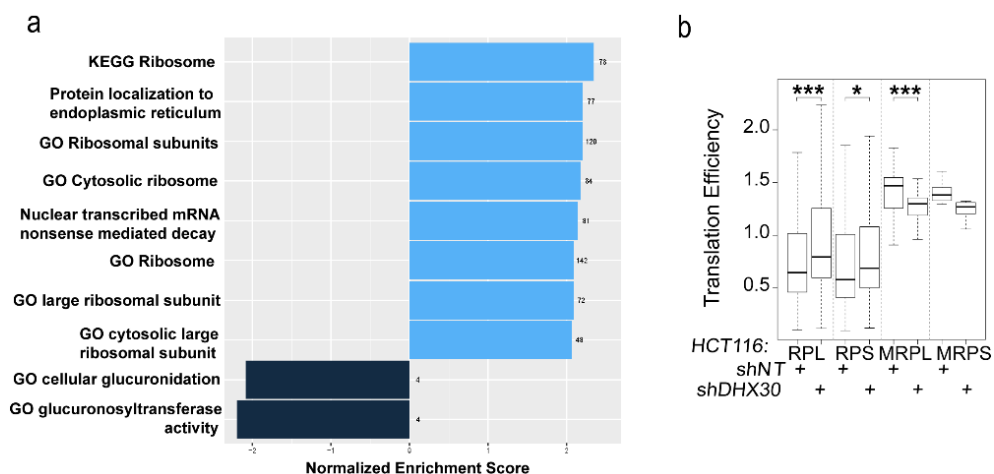


Figure 3.1: Bio-informatic analysis of RNA sequencing data. a) Most significant terms by GSEA along with the number of modulated genes in each pathway. b) Translation Efficiency (TE) was calculated from the RNA-seq normalized read counts obtained in polysomal over total RNA. Presented is the data for ribosome and mito-ribosome components, grouped by large or small subunits and for HCT116 control or stably depleted clones, as indicated. * $p < 0.05$; *** $p < 0.001$.

We then sought to understand if DHX30 could be directly regulating this class of genes, and exploited the DHX30 eCLIP data in ENCODE done in K562 cells (Van Nostrand EL *et al*, 2016). Although based on a different cell line, the eCLIP data indicate that DHX30 can bind 67 ribosomal (36 RPLs and 31 RPSs) and 23 mitoribosomal (16 MRPLs and 7 MRPSs) protein transcripts (Van Nostrand EL *et al*, 2016).

Consistent with the higher TE for RPL and RPS transcripts in HCT116_shDHX30 clone, these cells showed also a higher number of cytoplasmic ribosomes, extracted and quantified from a sucrose cushion (**Figure 3.2**), following an established protocol (Belin S *et al*, 2010).

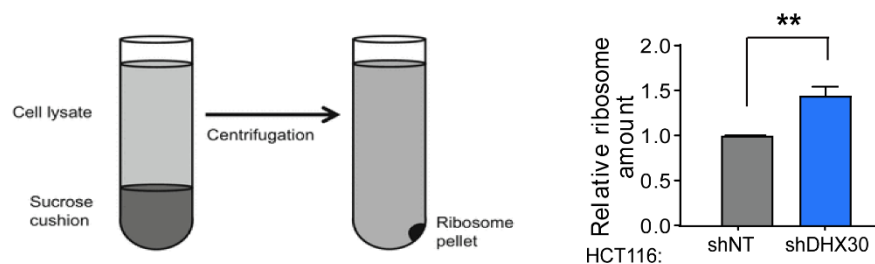


Figure 3.2: Amount of cytoplasmic ribosome produced in HCT116_shDHX30 and HCT116_shNT. Data are normalized on shNT and are mean \pm SD (n=3); * $p < 0.05$.

To confirm this data, we analyzed the production of ribosomal rRNA, estimated based on the fluorescence intensity of 5-Ethyluridine (5-EU) incorporated in nascent rRNAs present in the nucleoli. Actinomycin-D, a molecule able to inhibit RNA polymerase I, was used as a control treatment. Consistent with the higher amounts of ribosomes, DHX30 depletion in HCT116 cells was associated with higher relative amounts of rRNA levels (**Figure 3.3a**). To investigate also a specific ribosomal RNA, I performed a Fluorescent In Situ Hybridization (FISH) using probes able to hybridize the 18S rRNA. Quantifying the fluorescent intensity in nucleoli a higher amount was found in HCT_shDHX30 compared to shNT (**Figure 3.3b**).

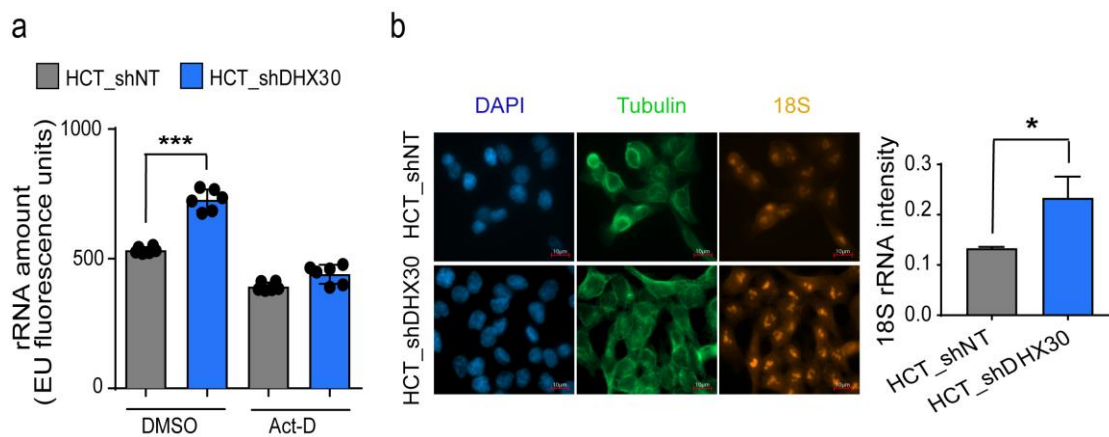


Figure 3.3: rRNA production in HCT116_shDHX30. **a)** Amount of ribosomal RNA based on 5-EU incorporated in nascent rRNA by click-it chemistry reaction. Data are mean \pm SD (n=3); *p < 0.05 **b)** (Left) Representative images of one of three independent experiments of FISH for rRNA precursor 18S. (Right) Box plot of 18S rRNA intensity Data are mean \pm SD (n=30 nucleoli in three biological replicates for each cell line); *p < 0.05

To study how the increase in ribosome components found in HCT116 depleted for DHX30 affects cell translation, we performed a global translation analysis based on the fluorescence intensity of L-azidohomoalanine incorporated in nascent proteins present in the cytoplasm. The analysis was performed in untreated conditions while 100mM of 5-Fluorouracil treatment was used as a control treatment that reduces global translation. Interestingly, we found that DHX30-depleted cells not only showed evidence of increased ribosome biogenesis but also of higher global translation (**Figure 3.4a**). This result was confirmed also exploiting the polysome fractionation on sucrose gradients. Indeed, the area under the curve of fractions corresponding to the polysomes relative to the fractions corresponding to the ribosomal subunits and the 80S monosome (POL/SUB ratio) is considered an estimate of translation efficiency and is higher in DHX30-depleted cells (**Figure 3.4b**). Finally, by again exploiting polysome fractionations on linear 15-50% sucrose gradients followed by protein extraction from each fraction and western blotting, DHX30 protein was found associated with ribosomal subunits, 80S monosomes as well as with polysomes in HCT116 cells (**Figure 3.4c**).

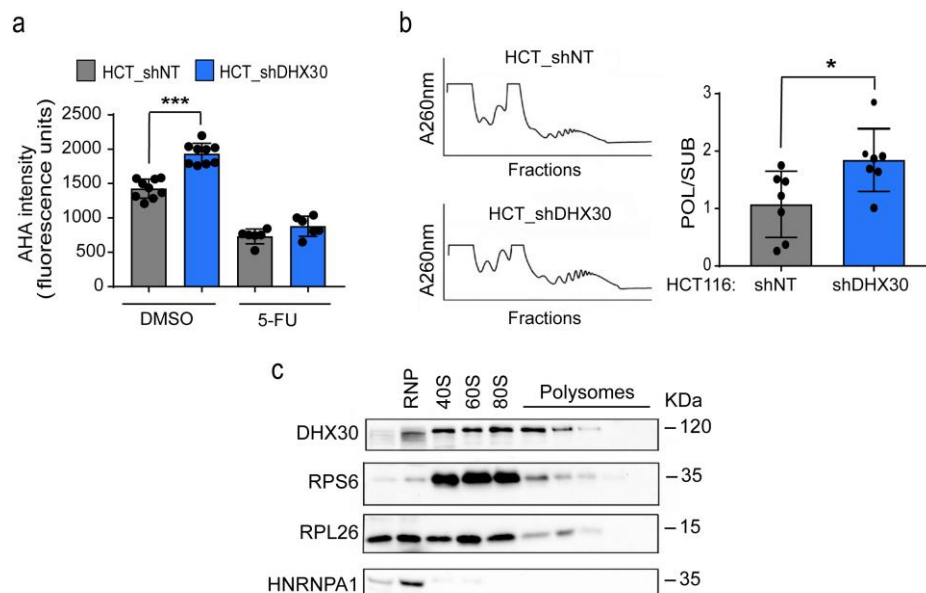


Figure 3.4: Analysis of translation in DHX30-depleted HCT116 cells. **a)** Analysis of AHA click-it chemistry to analyse global translation in HCT116_shDHX30 cells compared to the shNT control clone. 100mM of 5-FU was used as positive control. Data are mean \pm SD (n=6 to 9); ***p < 0.005. **b)** (Left) Polysome profiling of HCT_shDHX30 and HCT_shNT, revealed by the measurement of absorbance at a wavelength of 260 nm. (Right) Box plot of the relative quantification of the area under the curve. Data are mean \pm SD (n=7); *p < 0.05. **c)** Western blot to visualize DHX30 in the different fractions of polysome profiling. RPS6, RPL26 and HNRNPA1 were used as controls.

From those data, and inferring from the effect of DHX30 depletion by shRNAs I propose that DHX30 can act to negatively influence ribosome biogenesis as well as global translation. In a previous study from the lab, DHX30 was linked to the modulation of the translation of specific mRNAs, acting via a target cis-element (Rizzotto *et al.*, 2020). It is important to emphasize that effects on global and specific translation are not necessarily two dissociated events. Indeed, a change in ribosome number can lead also to changes in mRNA translation specificity (Mauro VP *et al.*, 2016).

3.2 DHX30 silencing negatively impacts on the expression of nuclear encoded mito-ribosome components

The impact of DHX30 depletion on the expression and translation efficiency of nuclear encoded mito-ribosomal proteins caught our attention, as it showed the opposite trend compared to ribosomal protein transcripts (**Figure 3.1b**). Initially, we

established the potential for DHX30 to bind to MRPL11 and MRPS22 transcripts by an RNA immunoprecipitation (RIP) assay. In this experiment, we compared DHX30 (blue bar) to IgG (grey bar) which was used as a negative control. Data are presented as % of input and the 1% level is highlighted (dashed line). Interestingly, we found that DHX30 bound both MRPL11 and MRPS22, although the latter with a higher apparent affinity (**Figure 3.5a**). Furthermore, in DHX30-depleted HCT116 cells, MRPL11 and MRPS22 expression were reduced both at transcript and protein levels, compared to shNT control cells (**Figure 3.5b, c**).

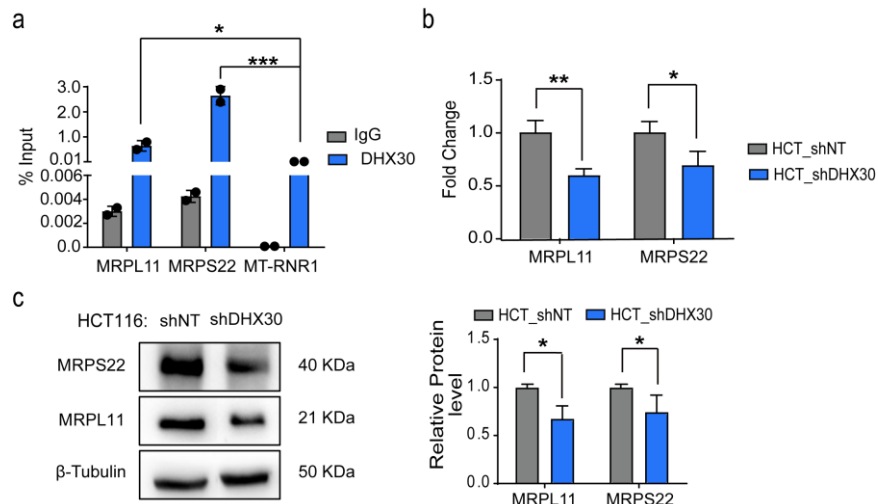


Figure 3.5: DHX30 impacts on nuclear encoded mito-ribosome components. a) RNA immunoprecipitation experiments to study the binding of DHX30 to MRPL11 and MRPS22 transcripts [performed in collaboration with Annalisa Rossi]. Results obtained with a primary antibody targeting DHX30 (blue) or the IgG control (grey) are plotted relative as % of input. Data are mean and individual points (n=2); **p < 0.01. **b)** Relative mRNA levels of MRPL11 and MRPS22 in HCT116_shDHX30 compared to the shNT control clone. **c)** (Left) Protein levels of MRPL11 and MRPS22. β -Tubulin was used as loading control. Immunoblots represent one of three independent experiments. (Right) MRPL11 and MRPS22 protein quantification in HCT116_shDHX30 normalized on shNT control clone. In all experiments data are mean \pm SD (n=3); *p < 0.05; **p < 0.01; ***p < 0.001.

3.2.1 Impact of cytoplasmic and mitochondrial DHX30 variants on the expression of mito-ribosome components in HCT116 p53^{+/+} and p53^{-/-}

The data obtained in the previous paragraph suggest that DHX30 directly promotes stability and/or translation of mito-ribosome transcripts. This feature could impact on mitochondrial translation and contribute to the functions previously described for DHX30 as a protein present in the mitochondrial matrix (Antonicka H *et al.*, 2015;

Wang Y and Bogenhagen DF, 2006). Indeed, the DHX30 gene comprises two promoters, and the transcript resulting from the internal one features an alternative first exon that contains a predicted mitochondrial localization signal (DHX30-207), not present in the DHX30 cytoplasmic variants (DHX30-201, DHX30-205) (**Figure 3.6a**). Indeed, mitochondrial localization in HCT116 cells was confirmed by immunofluorescence co-localizing DHX30 (red) with the mitochondrial protein MT-ATP6 (green), a component of ATP synthase (**Figure 3.6b**), as was established in human fibroblasts (Antonicka H *et al.*, 2015) and is also consistent with APEX-seq data (Fazal FM *et al.*, 2019). Next, using primers specifically designed for the two variants, the expression of either cytoplasmic or mitochondrial DHX30 transcripts was checked by real-time PCR. We found that the level of mitochondrial DHX30 (mDHX30) is about four times higher than the cytoplasmic variant (cDHX30) (**Figure 3.6c**). Since this comparison may be biased by slight differences in amplification efficiency of the two DHX30 isoform primer pairs used, and since the two isoforms have a similar molecular weight and cannot be resolved by a canonical western blot, I confirmed the result also at the protein level by cytoplasm-mitochondria fractionation followed by a western blot in HCT116 cells, using β -Tubulin and MT-ATP6 as controls of cytoplasmic and mitochondrial fractionation, respectively, and Ponceau-S staining as a loading/transfer control (**Figure 3.6d**).

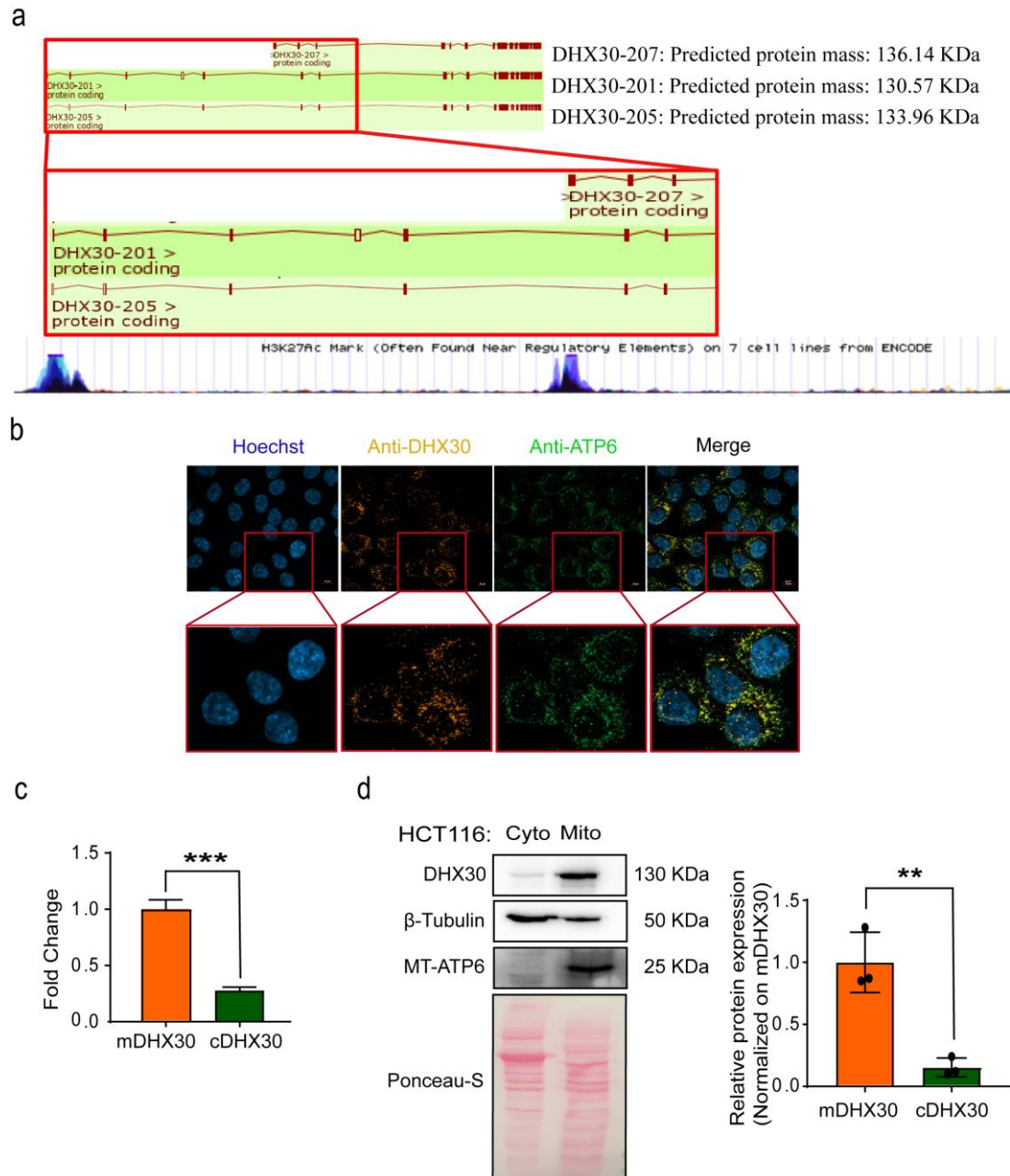


Figure 3.6: DHX30 localization and abundance in cellular compartments. **a)** (Upper panel) Cartoon of mitochondrial and cytoplasmic DHX30 isoforms and their predicted protein masses. (Lower panel) Acetylation of lysine on histone H3 analysis performed by Encode that indicates the presence of active promoters. **b)** Representative images of immunofluorescence to co-localize DHX30 (red) with MT-ATP6 (green). Staining with Hoechst was used to visualise nuclei. **c)** Relative mRNA levels of cytoplasmic DHX30 (cDHX30) and the mitochondrial variant (mDHX30, set to 1). Data are mean \pm SD (n=3); ***p < 0.005. **d)** (Left) Representative western blot of cytoplasm-mitochondria fractionation. One of three independent experiments is shown. (Right) Relative quantification of DHX30 protein levels in cytoplasm and mitochondria normalized on mDHX30.

The shRNA that we used to obtain stably depleted cells targeted both cytoplasmic and mitochondrial DHX30 transcripts (**Figure 3.7a**). To confirm the effect of DHX30

depletion on mito-ribosome genes, excluding possible adaptations that may have occurred during the selection of the stable shRNAs clones, we employed transient silencing using one validated siRNA specific for cytoplasmic DHX30 (siDHX30-C) or one validated siRNA targeting transcripts from both promoters (siDHX30-C+M). Then, the same experiment was performed also in p53 knock-out HCT116 cells (HCT116 p53^{-/-}) to explore if p53 status could play a role in the functions regulated by DHX30. The activity and specificity of the two siRNAs were confirmed by qRT-PCR (**Figure 3.7b** and **c**).

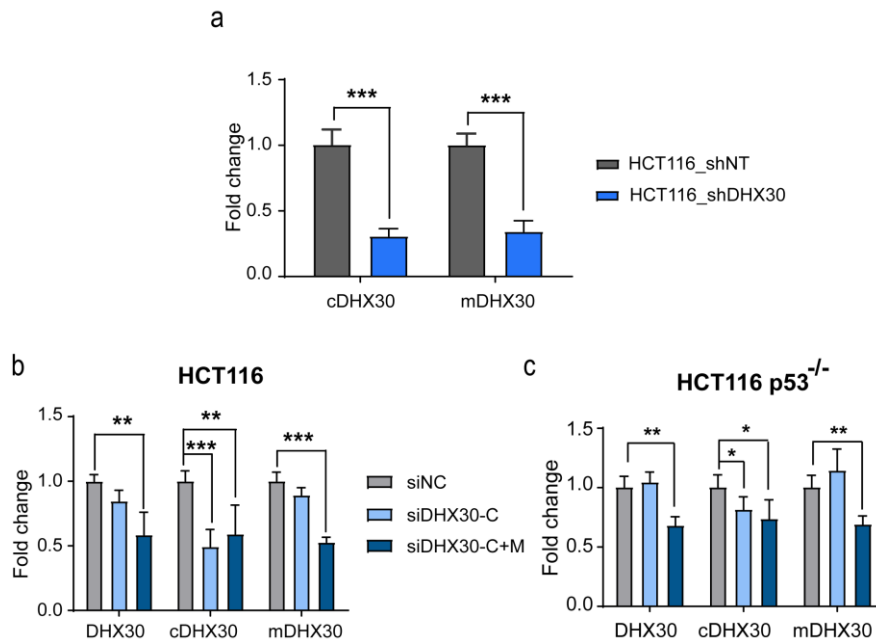


Figure 3.7: Control of stable and transient silencing in colorectal cancer cell lines. **a)** Relative mRNA levels of cytoplasmic (cDHX30) and mitochondrial (mDHX30) DHX30 transcript variants in HCT116_shDHX30 compared to the shNT control clone. **b)** and **c)** qRT-PCR to verify the transient silencing of DHX30 variants in **b)** HCT116 and **c)** HCT116 p53^{-/-} after 96 hours post transfection, using primers annealing to: (i) a portion of the coding sequence that is present in all transcript variants (DHX30); (ii) the first exon specific of cytoplasmic DHX30 (cDHX30) or (iii) the alternative first exon specific of mitochondrial DHX30 (mDHX30). All experiments data are analysed 96 hours post silencing and are mean \pm SD (n=3); *p<0.05; **p < 0.01; ***p < 0.001.

We noticed that although the siRNAs depleted DHX30 variants, the efficiency was lower compared to the shRNAs. This could be due to the transient transfection efficiency in HCT116. Exploiting the transient silencing of DHX30 variants in HCT116, I then checked MRPS22 and MRPL11 expression. Consistent with the results obtained with stable silencing of DHX30, qRT-PCR and western blots showed the reduction of mito-ribosome components when both cytoplasmic and

mitochondrial variants of DHX30 were transiently silenced (HCT_siDHX30-C+M) (**Figure 3.8a** and **b**) compared to the siRNA non-targeting control (HCT_siNC). Interestingly, in the p53 knock-out derivative cell line, MRPS22 and MRPL11 expression was not reduced by transient DHX30 depletion either at transcript nor protein level (**Figure 3.8c** and **d**), suggesting that p53 could also play a role, although the mechanism remains elusive. As a note of caution in this regard, it was apparent, that the efficacy of DHX30 transient silencing in HCT116 p53^{-/-} cells was slightly lower compared to the parental cells (**Figure 3.7b, c**).

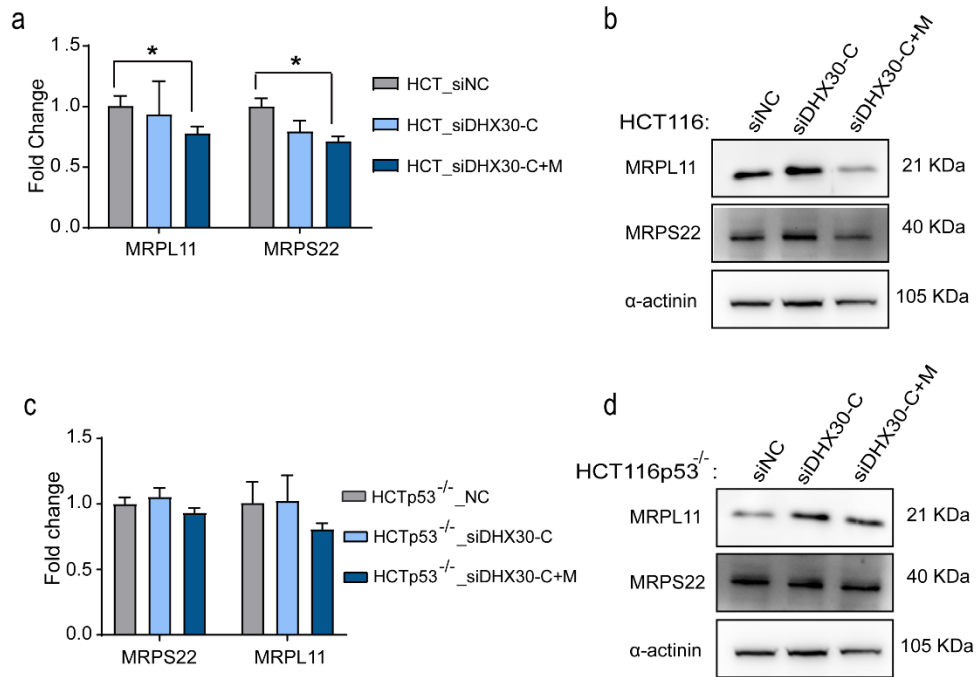


Figure 3.8: Transient silencing of DHX30 confirms the expression reduction of mito-ribosome components but only in wild-type p53 cell. **a)** mRNA and **b)** representative western blot of MRPL11 and MRPS22 in HCT116 silenced transiently for cytoplasmic DHX30 (HCT_siDHX30-C) or for both cytoplasmic and mitochondrial variants (HCT_siDHX30-C+M) for 96 hours. RT-qPCR data are compared to the siRNA negative control (HCT_siNC) and are mean \pm SD (n=3); *p < 0.05. **c)** mRNA and **d)** representative western blot of MRPL11 and MRPS22 protein levels in HCT116 p53^{-/-} silenced for cytoplasmic DHX30 (HCT_siDHX30-C) or for both cytoplasmic and mitochondrial variants (HCT_siDHX30-C+M). RT-qPCR data are compared to the siRNA negative control (HCT_siNC) and are mean \pm SD (n=3)

3.3 Impact of cytoplasmic and mitochondrial DHX30 variants on the expression of oxidative phosphorylation (OXPHOS) components.

Since DHX30 depletion impaired the expression of mito-ribosome components among which I validated MRPL11 and MRPS22, and since the gene, through an alternative promoter and alternative first exon, codes also for a mitochondrial variant, we next explored if and how DHX30 regulates expression of mitochondrially encoded genes. First of all, using digital PCR and two primers for the mitochondrial genes MT-RNR1 MT-ATP8, we established that DHX30 depletion did not impact on the number of mitochondrial genome copy numbers using droplet digital PCR (**Figure 3.9a**). The diploid marker gene CTDSP1 was used as an internal control of the experiment. While digital PCR provides a quantitative relative measure of mitochondrial genomes, we cannot exclude that mitochondrial fission/fusion cycles are affected by DHX30 depletion, as the visualization of mitochondria we did use imaging techniques (**Figure 3.6** and data not shown) offered a limited resolution. Next, we focused on gene expression analysis of mitochondrially encoded genes. The mitochondrial genome (mtDNA) is a 16.569 circular DNA that contains the genes for 13 proteins involved in oxidative phosphorylation (OXPHOS): seven complex I (NADH dehydrogenase) subunits MT-ND1, 2, 3, 4, 4L, 5 and 6; one complex III subunit MT-CYB; three complex IV components MT-CO1, 2 and 3; and two complex V subunits MT-ATP6 and 8. Besides, mtDNA contains also 2 rRNAs (MT-RNR1 and -RNR2) and 22 tRNAs (**Figure 3.9b**). These genes do not have introns and are polycystronically transcribed from a promoter located in the control region of the two strands of the mitochondrial genome. Transcripts are then cleaved and polyadenylated (Taanman JW, 1999). Interestingly, the expression of at least 10 out of 13 mitochondrially encoded coding transcripts was reduced in HCT116_shDHX30 (**Figure 3.9c**). Consistently, the steady-state expression of two mitochondrially encoded proteins, MT-ATP6 and MT-ATP8, analyzed by immunoblotting after cytoplasm-mitochondria fractionation, or by immunofluorescence, was shown to be reduced in DHX30-depleted HCT116 cells (**Figure 3.9d** and **e**). These results predict an impact on ATP production as the two proteins are subunits of complex V (ATP synthase).

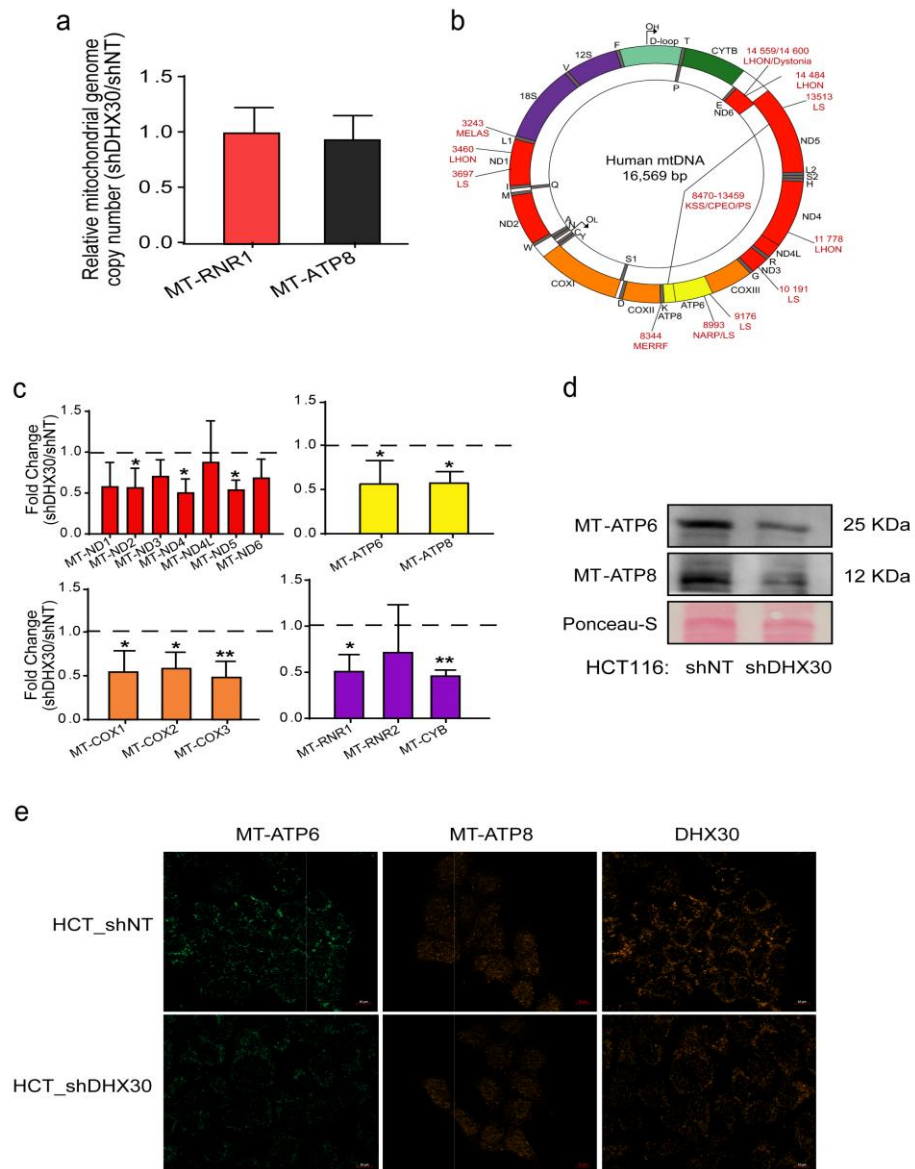


Figure 3.9: DHX30 impacts on mitochondrially encoded oxidative phosphorylation (OXPHOS) components. **a)** Relative mitochondrial genome copy number in HCT116_shDHX30 and -shNT measured by droplet digital PCR. MT-RNR1 and MT-ATP8 were amplified along with the nuclear diploid marker gene CTDSP1. Bars plot mean \pm SD (n=3). Digital PCR experiments were developed with contributions from Viktoriya Sidarovich and Pamela Gatto, CIBIO HTS core facility. **b)** Mammalian mitochondrial genome included 13 mitochondrially encoded genes and 2 rRNA (Nissanka N *et al*, 2018). **c)** Relative mRNA levels of mitochondrially encoded OXPHOS components in HCT116_shDHX30 compared to HCT116_shNT (dashed line, set to 1). Data are mean \pm SD (n=3); *p < 0.05; **p < 0.01. **d)** Protein levels of MT-ATP6 and MT-ATP8 in mitochondrial lysates of HCT116_shDHX30 and the shNT control clone. Ponceau-S was used as loading control. Immunoblots represent one of three independent experiments. **e)** Representative images of one of three independent immunofluorescence experiments to visualize DHX30, MT-ATP8 (red), or MT-ATP6 (green) expression in HCT116_shDHX30 and HCT116_shNT.

To explore the mechanism by which DHX30 could impact on mito-ribosome transcripts' expression, RNA-immunoprecipitation experiments were performed to evaluate the possibility of direct interaction between DHX30 and mitochondrially encoded transcripts. Contrary to previous reports in human fibroblasts (Antonicka H *et al.*, 2015), we did not obtain strong evidence for direct DHX30 binding to those transcripts in native conditions (**Figure 3.10, right panel**), except when a UV crosslinking step was introduced before cell lysis and immunoprecipitation (**Figure 3.10, left panel**).

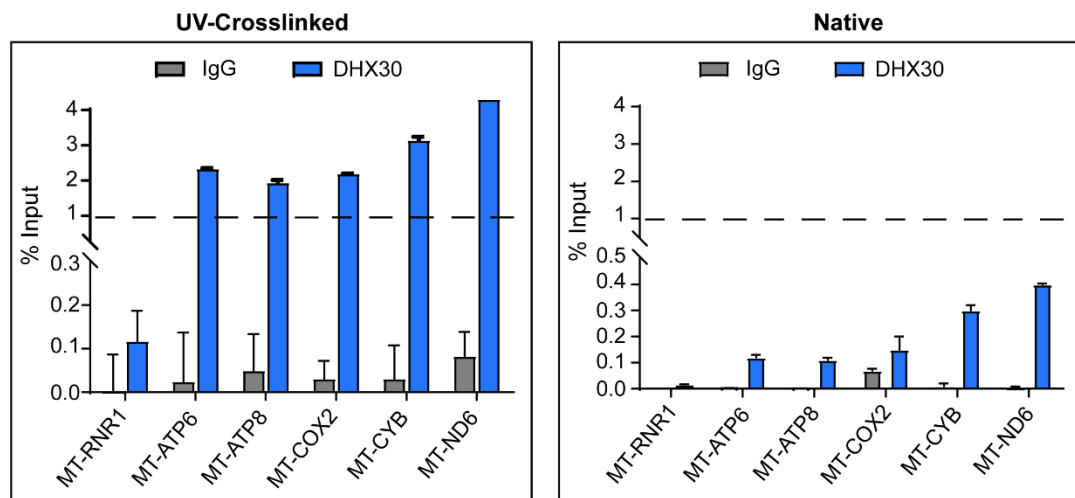


Figure 3.10: DHX30 directly bind mitochondrially encoded transcripts only with UV-crosslinking. RNA immunoprecipitation (RIP) experiments, performed in collaboration with Annalisa Rossi, to study the binding of DHX30 to mitochondrially encoded OXPHOS components transcripts with (Left) or without (Right) UV-crosslinking. Results obtained with a primary antibody targeting DHX30 (blue) or the IgG control (grey) are plotted relative to the input (1%, dashed line). Data are mean \pm SD (n=2 biological replicates with three technical replicates each for the native condition on the right, while only 1 experiment was performed with UV-crosslinking -left-)

Finally, we evaluated markers of carbon metabolism and mitochondrial respiration capacity by an Agilent Seahorse XF real-time analyzer. We found that HCT116_shDHX30 cells had a significantly lower basal oxygen consumption rate compared to the control cell line. Notably, DHX30-depleted cells did not show compensatory glycolysis in basal culture condition and not even when we chemically abolished mitochondrial respiration; in fact, we observed lower compensatory glycolysis compared with the control (**Figure 3.11**). These findings suggest that HCT116_shDHX30 cells do not show a typical Warburg effect (Heiden MG *et al.*,

2009), usually expected when cancer cells produce less energy due to reduced mitochondrial respiration, resulting in a lower energetic phenotype.

Collectively, depletion of DHX30 seems to generate an apparent imbalance in cell homeostasis, with higher demand of chemical energy from ribosome biogenesis and cytoplasmic translation, but lower mitochondrial activity.

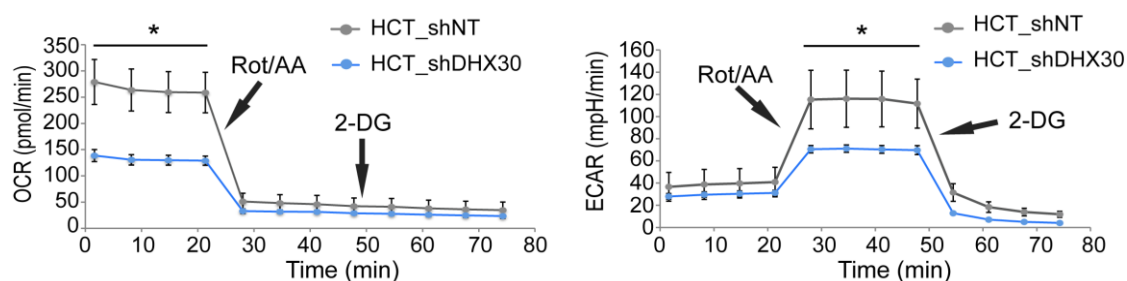


Figure 3.11: DHX30 depletion reduce mitochondrial respiration and compensatory glycolysis in HCT116 cancer cell line. (Left) Measurement of the oxygen consumption rate (OCR) to evaluate mitochondrial respiration by Seahorse XF analyzer. Points before the Rotenone/Antimycin-A (Rot/AA) treatment correspond to the basal mitochondrial respiration. (Right) Extracellular acidification rate measurement was used as a means to measure glycolysis. Points before and after the Rotenone/Antimycin-A (Rot/AA) treatment correspond respectively to basal and compensatory glycolysis -in response to the block of mitochondrial respiration-. 2-Deoxyglucose (2-DG) is then used to block glycolysis. For both panels, one of three independent replicates is presented. Data are mean \pm SD (n=3 wells in the Seahorse cartridge); *p < 0.05.

Using the same approach described in chapter 3.2.1, DHX30 variants were transiently silenced in HCT p53^{+/+} and HCT p53^{-/-} to confirm the resulting modulation in the expression of mitochondrially encoded genes and explore if p53 status could also play a role in this process. Initially, cytoplasmic or cytoplasmic + mitochondrial DHX30 were silenced and the expression of mitochondrially encoded genes was observed by qRT-PCR after 96h post DHX30 silencing. Although DHX30 depletion was visible already after 48 hours from the addition of the siRNAs (not shown), more time was needed to appreciate a reduction in the expression of mitochondrially encoded genes. The analysis after transient silencing in HCT p53^{+/+} confirmed their lower expression, while, interestingly, in the p53 knock-out clone, silencing of DHX30 did not affect the expression of OXPHOS components at both RNA and protein levels. (**Figure 3.12**). The effect observed could open a window on different cytoplasmic and mitochondrial DHX30 functions. Indeed, it seems that the silencing of cytoplasmic DHX30 affects the expression of nuclear-encoded mitoribosome components, playing a role in the formation of correct mitoribosomes. Instead, silencing of also

mitochondrial DHX30 isoform impacts the transcription of mitochondrially encoded OXPHOS genes, affecting the correct formation of OXPHOS machinery. The apparent p53 dependence of these effects remains to be explored.

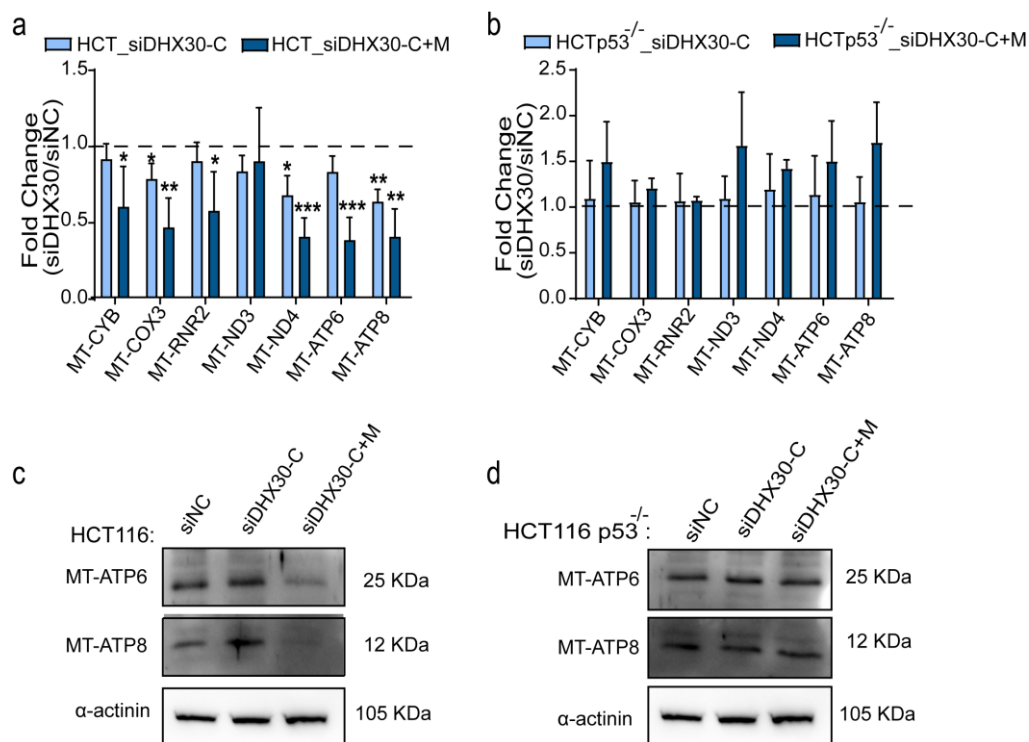


Figure 3.12: DHX30 depletion decrease the expression of mitochondrially encoded OXPHOS components but only in when p53 is present. a) and b) Relative mRNA levels of the indicated mitochondrially encoded OXPHOS components in a) HCT116 p53^{+/+} and b) HCT116 p53^{-/-} transiently silenced for DHX30 expression (siDHX30-C, siDHX30-C+M) compared to siNC (dashed line, set to 1) for 96 hours. Data are mean \pm SD (n=3); *p < 0.05; **p < 0.01; ***p < 0.001. c) and d) Protein levels of MT-ATP6 and MT-ATP8 in c) HCT116 p53^{+/+} and d) HCT116 p53^{-/-} transiently silenced for DHX30 variants. α -actinin was used as loading control. Immunoblots represent one of three independent experiments.

3.4 Silencing of DHX30 impaires cell proliferation rate and increases apoptosis proneness

Next, I characterized the impact of DHX30 depletion on HCT116 cell growth. Consistent with the lower mitochondrial oxygen consumption rate, HCT116_shDHX30 cells showed a significantly lower proliferation rate compared to the control clone. This was observed by colony formation assay and confirmed by time-course proliferation measured by cell count via high-content microscopy or by using a Real-Time Cell Analyser Xcelligence (Figure 3.13a, b, and c). Interestingly,

this effect on proliferation is maintained also in a 3D culture. Indeed, I observed a reduction in proliferation caused by DHX30 silencing also in a spheroid assay (**Figure 3.13d**). The lower growth rate in DHX30 depleted cells cannot be attributed to an arrest in a particular phase of the cell cycle (**Figure 3.13e** -the slight increase in the proportion of G1 is not significant-) but could be due to the lower amount of energy that those cells have, causing a slower cell cycle compared to the control. Interestingly, DHX30 depletion is associated with increase apoptosis after 48 hours of treatment not only with Nutlin, as expected by our previous results (Rizzotto D *et al*, 2020), but also when cells were treated with the topoisomerase inhibitor doxorubicin, and particularly with FCCP, an agent that causes mitochondrial membrane depolarization (**Figure 3.13f**).

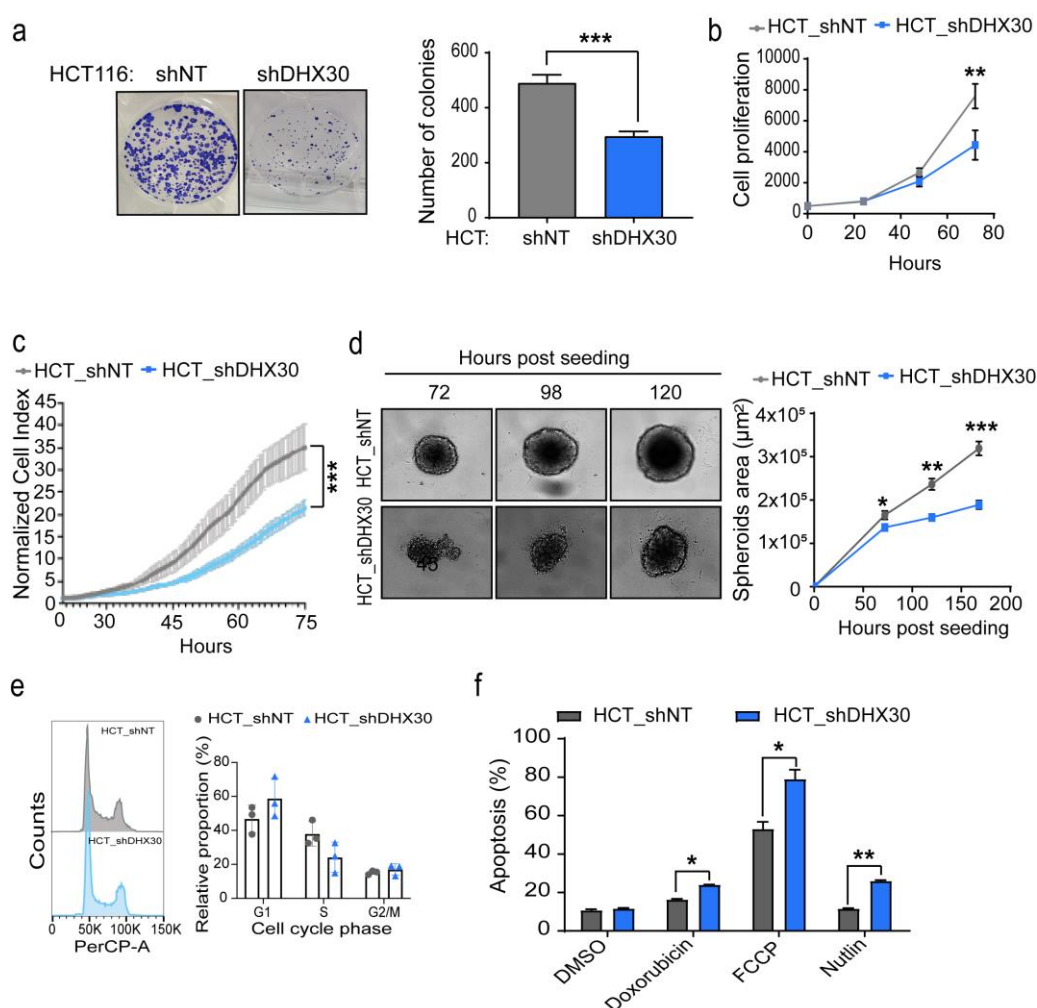


Figure 3.13: DHX30 depletion impaired cell proliferation and enhances apoptosis upon drug treatments. **a)** (Left) Representative image of colony formation assays. (Right) Colony quantification by ImageJ software. Data are mean \pm SD (n=3). **b)** Relative cell proliferation measured by high-content microscopy in digital phase contrast. Data are mean \pm SD (n=3). **c)** Estimate of relative proliferation by an impedance-based Real-Time Cell Analyser. Data are mean \pm SD (n=3). **d)**

Spheroid formation and growth assay. (Left) A representative image at the indicated time points is shown in the left panel. (Right) Spheroid area measured by ImageJ software. Data are mean \pm SD (n=3). **e)** (Left) Representative image of HCT116_shNT and shDHX30 cell cycle profile performed by Dario Rizzotto. (Right) Quantification of cell cycle profile in HCT116 DHX30 depleted cells compared to shNT control. Data are mean \pm SD (n=3). **f)** Relative expression of the Annexin-V apoptosis markers in cells treated for 48 hours with the indicated drugs or DMSO control. For all panels, data are mean \pm SD (n=3); *p < 0.05; **p < 0.01; ***p < 0.001.

3.5 Impact of DHX30 depletion in other cell line models

To investigate if DHX30 has a common role in translation and metabolism in additional cell models, I transiently silenced cytoplasmic and mitochondrial DHX30 in U2OS osteosarcoma and MCF7 breast cancer cell lines, and I studied the effect of its silencing in those cells. First, DHX30 silencing was confirmed by qRT-PCR. We can observe that in U2OS siRNAs worked as expected, silencing the specific DHX30 transcript variant they target, like in HCT116. Instead, in MCF7 it seems that siDHX30-C silenced both mitochondrial and cytoplasmic variants (**Figure 3.14a** and **b**). This result was unexpected, as the relative expression of DHX30 in MCF7 was only slightly lower compared to what we observed in HCT116 cells, and since mDHX30 was about four times more abundant than cDHX30 also in MCF7 cells. Given, this unexplained result -for which a technical error cannot be excluded-, in subsequent experiments in MCF7 I will present only the results obtained with the siDHX30-C+M.

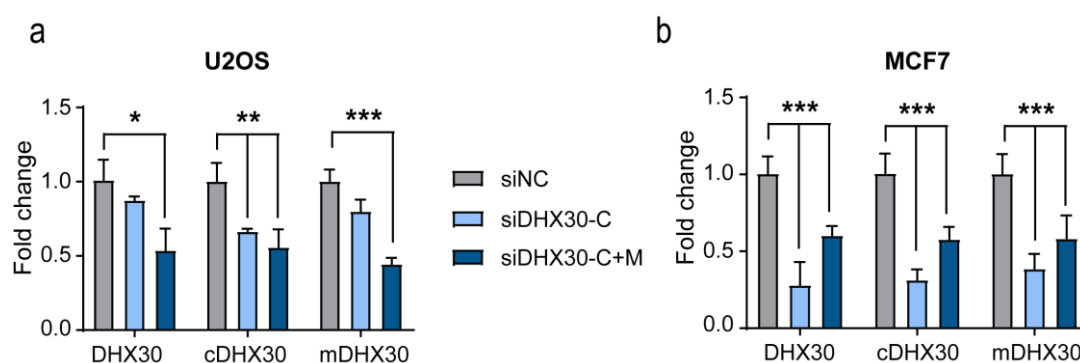


Figure 3.14: Efficacy of transient silencing of DHX30 in U2OS and MCF7. **a)** and **b)** qRT-PCR to verify the transient silencing of DHX30 in A) U2OS and B) MCF7 using primers annealing to: (i) a portion of the coding sequence that is present in all transcript variants (DHX30); (ii) the first exon specific of cytoplasmic DHX30

(cDHX30) or (iii) the alternative first exon specific of mitochondrial DHX30 (mDHX30). Experiments are performed after 96 hours post silencing and data are mean \pm SD (n=3); *p < 0.05; **p < 0.01; ***p < 0.001.

First, I explored the impact of DHX30 depletion on the expression of nuclear-encoded mitoribosome components. Surprisingly, only MCF7 cells showed a significant reduction in the expression of MRPL11 when both variants of DHX30 were silenced (siDHX30-C+M), at both mRNA and protein levels. In contrast, I observed for MRPL11 a reduction in protein levels also in U2OS, while MRPS22 did not change compared to the controls in either cell line (**Figure 3.15**).

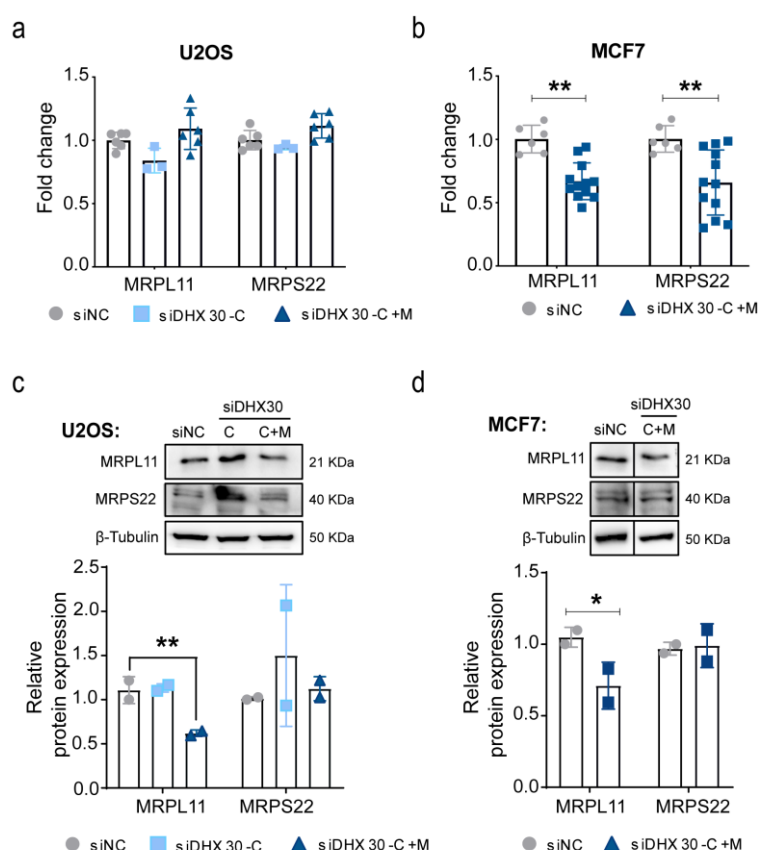


Figure 3.15: The effect of DHX30 depletion on nuclear encoded mitoribosome components in MCF7 and U2OS. **a)** and **b)** qRT-PCR of MRPL11 and MRPS22 in **a)** U2OS and **b)** MCF7 cells transiently silenced for cytoplasmic DHX30 (siDHX30-C) or for both cytoplasmic and mitochondrial variants (siDHX30-C+M). Data are compared to the siRNA negative control (siNC) and are mean \pm SD (n=3); **p < 0.01. **c)** (Upper panel) representative western blot of MRPL11 and MRPS22 in U2OS silenced transiently as in **a)**. (Down panel) Relative protein quantification of nuclear encoded mitoribosome components in U2OS transiently silenced for DHX30. Data are mean \pm SD (n=3); **p < 0.01. **d)** (Upper panel) representative western blot of MRPL11 and MRPS22 in MCF7 silenced transiently for both cytoplasmic and mitochondrial variants (MCF7_siDHX30-C+M). (Down panel) Relative protein

quantification of nuclear encoded mitochondrially encoded components in MCF7 transiently silenced for DHX30. Data are mean \pm SD (n=3); *p < 0.05.

Next, I explored the expression of mitochondrially encoded OXPHOS targets in U2OS and MCF7 DHX30 depleted cells. As observed with MRPL11 and MRPS22, also in this case DHX30 did not appear to play a transcriptional role in mitochondrial target gene expression in U2OS, with the possible exception of MT-RNR1. In fact, the expression even increased for some targets in U2OS_siDHX30-C+M. (**Figure 3.16a** and **c**). This could mean that in those cells, differently from HCT116, DHX30 affects OXPHOS components neither at transcript nor at protein levels. Instead, consistent with what was observed in HCT116, depletion of DHX30 in MCF7 cell line impaired the expression of all OXPHOS components tested by qRT-PCR, with a trend for lower MT-ATP6 protein expression (**Figure 3.16b** and **d**).

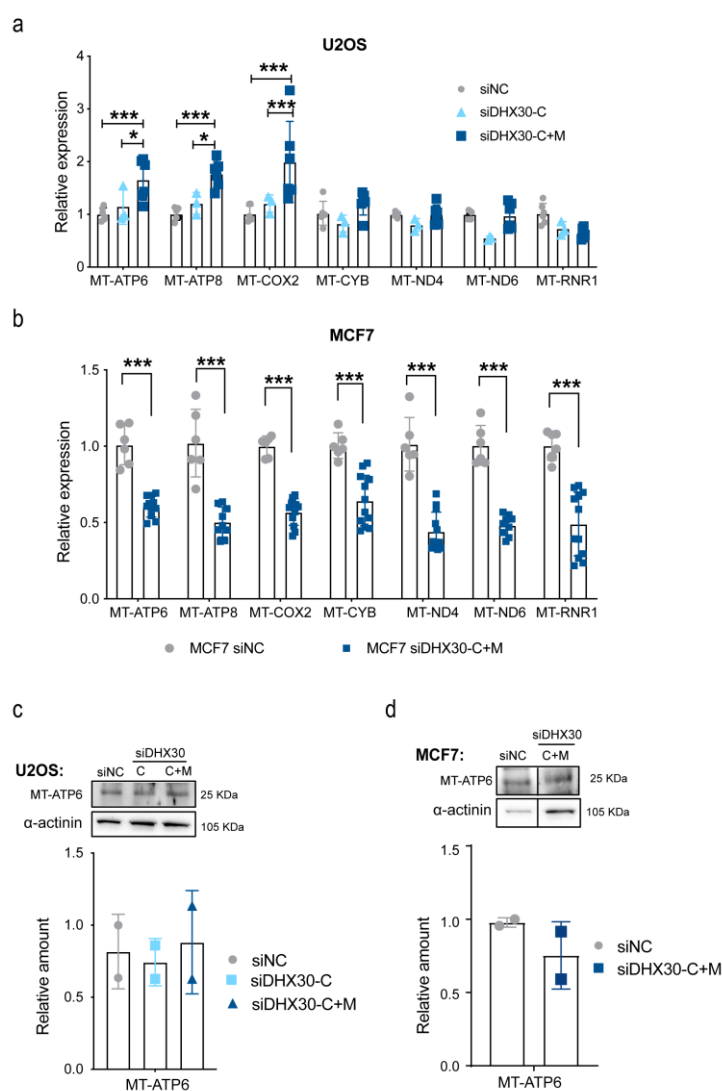


Figure 3.16: The effect of DHX30 depletion on mitochondrially encoded OXPHOS components in MCF7 and U2OS. a) and b) qRT-PCR of selected

mitochondrially encoded genes in a) U2OS and b) MCF7 cells transiently silenced for cytoplasmic DHX30 (siDHX30-C) or for both cytoplasmic and mitochondrial variants (siDHX30-C+M). Data are compared to the siRNA negative control (siNC) and are mean \pm SD (n=3); *p < 0.05; ***p < 0.005. c) (Upper panel) representative western blot of MT-ATP6 in U2OS transiently silenced as in a). (Down panel) Relative protein quantification of MT-ATP6 in U2OS. Data are mean \pm SD (n=3). d) (Upper panel) representative western blot of MT-ATP6 in MCF7 transiently silenced for both cytoplasmic and mitochondrial variants (MCF7_siDHX30-C+M). (Down panel) Relative protein quantification of MT-ATP6. Data are mean \pm SD (n=3)

Consistent with the lower expression of mito-ribosomes components as well as mitochondrial OXPHOS gene expression, MCF7_siDHX30-C+M cells showed a significantly lower proliferation rate compared to the control. In contrast, DHX30 silencing in U2OS did not affect cell proliferation, a result that was consistent with the lack of an impact on mitochondrially encoded OXPHOS components (**Figure 3.17**).

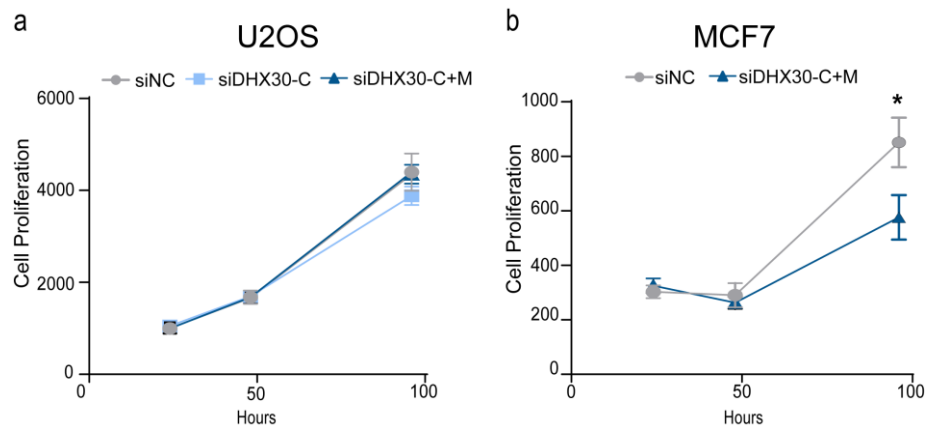


Figure 3.17: Impact of DHX30 depletion in U2OS and MCF7. a) and b) Relative cell proliferation measured by high-content microscopy in digital phase contrast in a) U2OS and b) MCF7 transiently silenced for DHX30 variants. Data are mean \pm SD (n=3); *p < 0.05.

3.6 Expression of DHX30 in human tissues and prognostic significance in human cancer

Our results suggest that DHX30 exerts a constitutive function that improves cellular fitness by balancing energy metabolism and global translation potential. Furthermore, our previous study identified DHX30 as a negative modulator of the translation of specific mRNAs, thus controlling p53-dependent apoptosis (Rizzotto D. *et al.*, 2020). Both these functions suggest that DHX30 could be a modifier of cancer cell

properties potentially impacting clinical variables. Based on those findings, I took a more translational research direction and explored if and how DHX30 expression could be correlated to tumor prognosis. Initially, based on the human protein atlas database (<https://www.proteinatlas.org/>) I found that DHX30 protein expression is high or medium in many tissues, among which brain, lung, testis, liver, colorectal, and others (**Figure 3.18**). Interestingly, organs in which DHX30 is physiologically more abundant are directly correlated to the percentage of patients where high or medium DHX30 protein expression is detected in tumors derived from those tissues, such as Thyroid cancer, Glioma, Colorectal cancer, Liver cancer, Melanoma, Prostate cancer, and others (**Figure 3.19**).

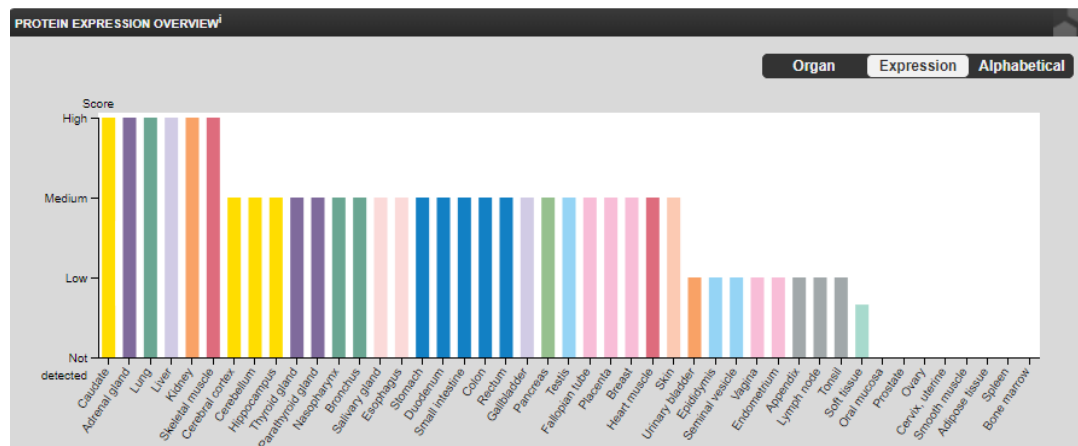


Figure 3.18: DHX30 expression in human tissues. DHX30 protein expression data is shown for each of 44 human tissues. Color-coding is based on tissue groups.

This suggests that DHX30 expression is globally maintained in cancer cells. Although total RNA-seq data are not a good proxy for investigating translation controls (Schwanhauser B. *et al.*, 2011), in this study we showed that DHX30 depletion impacts on steady-state levels of nuclear-encoded mitochondrial transcripts. MRPL11 and, particularly, MRPS22 can be considered direct DHX30 targets. Interrogating RNA-seq data in TCGA through the gepia web resource (<http://gepia2.cancer-pku.cn/#index>) the expression of DHX30, MRPL11 and MPR22 appeared to be positively correlated both in normal and cancer samples from several cancer types, including adrenal gland and adrenocortical carcinoma, liver and hepatocellular carcinomas (**Figure 3.20**). No such correlation was instead apparent for breast or colon tissue.

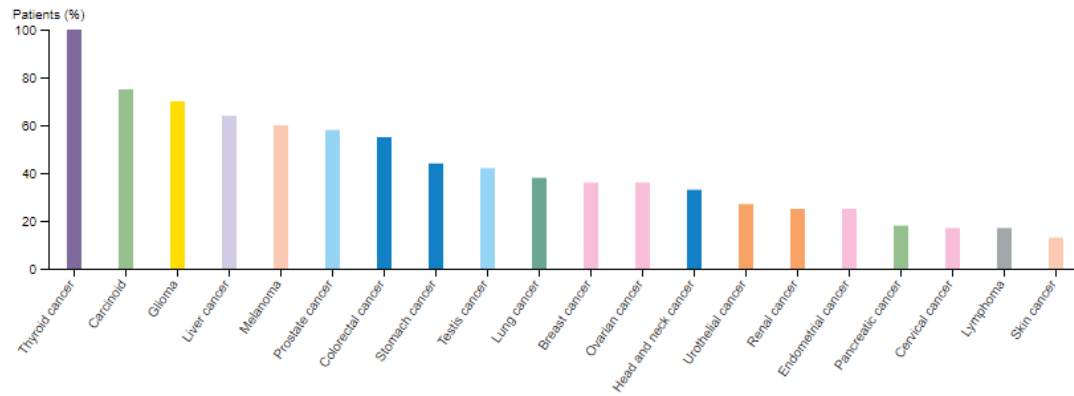


Figure 3.19: DHX30 expression is directly correlated to the percentage of tumor positive patient. Percentage of patients (maximum 12) with high or medium DHX30 expression. Cancer types are color-coded according to which type of normal organ the cancer originates from.

Since I observed that DHX30 could directly interact with mitoribosome transcripts, we next combined the RNA-sequencing polysomal results and, particularly, the Translation Efficiency data (**Figure 3.1**), with the terms most enriched in the GSEA data (**Figure 3.1**, considering the leading-edge genes), with our RIP results and the DHX30 eCLIP data in ENCODE (Van Nostrand EL *et al.*, 2016). This allowed us to compile a list of 14 mitoribosomal protein (MRP) transcripts as candidate direct DHX30 direct targets: MRPL1, MRPL12, MRPL3, MRPL30, MRPL35, MRPL37, MRPL4, MRPL41, MRPL49, MRPL51, MRPS15, MRPS24, MRPS22, MRPL11. Interrogating RNA-seq data in TGCA through the gepia web resource the expression of DHX30, and of each MRP transcript or of the group of 14 candidate target MRPs appeared to be positively correlated in some cancer types, including adrenocortical carcinoma, and hepatocellular carcinomas (**Figure 3.20a**, and **b**; **3.21b**).

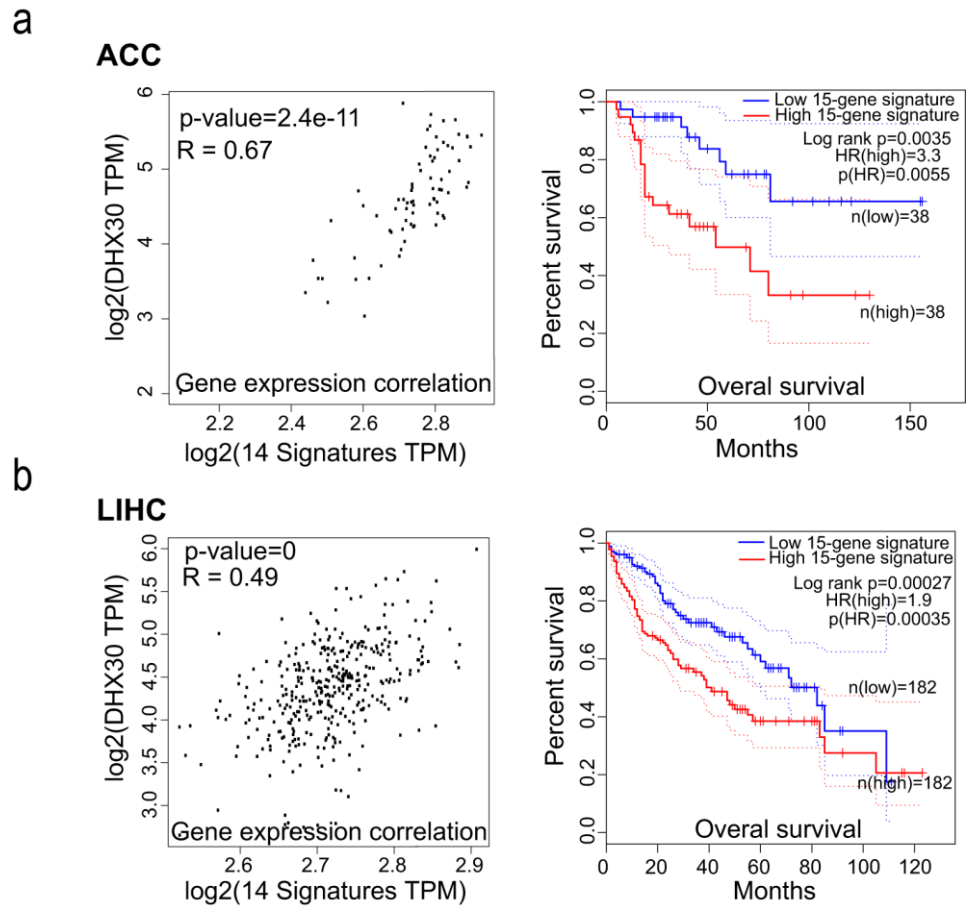


Figure 3.20: Prognostic value of a gene signature comprising DHX30 and its target mitoribosome transcripts. See also Figure 3.20. TCGA data was interrogated through the Gepia web resource to evaluate the correlation between the expression of DHX30 and that of 14 mitoribosomal transcripts that are predicted are direct targets. Presented are two examples among a cluster of eleven cancer types where a positive correlation is apparent. See Figure 3.20 for the complete data and additional examples. **a)** Adrenocortical Carcinomas (ACC). **b)** Liver Hepatocellular Carcinomas (LIHC). Left panels, Pearson correlation; right panels, Overall Survival Kaplan-Meier. The correlation value, the Hazard Ratio, p values and sample sizes are shown.

We next used this gene signature to stratify patients' clinical outcome. Interestingly, for the cancer types where a positive correlation in the expression of DHX30 and the 14 MRPs was observed, the combined 15-gene signature (*i.e.* including DHX30) showed some prognostic value. In particular, higher expression was associated with reduced Overall Survival or Disease-Free Survival (**Figure 3.21**). This preliminary exploration suggests that a functional signature could be developed to predict aggressiveness in cancer types where DHX30 appears to stimulate mito-ribosome gene expression.

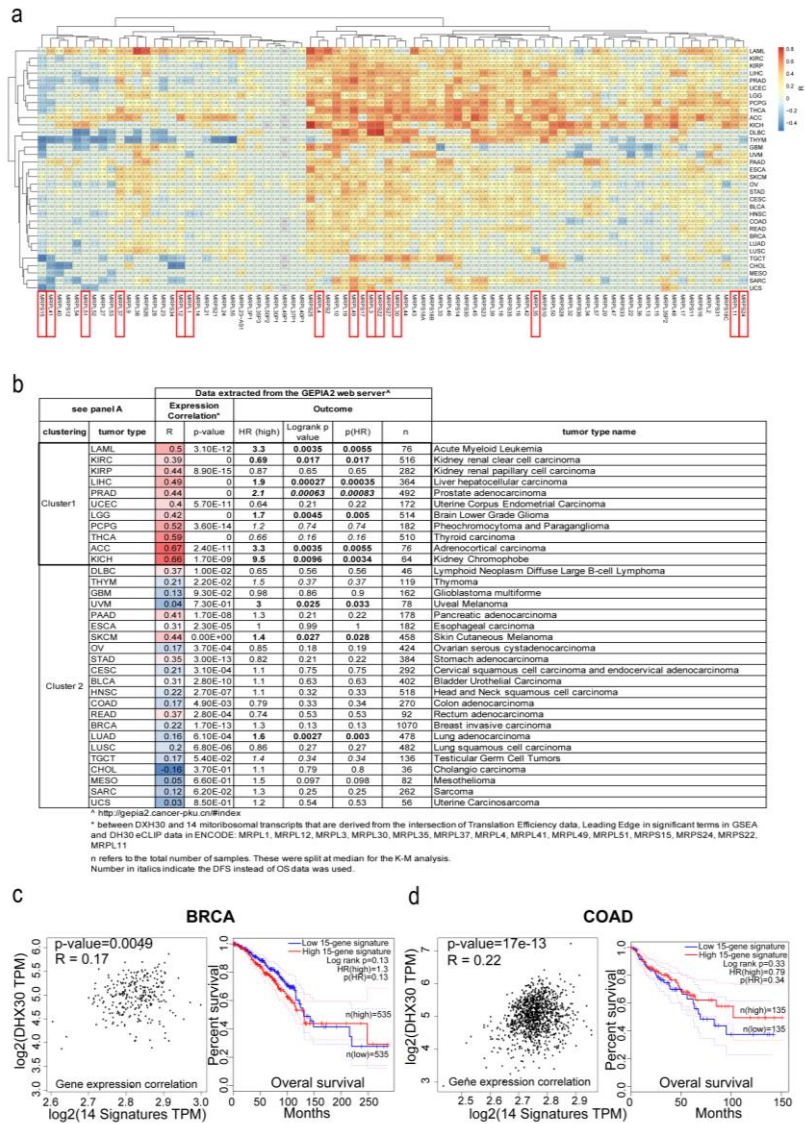


Figure 3.21: DHX30 expression positively correlates with the expression of mitoribosomal protein transcripts and can have prognostic significance.

a) Pearson correlations between the expression of DHX30 and of each mitoribosomal protein transcripts in cancer samples. Data was extracted from the Gepia web server (see methods for details). Unsupervised clustering revealed two major clusters based on the level of gene expression correlation and two main clusters among cancer types. Boxed in red are the names of the fourteen transcripts that are candidate DHX30 direct targets **b)** The expression correlation data (R value and p value) between DHX30 and the combined group of 14 mitoribosomal protein transcripts is listed for each cancer type presented in the same order as for panel A). Data from Kaplan-Meier outcome analysis for the aggregated 15-gene signature (DHX30 + the 14 mitoribosomal protein transcripts). Significant differences are highlighted in bold font. **c), d)** Correlation and Overall Survival Kaplan-Meier curves for two negative examples from cluster 2; colon adenocarcinoma (COAD); breast cancer (BRCA). As for panel b), Hazard Ratio for the high expression group, and p values, and sample size are indicated.

Chapter 4: Discussion and future perspectives

Ribosome biogenesis and translation impose a high metabolic demand on the cell (Buttgereit F. *et al.*, 1995; Wieser W. *et al.*, 2001). Hence, coordination between translational control and metabolic output ultimately involving mitochondrial respiratory functions is expected to contribute to cell homeostasis and fitness (Couvillion MT. *et al.*, 2016; Calamita P. *et al.*, 2018). However, relatively few proteins and pathways have been established to exert a direct role in balancing cytoplasmic translation initiation with mitochondrial metabolism (Morita M. *et al.*, 2017; Pla-Martín D. *et al.*, 2020). eIF6 represents a significant example, as it has been clearly shown that it negatively controls 80S monosome assembly, a necessary step for translation initiation, while at the same time playing a critical positive role in mitochondrial functions, as revealed by broad changes in the mitochondrial proteome in eIF6 hemizygous mice (Clarke K. *et al.*, 2017; Biffo S. *et al.*, 2018). We propose that DHX30 can also exert an important housekeeping role in coordinating ribosome biogenesis, translation, and mitochondrial respiration. Indeed, DHX30 depletion in HCT116, stable or transient, leads to a modest but significant increase in ribosome biogenesis as well as in global translation; on the contrary, mito-ribosome transcripts, particularly of the large subunits, exhibit reduced translation efficiency. Furthermore, DHX30 can also exert a more direct role on mitochondria, as the protein can directly localize to the organelle, thanks to an alternative first exon that features a localization signal. We observed that the depletion of just cytoplasmic DHX30 transcript does not reduce the steady-state expression of mitochondrially encoded genes, but this effect is obtained only when also mitochondrial DHX30 transcript is silenced, resulting in a lower basal mitochondrial respiration, not compensated by glycolysis (Heiden MG *et al.*, 2009). A previous study provided clear evidence that DHX30 can modulate the function of Transcription Elongation Factor Mitochondrial (TEFM), having a role in mitochondrial transcription (Minczuk M. *et al.*, 2011). Furthermore, together with DDX28, FASTKD2, and FASTKD5, it can promote the assembly of 55S mito-monomer and translation (Antonicka H. *et al.*, 2015). Consistent with the relevance of a mitochondrial and translation function, the DHX30 transcript is located and locally translated at the ER-Outer Mitochondrial membrane interface, by APEX-seq (Fazal FM. *et al.*, 2019). In fact, none of the DHX30 closer homologs showed strong evidence of such localized translation or other evidence of mitochondrial localization. Consistently with the enhancement of a high-energy consuming process such as

translation and reduction of energy production via ATP synthase, DHX30 depleted HCT116 cells showed a lower proliferation in 2D and 3D-like model. They also showed higher cell apoptosis proneness upon drug treatments that stabilize p53, such as Nutlin or Doxorubicin, or that cause mitochondrial damage, such as FCCP (**Figure 4.1**).

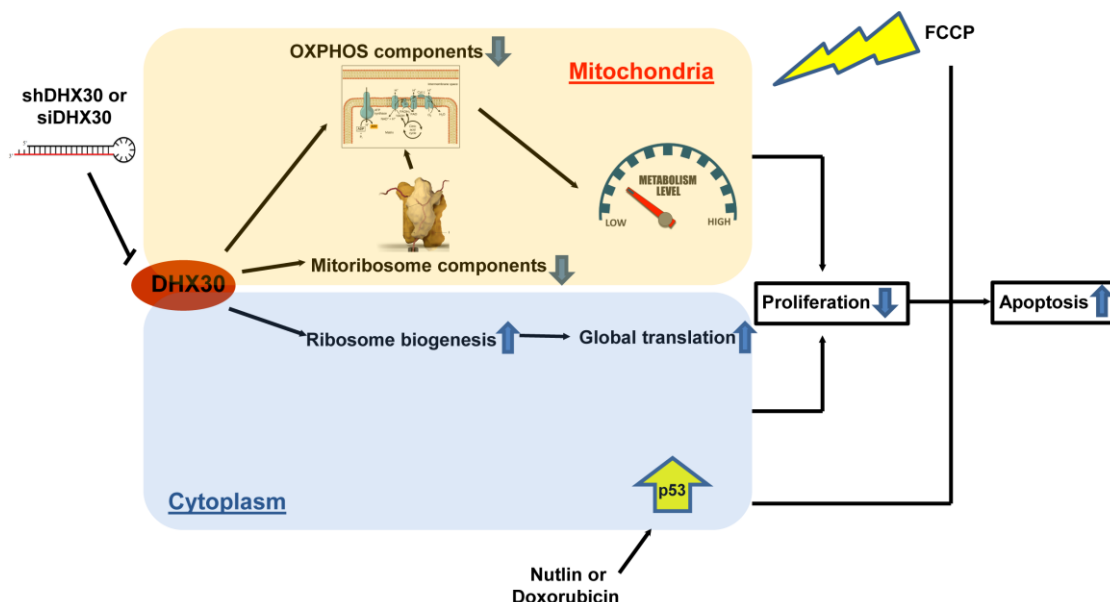


Figure 4.1: Graphical scheme of the DHX30 functions inferred by the results in this thesis. DHX30 depletion by short hairpin or siRNA reduces mitoribosome biogenesis as well as OXPHOS components expression in mitochondria; in contrast it enhances ribosome biogenesis and global translation in the cytoplasm. Those phenomena cause a reduction in proliferation and are associated with higher apoptosis proneness upon p53-activation or the treatment with mitochondrial damaging agents.

The effect on proliferation was visible also by transient silencing of just the cytoplasmic transcript, although it was more evident when the mitochondrial one was also targeted. Although we cannot exclude that the lower proliferation results from a checkpoint activation, as we have seen that in the siRNA experiments the lack of p53 can reduce the proliferation lag, cells did not show evidence for overt cell cycle arrest. This is not entirely unexpected, due to the residual levels of DHX30 expression in the cell models we used, as noted above, and also for the possible selective pressure for compensatory effects given the central nature of the processes involved. Transient silencing of DHX30 in HCT116 p53 null cells besides having a reduced impact on proliferation also did not significantly alter the expression of MRPS22, MRPL11, or mitochondrial transcripts. While this may be suggestive of a functional interaction between DHX30 and p53, results may be affected by the lower efficiency of DHX30 silencing in HCT116 p53^{-/-} cells. Exploring the mitochondrial

role of DHX30 also in breast cancer MCF7 cells I found the same effect observed in HCT116. Indeed, also in this cell line DHX30 silencing reduces expression of nuclear encoding MRPL11 and mitochondrial encoded OXPHOS transcripts. Furthermore, DHX30 depletion causes a lack of cell proliferation. In contrast, the silencing of DHX30 in osteosarcoma U2OS cells does not affect the transcription of MRPL11 nor MRPS22 as well as OXPHOS components. Consistently, in this cell model, DHX30 depletion does not impair cell proliferation. Those findings suggest that DHX30 could act similarly in MCF7 and HCT116, while in U2OS its role may be more dependent on other RNA binding proteins, for example DDX28 in mitochondria. It is also possible that since DHX30 is expressed at relatively higher levels in U2OS, the efficacy or persistence in time of the silencing would be a limiting factor for observed phenotypes.

Those findings suggest that DHX30 could be considered as a potential oncogene by contributing to the coordination between global translation, cell metabolism, and proliferation in cancer. For this reason, it was interesting to explore if the relative expression levels of DHX30 and its putative mito-ribosome targets could be associated with clinical variables in primary cancers.

Although our experiments did not enable us to confirm it in HCT116, a previous report also showed evidence for DHX30 interaction with mitochondrial transcripts in human fibroblasts by RIP-seq (Antonicka H. *et al.*, 2015). Our data instead point to a direct interaction with mitoribosome transcripts and their positive modulation as another means by which DHX30 can indirectly affect the mitochondrial translation. We validated by RIP the binding of DHX30 to MRPL11 and MRPS22. Leveraging public data from eCLIP experiments in ENCODE and our polysomal profiling, RNA-seq, and GSEA analysis, we propose that DHX30 could directly interact with mito-ribosome protein transcripts modulating their expression. Hence, we reasoned that changes in DHX30 levels to an extent that would not lead to overt stress responses could provide opportunities for increased fitness due to the coordination between mitochondrial function and translation potential, which could be considered as a balancing function between energy supply and demand. If any, the effects would be expected to reflect tissue-specific differences in metabolism. We explored TCGA data, first evaluating if a positive correlation could be observed in normal tissue and/or primary cancer samples for DHX30 and mito-ribosome gene expression. Cross-referencing eCLIP data, with our polysomal profiling, RNA-seq,

RIP results, and GSEA data we compiled a list of 14 mito-ribosomal transcripts as candidate direct DHX30 targets. In particular, higher expression is associated with reduced Overall Survival or Disease-Free Survival.

In conclusion, our study demonstrated an oncogenic role of DHX30 that is related to its role in the coordination between global cytoplasmic translation and mitochondrial functions and appears to correlate with tumor aggressiveness.

There are several open ends in this project that require or warrant further investigation. One future perspective would be to elucidate the exact mechanism by which the RNA helicase and RNA binding protein DHX30 exerts its role, in particular, in which way is DHX30 involved in mitochondrially encoded OXPHOS and nuclear encoded mito-ribosome RNA expression. In detail, it could be interesting to study if TEFM is involved in this mechanism as demonstrated by Minczuk M. *et al* also in our cancer cell models, and/or if DHX30 is involved in RNA stability and decay. The direct contribution of DHX30 on global as well as sequence-specific translation could also be explored by purifying the protein and using it in *in vitro* transcription/translation assays. In this context, it would be interesting to compare wild type DHX30 with missense changes recently identified as de novo mutations in patients (Lessel D. *et al.*, 2017), and with a deletion mutant lacking the predicted double-strand RNA binding domain (Chen G. *et al.*, 2020). Although the result could be related to the relative efficiency of silencing, combined with the relatively high level of DHX30 expression, the observation that in U2OS cells DHX30 depletion did not appear to affect mitoribosomal as well as OXPHOS expression, warrants further investigation. Furthermore, preliminary results from our laboratory showed an impact of DHX30 depletion on cell morphology, suggestive of a possible effect on Epithelial-Mesenchymal Transition (EMT) in those cells.

Another important future step could be to investigate deeply the functional crosstalk between p53 and DHX30. Previously, the lab had revealed DHX30 as a modulator of translation efficiency of mRNAs via a target 3'UTR cis-element, influencing p53-dependent apoptosis. Since p53 has a critical tumor-suppressive function in many tissues and is activated by many types of physiological or treatment-dependent stresses, the potential prognostic value of DHX30 expression in cancer that was identified should be re-examined considering p53 status.

Moving this research on primary tissue-derived cells or *in vivo* models using for example xenograft assays should ultimately be considered. On this point, when the DHX30 mechanism will be clear, its protein purification and structure elucidation could open a window on a therapeutic drug strategy against tumors in which it is overexpressed. In particular, knowing the DHX30 structure could be possible to design an array of chemical small molecules able to inhibit the cytoplasmic or mitochondrial protein variant, studying a therapeutic approach for patient cancer treatment.

It was observed that DHX30 has an essential role in mouse development and its homozygous mutation is lethal during embryonic development (Zheng HJ *et al*, 2014). In detail, it is highly expressed in neural cells and somites during embryogenesis and homozygous mutant embryos have neither differentiated somites nor brain, retarding development embryos died at E9.5. A recent study correlates metabolic reprogramming with neural differentiation, showing that neural development causes an enhancement in mitochondrial biogenesis and upregulation of mitochondrial master regulators TFAM and PGC-1 α with an increase in glucose metabolism (Agostini M. *et al*, 2016). Since DHX30 depletion reduces cell energy by impairing OXPHOS gene expression it might be interesting to study this function more in-depth concerning the DHX30 role as a neural differentiating factor.

Finally, in a work by Chen *et al* it was showed that the amino-terminal of DHX30 binds NS1, an Influenza A virus non-structural protein that inhibits host antiviral response. The DHX30:NS1 complex inactivates the function of viral protein NS1, allowing cellular antiviral response upon Influenza A virus infection (Chen G *et al*, 2020). Based on those finding a possible future project could be to explore if the same mechanism is suitable also for other types of RNA virus infection that have NS1, like for example SARS-CoV viruses (Zust R *et al*, 2007). Moreover, several studies selected p53 as an important regulator of immune responses to Influenza A virus infection. In detail, it seems that p53 can lead to an increase in cytokine production and antiviral gene responses such as induction of interferon expression in lung and bone marrow, activating dendritic and CD8⁺T cells, and enhancing antiviral response (Munoz-Fontela C *et al*, 2011; Rivas C *et al*, 2010). Based on those findings, it would be interesting to explore crosstalk between DHX30 and p53 as an antiviral mechanism against dangerous RNA viruses like SARS-CoV or HIV.

References

- Adams PD, Sellers WR, Sharma SK, Wu AD, Nalin CM, Kaelin WG. Identification of a cyclin-cdk2 recognition motif present in substrates and p21-like cyclin-dependent kinase inhibitors. *Mol Cell Biol.* 1996; 16(12):6623-6633. doi:10.1128/mcb.16.12.6623
- Agostini M, Romeo F, Inoue S, et al. Metabolic reprogramming during neuronal differentiation. *Cell Death Differ.* 2016; 23(9):1502-1514. doi:10.1038/cdd.2016.36
- Aktaş T, Ilik IA, Maticzka D, et al. DHX9 suppresses RNA processing defects originating from the Alu invasion of the human genome. *Nature.* 2017; 544(7648):115-119. doi:10.1038/nature21715
- Amaral JD, M. Xavier J, J. Steer C, M.P. Rodrigues C. Targeting the p53 Pathway of Apoptosis. *Curr Pharm Des.* 2010; 16(22):2493-2503. doi:10.2174/138161210791959818
- Amaresh CP, Martindale JL, and Gorospe M. *Bio Protoc.* 2017; 7(3). doi:10.21769/BioProtoc.2126
- Andrysik Z, Galbraith MD, Guarnieri AL, et al. Identification of a core TP53 transcriptional program with highly distributed tumor suppressive activity. *Genome Res.* 2017; 27(10):1645-1657. doi:10.1101/gr.220533.117
- Antonicka H, Shoubbridge EA. Mitochondrial RNA Granules Are Centers for Posttranscriptional RNA Processing and Ribosome Biogenesis. *Cell Rep.* 2015; 10(6):920-932. doi:10.1016/j.celrep.2015.01.030
- Belin S, Hacot S, Daudignon L, et al. Purification of ribosomes from human cell lines. *Curr Protoc Cell Biol.* 2010 ;(SUPPL.49):1-11. doi:10.1002/0471143030.cb0340s49
- Biffo S, Manfrini N, Ricciardi S. Crosstalks between translation and metabolism in cancer. *Curr Opin Genet Dev.* 2018; 48:75-81. doi:10.1016/j.gde.2017.10.011
- Bolger AM, Lohse M, Usadel B. Trimmomatic: A flexible trimmer for Illumina sequence data. *Bioinformatics.* 2014; 30(15):2114-2120. doi:10.1093/bioinformatics/btu170
- Brunet S, Sardon T, Zimmerman T, et al. Characterization of the TPX2 Domains Involved in Microtubule Nucleation and Spindle Assembly in Xenopus nucleation around chromatin and functions in a network of other molecules , some of which also are regulated by. *Mol Biol Cell.* 2004; 15(12):5318-5328. doi:10.1091/mbc.E04

- Budanov AV, Karin M. The p53-regulated Sestrin gene products inhibit mTOR signaling. *October*. 2009; 134(3):451-460. doi:10.1016/j.cell.2008.06.028.The
- Burton-Christie D. *Nature. Blackwell Companion to Christ Spiritual*. 2007; 447(7148):478-495. doi:10.1002/9780470996713.ch28
- Buttgereit F, Brandt MD, Road TC, Cb C. A hierarchy of ATP-consuming. 1995; 167:163-167.
- Butturini E, de Prati AC, Boriero D, Mariotto S. Tumor dormancy and interplay with hypoxic tumor microenvironment. *Int J Mol Sci*. 2019; 20(17). doi:10.3390/ijms20174305
- Cai L, Fritz D and Stefanovic B. Binding of LARP6 to the conserved 5' stem-loop regulates translation of mRNAs encoding type I collagen. *J Mol Biol*. 2010; 395(2): 309–326. doi:10.1016/j.jmb.2009.11.020
- Calamita P, Gatti G, Miluzio A, Scagliola A, Biffo S. Translating the game: Ribosomes as active players. *Front Genet*. 2018; 9(November):1-8. doi:10.3389/fgene.2018.00533
- Chalupníková K, Lattmann S, Selak N, Iwamoto F, Fujiki Y, Nagamine Y. Recruitment of the RNA helicase RHAU to stress granules via a unique RNA-binding domain. *J Biol Chem*. 2008; 283(50):35186-35198. doi:10.1074/jbc.M804857200
- Chang CJ, Chao CH, Xia W, Yang JY, Xiong Y, Li CW, Yu WH, Rehman SK, Hsu JL, Lee HH, Liu M, Chen CT, Yu D, Hung MC. p53 regulates epithelial-mesenchymal transition and stem cell properties through modulating miRNAs. *Nat Cell Biol*. 2011; 13(3): 317-23. Doi: 10.1038/ncb2173
- Chang TC, Wentzel EA, Kent OA, et al. NIH Public Access. 2008; 26(5):745-752.
- Chen G, Ma LC, Wang S, et al. A double-stranded RNA platform is required for the interaction between a host restriction factor and the NS1 protein of influenza A virus. *Nucleic Acids Res*. 2020; 48(1):304-315. doi:10.1093/nar/gkz1094
- Chen MC, Tippiana R, Demeshkina NA, Murat P, Balasubramanian S, Myong S and Ferrè-D'Amarè AR. Structural basis of G-quadruplex unfolding by the DEAH/RHA helicase DHX36. *Nature*. 2018; 558(7710):465–469. doi:10.1038/s41586-018-0209-9
- Cho RW, Clarke MF. Recent advances in cancer stem cells. *Curr Opin Genet Dev*. 2008; 18(1):48-53. doi:10.1016/j.gde.2008.01.017
- Clarke K, Ricciardi S, Pearson T, et al. The Role of Eif6 in Skeletal Muscle Homeostasis Revealed by Endurance Training Co-expression Networks. *Cell Rep*. 2017; 21(6):1507-1520. doi:10.1016/j.celrep.2017.10.040

- Cornella N, Tebaldi T, Gasperini L, et al. The hnRNP RALY regulates transcription and cell proliferation by modulating the expression of specific factors including the proliferation marker E2F1. *J Biol Chem.* 2017; 292(48):19674-19692. doi:10.1074/jbc.M117.795591
- Couvillion MT, Soto IC, Shipkovenska G, Churchman LS. Synchronized mitochondrial and cytosolic translation programs. *Nature.* 2016; 533(7604):499-503. doi:10.1038/nature18015
- Cunningham D, Atkin W, Lenz HJ, et al. Colorectal cancer. *Lancet.* 2010; 375(9719):1030-1047. doi:10.1016/S0140-6736(10)60353-4
- David PL,
- Dejean LM, Martinez-Caballero S, Guo L, Hughes C, Tejjido O, Ducret T, Ichas F, Korsmeyer SJ, Antonsson B, Jonas EA, and Kinnally KW. Oligomeric Bax Is a Component of the Putative Cytochrome c Release Channel MAC, Mitochondrial Apoptosis-induced Channel. *Mol Bio Cel.* 2005; 16(5): 2424-2432. doi: 10.1091/mbc.E04-12-1111
- DeLeo AB, Jay G, Appella E, Dubois GC, Law LW, Old LJ. Detection of a transformation-related antigen in chemically induced sarcomas and other transformed cells of the mouse. *Proc Natl Acad Sci U S A.* 1979; 76(5):2420-2424. doi:10.1073/pnas.76.5.2420
- DeNardo DG, Andreu P, Coussens LM. Interactions between lymphocytes and myeloid cells regulate pro-versus anti-tumor immunity. *Cancer Metastasis Rev.* 2010; 29(2):309-316. doi:10.1007/s10555-010-9223-6
- Deng G, Sui G. Noncoding RNA in oncogenesis: A new era of identifying key players. *Int J Mol Sci.* 2013; 14(9):18319-18349. doi:10.3390/ijms140918319
- Edinger AL, Thompson CB. Death by design: Apoptosis, necrosis and autophagy. *Curr Opin Cell Biol.* 2004; 16(6):663-669. doi:10.1016/j.ceb.2004.09.011
- El-Deiry WS. Regulation of p53 downstream genes. *Semin Cancer Biol.* 1998; 8(5):345-357. doi:10.1006/scbi.1998.0097
- Fazal FM, Han S, Parker KR, et al. Atlas of Subcellular RNA Localization Revealed by APEX-Seq. *Cell.* 2019; 178(2):473-490.e26. doi:10.1016/j.cell.2019.05.027
- Ferlay J, Soerjomataram I, Dikshit R, et al. Cancer incidence and mortality worldwide: Sources, methods and major patterns in GLOBOCAN 2012. *Int J Cancer.* 2015; 136(5):E359-E386. doi:10.1002/ijc.29210
- Fontoura BM, Sorokina EA, David E, Carroll RB. p53 is covalently linked to 5.8S rRNA. *Mol Cell Biol.* 1992; 12(11):5145-5151. doi:10.1128/mcb.12.11.5145

- Freed-Pastor WA, Prives C. Mutant p53: One name, many proteins. *Genes Dev.* 2012; 26(12):1268-1286. doi:10.1101/gad.190678.112
- Ge J, Karijolich J, Zhai Y, Zheng J and Yu YT. 5-Fluorouracil Treatment Alters the Efficiency of Translational Recoding. *Genes.* 2017; 8(11): 295-307. doi:10.3390/genes8110295
- George P, George P. P53 HOW CRUCIAL IS ITS ROLE IN CANCER? DR. PHILOMENA GEORGE International Journal of Current Pharmaceutical Research 2014; 3(2).
- Grover R, Candeias MM, Fhraeus R, Das S. P53 and little brother p53/47: Linking IRES activities with protein functions. *Oncogene.* 2009; 28(30):2766-2772. doi:10.1038/onc.2009.138
- Guicciardi ME, Gores GJ. Life and death by death receptors. *FASEB J.* 2009; 23(6):1625-1637. doi:10.1096/fj.08-111005
- Hanahan D, Weinberg RA. Hallmarks of cancer: The next generation. *Cell.* 2011; 144(5):646-674. doi:10.1016/j.cell.2011.02.013
- Hao Q, Cho WC. Battle against cancer: An everlasting saga of p53. *Int J Mol Sci.* 2014; 15(12):22109-22127. doi:10.3390/ijms151222109
- Harris SL, Levine AJ. The p53 pathway: Positive and negative feedback loops. *Oncogene.* 2005; 24(17):2899-2908. doi:10.1038/sj.onc.1208615
- He L, He X, Lim LP, de Stanchina E, Xuan Z, Liang Y, Xue W, Zender L, Magnus J, Ridzone D, Jackson AL, Linsley PS, Chen C, Lowe SW, Cleary MA, Hannon GJ. A microRNA component of the p53 tumour suppressor network. *Nature.* 2007; 447(7148):1130-4. Doi: 10.1038/nature05939
- Heiden MG, Cantley LC, Thompson CB. Understanding the Warburg effect: the metabolic requirements of cell proliferation. *Science.* 2009; 324(5930):1029-33. Doi: 10.1126/science.1160809
- Hermeking H, Lengauer C, Polyak K, He TC, Zhang L, Thiagalingam S, Kinzel KW, Vogelstein B. 14-3-3sigma is a p53-regulated inhibitor of G2/M progression. *Mol Cell.* 1997; 1(1):3-11. doi: 10.1016/s1097-2765(00)80002-7
- Hermeking H. MicroRNAs in the p53 network: Micromanagement of tumour suppression. *Nat Rev Cancer.* 2012; 12(9):613-626. doi:10.1038/nrc3318
- Horton LE, Bushell M, Barth-Baus D, Tilleray VJ, Clemens MJ, Hensold JO. p53 activation results in rapid dephosphorylation of the eIF4E-binding protein 4E-BP1, inhibition of ribosomal protein S6 kinase and inhibition of translation initiation. *Oncogene.* 2002; 21(34):5325-5334. doi:10.1038/sj.onc.1205662

- https://ec.europa.eu/eurostat/statisticsexplained/index.php?title=Cancer_statistics#Deaths_from_cancer
- <https://gco.iarc.fr/>
- <http://gepia2.cancer-pku.cn/#index>
- <https://gco.iarc.fr/today/online-analysis>
- <http://www.gencodegenes.org/releases/>
- <https://www.proteinatlas.org/>
- Huun J, Gansmo LB, Mannsåker B, et al. The Functional Roles of the MDM2 Splice Variants P2-MDM2-10 and MDM2-Δ5 in Breast Cancer Cells. *Transl Oncol.* 2017; 10(5):806-817. doi:10.1016/j.tranon.2017.07.006
- Jeffrey PD, Gorina S, Pavletich NP. Crystal structure of the tetramerization domain of the p53 tumor suppressor at 1.7 angstroms. *Science*, 1995; 267:1498-1502. DOI: 10.1126/science.7878469
- Jenner L, Melnikov S, de Loubresse NG, et al. Crystal structure of the 80S yeast ribosome. *Curr Opin Struct Biol.* 2012; 22(6):759-767. doi:10.1016/j.sbi.2012.07.013
- Jewad N, Direkze N, Leedham SJ. Inflammatory bowel disease and colon cancer. *Recent Results in Cancer Research*, 2011; 185:99-115. DOI: 10.1007/978-3-642-03503-6_6.
- Jin J, Jing W, Lei XX, et al. Evidence that Lin28 stimulates translation by recruiting RNA helicase A to polysomes. *Nucleic Acids Res.* 2011; 39(9):3724-3734. doi:10.1093/nar/gkq1350
- Koh WS, Porter JR, Batchelor E. Tuning of mRNA stability through altering 3'-UTR sequences generates distinct output expression in a synthetic circuit driven by p53 oscillations. *Sci Rep.* 2019; 9(1):1-8. doi:10.1038/s41598-019-42509-y
- Kong YW, Ferland-McCollough D, Jackson TJ, Bushell M. MicroRNAs in cancer management. *Lancet Oncol.* 2012; 13(6):e249-e258. doi:10.1016/S1470-2045(12)70073-6
- Lane DP, Crawford L V. T antigen is bound to a host protein in SY40-transformed cells. *Nature.* 1979; 278(5701):261-263. doi:10.1038/278261a0
- Le MTN, Teh C, Shyh-Chang N, et al. Supplementary Figure 1 A -MicroRNA-125b is a novel negative regulator of p53. *Genes Dev.* 2009; (3):1-9. doi:10.1101/gad.1767609.stability
- Lee T, Pelletier J. The biology of DHX9 and its potential as a therapeutic target INTRODUCTION TO DHX9 AND DEXD/ H-BOX HELICASES. *Oncotarget.* 2016; 7(27):42716-42739

- Lee T, Di Paola D, Malina A, et al. Suppression of the DHX9 helicase induces premature senescence in human diploid fibroblasts in a p53-dependent manner. *J Biol Chem.* 2014; 289(33):22798-22814. doi:10.1074/jbc.M114.568535
- Lessel D, Schob C, Küry S, et al. De Novo Missense Mutations in DHX30 Impair Global Translation and Cause a Neurodevelopmental Disorder. *Am J Hum Genet.* 2017; 101(5):716-724. doi:10.1016/j.ajhg.2017.09.014
- Levine AJ, Oren M. The first 30 year of p53: growing ever more complex. *Nat Rev Cancer.* 2009; 9(10):749-758. doi:10.1038/nrc2723
- Liang SH, Clarke MF. The nuclear import of p53 is determined by the presence of a basic domain and its relative position to the nuclear localization signal. *Oncogene.* 1999; 18(12):2163-2166. doi:10.1038/sj.onc.1202350
- Linder P, Lasko PF, Ashburner M, et al. Birth of the D-E-A-D box [5]. *Nature.* 1989; 337(6203):121-122. doi:10.1038/337121a0
- Linzer DIH, Levine a. J. Characterization Tumor Antigen and Uninfected of a 54K Dalton Cellular SV40 Present in SV40-Transformed Cells. *Cell.* 1979; 17(1):43-52. doi:10.1016/0092-8674(79)90293-9
- Lunde BM, Moore C, Varani G. RNA-binding proteins: Modular design for efficient function. *Nat Rev Mol Cell Biol.* 2007; 8(6):479-490. doi:10.1038/nrm2178
- Marcel V, Catez F, Diaz JJ. P53, a translational regulator: Contribution to its tumour-suppressor activity. *Oncogene.* 2015; 34(44):5513-5523. doi:10.1038/onc.2015.25
- Mauro VP, Matsuda D. Translation regulation by ribosomes: Increased complexity and expanded scope. *RNA Biol.* 2016; 13(9):748-755. doi:10.1080/15476286.2015.1107701
- Millau JF, Bastien N, Drouin R. P53 transcriptional activities: A general overview and some thoughts. *Mutat Res - Rev Mutat Res.* 2009; 681(2-3):118-133. doi:10.1016/j.mrrev.2008.06.002
- Minczuk M, He J, Duch AM, et al. TEFM (c17orf42) is necessary for transcription of human mtDNA. *Nucleic Acids Res.* 2011; 39(10):4284-4299. doi:10.1093/nar/gkq1224
- Mollet S, Cougot N, Wilczynska A, Dautry F, Kress M, Bertrand E, and Weil D. Translationally Repressed mRNA Transiently Cycles through Stress Granules during Stress. *Mol Biol Cell.* 2008; 19(10): 4469-4479. Doi: 10.1091/mbc.E08-05-0499
- Momand J, Zambetti GP, Olson DC, George D, Levine AJ. The mdm-2 oncogene product forms a complex with the p53 protein and inhibits p53-mediated transactivation. *Cell.* 1992; 69(7):1237-1245. doi:10.1016/0092-8674(92)90644-R

- Morita M, Prudent J, Basu K, et al. mTOR Controls Mitochondrial Dynamics and Cell Survival via MTFP1. *Mol Cell*. 2017; 67(6):922-935.e5. doi:10.1016/j.molcel.2017.08.013
- Müller-Mcnicoll M, Neugebauer KM. How cells get the message: Dynamic assembly and function of mRNA-protein complexes. *Nat Rev Genet*. 2013; 14(4):275-287. doi:10.1038/nrg3434
- Muñoz-Fontela C, Pazos M, Delgado I, et al. p53 Serves as a Host Antiviral Factor That Enhances Innate and Adaptive Immune Responses to Influenza A Virus. *J Immunol*. 2011; 187(12):6428-6436. doi:10.4049/jimmunol.1101459
- Niemantsverdriet M, Jongmans W, Backendorf C. Radiation response and cell cycle regulation of p53 rescued malignant keratinocytes. *Exp Cell Res*. 2005; 310(1):237-247. doi:10.1016/j.yexcr.2005.07.016
- Nissanka N, Moraes CT. Mitochondrial DNA damage and reactive oxygen species in neurodegenerative disease. *FEBS Lett*. 2018; 592(5):728-742. doi:10.1002/1873-3468.12956
- Nurse P. A long twentieth century of the cell cycle and beyond. *Cell*. 2000; 100(1):71-78. doi:10.1016/S0092-8674(00)81684-0
- Petersson J, Ageberg M, Sandén C, Olofsson T, Gullberg U, Drott K. The p53 target gene TRIM22 directly or indirectly interacts with the translation initiation factor eIF4E and inhibits the binding of eIF4E to eIF4G. *Biol Cell*. 2012; 104(8):462-475. doi:10.1111/boc.201100099
- Pla-Martín D, Schatton D, Wiederstein JL, et al. CLUH granules coordinate translation of mitochondrial proteins with mTORC1 signaling and mitophagy. *EMBO J*. 2020; 39(9):1-23. doi:10.15252/embj.2019102731
- Provenzani A, Fronza R, Loreni F, Pascale A, Amadio M, Quattrone A. Global alterations in mRNA polysomal recruitment in a cell model of colorectal cancer progression to metastasis. *Carcinogenesis*. 2006; 27(7):1323-1333. doi:10.1093/carcin/bgi377
- Raver-Shapira N, Marciano E, Meiri E, et al. Transcriptional Activation of miR-34a Contributes to p53-Mediated Apoptosis. *Mol Cell*. 2007; 26(5):731-743. doi:10.1016/j.molcel.2007.05.017
- Ryan KM. P53 and autophagy in cancer: Guardian of the genome meets guardian of the proteome. *Eur J Cancer*. 2011; 47(1):44-50. doi:10.1016/j.ejca.2010.10.020
- Riley KJL and Maher LJ. Analysis of p53-RNA Interactions in Cultured Human Cells. *Biochem Biophys Res Commun*. 2007; 363(2): 381–387. doi: 10.1016/j.

- Rivas C, Aaronson SA, Munoz-Fontela C. Dual role of p53 in innate antiviral immunity. *Viruses*. 2010; 2(1):298-313. doi:10.3390/v2010298
- Rizzotto D, Zaccara S, Rossi A, et al. Nutlin-Induced Apoptosis Is Specified by a Translation Program Regulated by PCBP2 and DHX30. *Cell Rep*. 2020; 30(13):4355-4369.e6. doi:10.1016/j.celrep.2020.03.011 bbrc.2007.08.181
- Robinson MD, McCarthy DJ, Smyth GK. EdgeR: A Bioconductor package for differential expression analysis of digital gene expression data. *Bioinformatics*. 2009; 26(1):139-140. doi:10.1093/bioinformatics/btp616
- Schwanhüusser B, Busse D, Li N, et al. Global quantification of mammalian gene expression control. *Nature*. 2011; 473(7347):337-342. doi:10.1038/nature10098
- Scoumanne A, Cho SJ, Zhang J, Chen X. The cyclin-dependent kinase inhibitor p21 is regulated by RNA-binding protein PCBP4 via mRNA stability. *Nucleic Acids Res*. 2011; 39(1):213-224. doi:10.1093/nar/gkq778
- Sergushichev AA, Loboda AA, Jha AK, et al. GAM: a web-service for integrated transcriptional and metabolic network analysis. *Nucleic Acids Res*. 2016; 44(W1):W194-W200. doi:10.1093/nar/gkw266
- Silvera D, Formenti SC, Schneider RJ. Translational control in cancer. *Nat Rev Cancer*. 2010; 10(4):254-266. doi:10.1038/nrc2824
- Simeonova I, Jaber S, Draskovic I, et al. Mutant Mice Lacking the p53 C-Terminal Domain Model Telomere Syndromes. *Cell Rep*. 2013; 3(6):2046-2058. doi:10.1016/j.celrep.2013.05.028
- Singh A, Settleman J. EMT cancer stem cells and drug resistance. *Oncogene*. 2010; 29(34):4741-4751. doi:10.1038/onc.2010.215.EMT
- Sinha AU, Kaimal V, Chen J, Jegga AG. Dissecting microregulation of a master regulatory network. *BMC Genomics*. 2008; 9:1-19. doi:10.1186/1471-2164-9-88
- Smits VAJ, Klompmaker R, Vallenius T, Rijksen G, Mäkelä TP, Medema RH. p21 Inhibits Thr161 phosphorylation of Cdc2 to enforce the G2 DNA damage checkpoint. *J Biol Chem*. 2000; 275(39):30638-30643. doi:10.1074/jbc.M005437200
- Sonenberg N, Hinnebusch AG. Regulation of translation initiation in eukaryotes. *Cell*. 2009; 136(4):731-745. doi:10.1016/j.cell.2009.01.042.Regulation
- Sophie Moka JRM, Cristina Garreau M-J, Fournier 'e, et al. Uncoupling Stress Granule Assembly and Translation Initiation Inhibition. *Mol Biol Cell*. 2009; 20(October):2673-2683. doi:10.1091/mbc.E08

- Srivastava A, Sarkar H, Gupta N, Patro R. RapMap: A rapid, sensitive and accurate tool for mapping RNA-seq reads to transcriptomes. *Bioinformatics*. 2016; 32(12):i192-i200. doi:10.1093/bioinformatics/btw277
- Stommel JM. A leucine-rich nuclear export signal in the p53 tetramerization domain: regulation of subcellular localization and p53 activity by NES masking. *EMBO J*. 1999; 18(6):1660-1672. doi:10.1093/emboj/18.6.1660
- Stucchi G, Battevi N, Cairoli S, Consonni D. The prevalence of musculoskeletal disorders in the retail sector: an Italian cross sectional study on 3380 workers. *Med Lav*. 2016; 107(4):251-262.
- Subramanian M, Jones MF, Lal A. Long non-coding RNAs embedded in the Rb and p53 pathways. *Cancers (Basel)*. 2013; 5(4):1655-1675. doi:10.3390/cancers5041655
- Sur S, Pagliarini R, Bunz F, et al. A panel of isogenic human cancer cells suggests a therapeutic approach for cancers with inactivated p53. *Proc Natl Acad Sci U S A*. 2009; 106(10):3964-3969. doi:10.1073/pnas.0813333106
- Suzuki HI, Yamagata K, Sugimoto K, Iwamoto T, Kato S, Miyazono K. Modulation of microRNA processing by p53. *Nature*. 2009; 460(7254):529-533. doi:10.1038/nature08199
- Taanman JW. The mitochondrial genome: Structure, transcription, translation and replication. *Biochim Biophys Acta - Bioenerg*. 1999; 1410(2):103-123. doi:10.1016/S0005-2728(98)00161-3
- Tang Z, Kang B, Li C, Chen T, Zhang Z. GEPIA2: an enhanced web server for large-scale expression profiling and interactive analysis. *Nucleic Acids Res*. 2019; 47(W1):W556-W560. doi:10.1093/nar/gkz430
- Tanner NK, Cordin O, Banroques J, Doère M, Linder P. The Q motif: A newly identified motif in DEAD box helicases may regulate ATP binding and hydrolysis. *Mol Cell*. 2003; 11(1):127-138. doi:10.1016/S1097-2765(03)00006-6
- Tippana R, Chen MC, Demeshkina NA, Ferré-D'Amaré AR, Myong S. RNA G-quadruplex is resolved by repetitive and ATP-dependent mechanism of DHX36. *Nat Commun*. 2019; 10(1):1-10. doi:10.1038/s41467-019-09802-w
- Toledo F, Krummel KA, Lee CJ, et al. A mouse p53 mutant lacking the proline-rich domain rescues Mdm4 deficiency and provides insight into the Mdm2-Mdm4-p53 regulatory network. *Cancer Cell*. 2006; 9(4):273-285. doi:10.1016/j.ccr.2006.03.014
- Tovar C, Rosinski J, Filipovic Z, et al. Small-molecule MDM2 antagonists reveal aberrant p53 signaling in cancer: Implications for therapy. *Proc Natl Acad Sci U S A*. 2006; 103(6):1888-1893. doi:10.1073/pnas.0507493103

- Van Nostrand EL Van, Pratt G a, Shishkin A a, et al. eCLIP. 2016; 13(6):508-514. doi:10.1038/nmeth.3810.Robust
- Vander Heiden M, Cantley L, Thompson C. The Metabolic Requirements of Cell Proliferation. *Science*. 2009; 324(5930):1029-1033. doi:10.1126/science.1160809.Understanding
- Veprintsev DB, Freund SMV, Andreeva A, et al. Core domain interactions in full-length p53 in solution. *Proc Natl Acad Sci U S A*. 2006; 103(7):2115-2119. doi:10.1073/pnas.0511130103
- Viero G, Lunelli L, Passerini A, et al. Three distinct ribosome assemblies modulated by translation are the building blocks of polysomes. *J Cell Biol*. 2015; 208(5):581-596. doi:10.1083/jcb.201406040
- Wang Y, Bogenhagen DF. Human mitochondrial DNA nucleoids are linked to protein folding machinery and metabolic enzymes at the mitochondrial inner membrane. *J Biol Chem*. 2006; 281(35):25791-25802. doi:10.1074/jbc.M604501200
- Watson AJM, Collins PD. Colon Cancer: A civilization disorder, *Dig Dis*, 2011; 29, 222-228. DOI: 10.1159/000323926.
- Wieser W, Krumschnabel G. Hierarchies of ATP-consuming processes: Direct compared with indirect measurements, and comparative aspects. *Biochem J*. 2001; 355(2):389-395. doi:10.1042/0264-6021:3550389
- Wurth L. Versatility of RNA-binding proteins in cancer. *Comp Funct Genomics*. 2012. doi:10.1155/2012/178525
- www.cancer.gov
- Xue W, Zender L, Miething C, et al. Senescence and tumour clearance is triggered by p53 restoration in murine liver carcinomas. *Nature*. 2015; 445(7128):656-660. doi:10.1038/nature05529
- Xue S and Barna M. Specialized ribosomes: a new frontier in gene regulation and organismal biology. *Nat Rev Mol Cell Biol*. 2012; 13(6):355–369. doi:10.1038/nrm3359
- Yang G, Sau C, Lai W, Cichon J, Li W. p53 regulates epithelial-mesenchymal transition (EMT) and stem cell properties through modulating miRNAs. 2015; 344(6188):1173-1178. doi:10.1126/science.1249098.Sleep
- Ye P, Liu S, Zhu Y, Chen G, Gao G. DEXH-Box protein DHX30 is required for optimal function of the zinc-finger antiviral protein. *Protein Cell*. 2010; 1(10):956-964. doi:10.1007/s13238-010-0117-8

- Yip KW, Reed JC. Bcl-2 family proteins and cancer. *Oncogene*. 2008; 27(50):6398-6406. doi:10.1038/onc.2008.307
- Yoon A, Peng G, Brandenburg Y, et al. Impaired control of IRES-mediated translation in X-linked dyskeratosis congenita. *Science*. 2006; 312(5775):902-906. doi:10.1126/science.1123835
- Yoon JH, Abdelmohsen K, Srikantan S, et al. LincRNA-p21 Suppresses Target mRNA Translation. *Mol Cell*. 2012; 47(4):648-655. doi:10.1016/j.molcel.2012.06.027
- Zaccara S, Tebaldi T, Pederiva C, Ciribilli Y, Bisio A, Inga A. P53-directed translational control can shape and expand the universe of p53 target genes. *Cell Death Differ*. 2014; 21(10):1522-1534. doi:10.1038/cdd.2014.79
- Zhan Q, Antinore MJ, Wang XW, et al. Association with Cdc2 and inhibition of Cdc2/Cyclin B1 kinase activity by the p53-regulated protein Gadd45. *Oncogene*. 1999; 18(18):2892-2900. doi:10.1038/sj.onc.1202667
- Zhang J, Cho SJ, Shu L, et al. Translational repression of p53 by RNPC1, a p53 target over expressed in lymphomas. *Genes Dev*. 2011; 25(14):1528-1543. doi:10.1101/gad.2069311
- Zheng HJ, Tsukahara M, Liu E, et al. The novel helicase helG (DHX30) is expressed during gastrulation in mice and has a structure similar to a human DExH box helicase. *Stem Cells Dev*. 2015; 24(3):372-383. doi:10.1089/scd.2014.0077
- Zhu N, Gu L, Findley HW, Zhou M. Transcriptional repression of the eukaryotic initiation factor 4E gene by wild type p53. *Biochem Biophys Res Commun*. 2005; 335(4):1272-1279. doi:10.1016/j.bbrc.2005.08.026
- Züst R, Cervantes-Barragán L, Kuri T, et al. Coronavirus non-structural protein 1 is a major pathogenicity factor: Implications for the rational design of coronavirus vaccines. *PLoS Pathog*. 2007; 3(8):1062-1072. doi:10.1371/journal.ppat.0030109

APPENDIX

SLMP53-2 Restores Wild-Type-like Function to Mutant p53 through Hsp70: Promising Activity in Hepatocellular Carcinoma

*Gomes S, **Bosco B**, Loureiro JB, Ramos H, Raimundo L, Soares J, Nazareth N, Barcherini V, Domingues L, Oliveira C, Bisio A, Piazza S, Bauer MR, Brás JP, Almeida MI, Gomes C, Reis F, Fersht AR, Inga A, Santos MMM, Saraiva L*

Cancers 2019, 8: 1151-1171, doi:10.3390/cancers11081151

This work was developed in collaboration with the Drug Discovery and Development Research Unit at the University of Porto, led by prof. Lucilia Saraiva. We analyzed a newly synthesized molecule called SLMP53-2 investigating its effect in mutant p53 reactivation. In detail, SLMP53-2 was tested on mutp53-Y220C-expressing hepatocellular carcinoma (HCC) cells, and it was shown that it induced cell cycle arrest, apoptosis, and endoplasmic reticulum stress responses. SLMP53-2 was also shown to be able to restore wild-type-like conformation and DNA-binding ability to mutp53-Y220C likely through the heat shock protein 70 (Hsp70), thus reestablishing p53 transcriptional activity. Interestingly, SLMP53-2 showed potent antitumor activity not only in human HCC cell cultures but also in human HCC xenograft mouse model with no apparent toxic side effects.



In this work, my specific contribution was related to the transcriptomic analysis of the impact of SLMP53-2 treatment by a microarray experiment on mutp53-Y220C HuH-7 hepatocellular carcinoma cells treated with two different concentrations (2x IC₅₀ and 3x IC₅₀) SLMP53-2. As a control, I also measured the effect of 10uM Nutlin treatment alone or combined with SLMP53-2. As expected, Nutlin alone did not induce significant gene expression changes in this cell line. Furthermore, I did not see a strong interaction between Nutlin and SLMP53-2. The experiment was performed in biological triplicate and the array data were processed in-house by Dr. Silvano Piazza of the CIBIO Bioinformatics facility and I was then involved in the validation of the transcriptome data, GSEA pathway, and Gene Ontology analyses, employing also an HuH-p53 null derivative clone.

Briefly, I found that endoplasmic reticulum stress response is caused by SLMP53-2 treatment and validated it by qRT-PCR of various targets and by XBP1 splice variant relative quantification and protein localization by immunofluorescence. Based on the unfolded protein response observed, we hypothesized involvement of heat shock proteins in the mutant p53 re-folding process and started to validate this hypothesis by co-immunoprecipitation, an experiment that was then confirmed for HSP70 in the Saraiva lab. The impact of SLMP53-2 was shown to be mutant p53 dependent using a p53-null derivative clone.

This work is potentially linkable to my main Ph.D. project since the results revealed that SLMP53-2 treatment can lead to cell cycle arrest and apoptosis dependent on p53 and also to Unfolded Protein Response (UPR) activation. We know that the silencing of mitochondrial DHX30 caused mitochondrial stress and energy impairment. Moreover, DHX30 silencing enhances translation and the combination of these two features may lead to an unfolded protein response, like SLMP53-2 treatment. Indeed, it will be interesting to study if targeting DHX30 could have an additive or even synergistic effect combined with SLMP53-2 treatment, leading to massive apoptosis.

Article

SLMP53-2 Restores Wild-Type-Like Function to Mutant p53 through Hsp70: Promising Activity in Hepatocellular Carcinoma

Sara Gomes ¹, Bartolomeo Bosco ², Joana B. Loureiro ¹, Helena Ramos ¹, Liliana Raimundo ¹, Joana Soares ¹, Nair Nazareth ¹, Valentina Barcherini ³, Lucília Domingues ⁴, Carla Oliveira ⁴, Alessandra Bisio ², Silvano Piazza ², Matthias R. Bauer ⁵, João P. Brás ^{6,7}, Maria Inês Almeida ^{6,7}, Célia Gomes ⁸, Flávio Reis ⁸, Alan R. Fersht ⁵, Alberto Inga ², Maria M. M. Santos ^{3,*}  and Lucília Saraiva ^{1,*} 

¹ LAQV/REQUIMTE, Department of Biological Sciences, Laboratory of Microbiology, Faculty of Pharmacy, University of Porto, Rua de Jorge Viterbo Ferreira 228, 4050-313 Porto, Portugal

² Department of Cellular, Computational and Integrative Biology (CIBIO), University of Trento, Via Sommarive 9, 38123 Trento, Italy

³ Research Institute for Medicines (iMed.Ulisboa), Faculty of Pharmacy, University of Lisbon, Av. Prof. Gama Pinto, 1649-003 Lisboa, Portugal

⁴ CEB—Centre of Biological Engineering, University of Minho, Campus de Gualtar, 4710-057 Braga, Portugal

⁵ Medical Research Council, Laboratory of Molecular Biology, Francis Crick Avenue, Cambridge CB2 0QH, UK

⁶ i3S—Institute for Research and Innovation in Health, University of Porto, Rua Alfredo Allen 208, 4200-135 Porto, Portugal

⁷ INEB—Institute of Biomedical Engineering, University of Porto, Rua Alfredo Allen 208, 4200-135 Porto, Portugal

⁸ Institute of Pharmacology & Experimental Therapeutics, Coimbra Institute for Clinical and Biomedical Research (iCIBR), Faculty of Medicine, CNC.IBILI Consortium & CIBB Consortium, University of Coimbra, 3000-548 Coimbra, Portugal

* Correspondence: mariasantos@ff.ulisboa.pt (M.M.M.S.); lucilia.saraiva@ff.up.pt (L.S.);

Tel.: +351-21-794-6451 (M.M.M.S.); +351-22-042-8500 (L.S.)

Received: 4 June 2019; Accepted: 7 August 2019; Published: 10 August 2019

check
for



update
s

Abstract: Half of human cancers harbor *TP53* mutations that render p53 inactive as a tumor suppressor. In these cancers, reactivation of mutant p53 (mutp53) through restoration of wild-type-like function constitutes a valuable anticancer therapeutic strategy. In order to search for mutp53 reactivators, a small library of tryptophanol-derived oxazoloisindolinones was synthesized and the potential of these compounds as mutp53 reactivators and anticancer agents was investigated in human tumor cells and xenograft mouse models. By analysis of their anti-proliferative effect on a panel of p53-null NCI-H1299 tumor cells ectopically expressing highly prevalent mutp53, the compound SLMP53-2 was selected based on its potential reactivation of multiple structural mutp53. In mutp53-Y220C-expressing hepatocellular carcinoma (HCC) cells, SLMP53-2-induced growth inhibition was mediated by cell cycle arrest, apoptosis, and endoplasmic reticulum stress response. In these cells, SLMP53-2 restored wild-type-like conformation and DNA-binding ability of mutp53-Y220C by enhancing its interaction with the heat shock protein 70 (Hsp70), leading to the reestablishment of p53 transcriptional activity. Additionally, SLMP53-2 displayed synergistic effect with sorafenib, the only approved therapy for advanced HCC. Notably, it exhibited potent antitumor activity in human HCC xenograft mouse models with a favorable toxicological profile. Collectively, SLMP53-2 is a new mutp53-targeting agent with promising antitumor activity, particularly against HCC.

Keywords: anticancer therapeutics; hepatocellular carcinoma; Hsp70; mutant p53; tryptophanol-derived oxazoloisindolinone

1. Introduction

As the most frequently inactivated tumor suppressor in human tumors, p53 has attracted great interest as an anticancer therapeutic target. p53 is a transcription factor that regulates several cellular processes, including apoptosis, cell cycle, and DNA-damage repair [1]. Over half of human tumors harbor *TP53* mutations, leading not only to the impairment of p53 tumor-suppressive activity, but also to gain-of-function that promotes tumor growth, dissemination, and chemoresistance [2]. Most p53 mutations occur within the DNA-binding domain (DBD). The amino acid substitutions in mutant p53 (mutp53) may lead to substantial protein unfolding (structural mutations; e.g., R175H, Y220C, G245S), or to loss of DNA contacts, with no significant structural destabilization (contact mutations; e.g., R280K, R273H) [2,3]. Regardless of the type, mutp53 loses transcriptional, and therefore tumor-suppressive, activity. Hence, restoring wild-type (wt)-like activity to mutp53 is an appealing anticancer therapeutic strategy. In fact, extensive efforts have been made in the search for mutp53 reactivators [4]. Among the mutp53 reactivators disclosed to date, distinct molecular mechanisms have been reported. While some reactivators bind to mutp53, others display indirect reactivation mechanisms by targeting proteins like heat shock protein 40 (Hsp40), which promotes mutp53 refolding and subsequent re-establishment of DNA-binding ability [5]. Although several small molecule mutp53

reactivators have been reported to date, only APR-246 (PRIMA-1^{MET}) and COTI-2 are currently undergoing clinical trials [5].

Primary liver cancer presented the sixth highest incidence worldwide in 2018 [6], which is predicted to increase in the upcoming years [7]. Hepatocellular carcinoma (HCC), the most common histologic type of primary liver cancer, is associated with unfavorable prognosis, mainly due to high chemoresistance and recurrence rates [8,9]. The majority of patients are diagnosed at advanced-or terminal-stage, and available therapeutic options are restricted to symptomatic treatment or sorafenib, a multi-target kinase inhibitor [8,9]. Nonetheless, the increase of median overall survival of HCC patients treated with sorafenib is only 2.8 months [8], making the identification of effective therapeutic alternatives a high priority. About 30% of HCC harbor p53 mutations, correlating with increased invasiveness, recurrence, and lower survival rates [10,11]. This makes mutp53 a privileged therapeutic target in HCC. Herein, we unveil the new mutp53 reactivator SLMP53-1 with great potential as an anticancer agent, particularly against HCC.

2. Results

2.1. *SLMP53-2 Displays mutp53-Dependent Growth Inhibitory Effect in Human Tumor Cells, Leading to Cell Cycle Arrest, Apoptosis and Endoplasmic Reticulum (ER) Stress*

In our previous work, the tryptophanol-derived oxazoloisoindolinone SLMP53-1 was identified as a reactivator of mutp53-R280K with in vivo p53-dependent anti-tumor activity [12]. In order to search for new mutp53 reactivators, a small library of SLMP53-1 derivatives was synthesized. The activity of the compounds as potential mutp53 reactivators was investigated by analysis of their anti-proliferative effect on p53-null NCI-H1299 tumor cells ectopically expressing four prevalent mutp53 forms. By sulforhodamine B (SRB) assay, the compound SLMP53-2 (Figure 1A) was selected based on its marked reduction of the IC₅₀ values in NCI-H1299 cells expressing mutp53-R175H, -Y220C, or -G245S, compared to cells transfected with the empty vector (Figure 1B). These results evidenced the ability of SLMP53-2 to reactivate multiple structural mutp53. Interestingly, they also showed a distinct selectivity of SLMP53-1 and -2 towards different mutp53. In fact, unlike SLMP53-1 [12], SLMP53-2 was able to activate mutp53-Y220C, not significantly interfering with mutp53-R280K activity (Figure 1B).

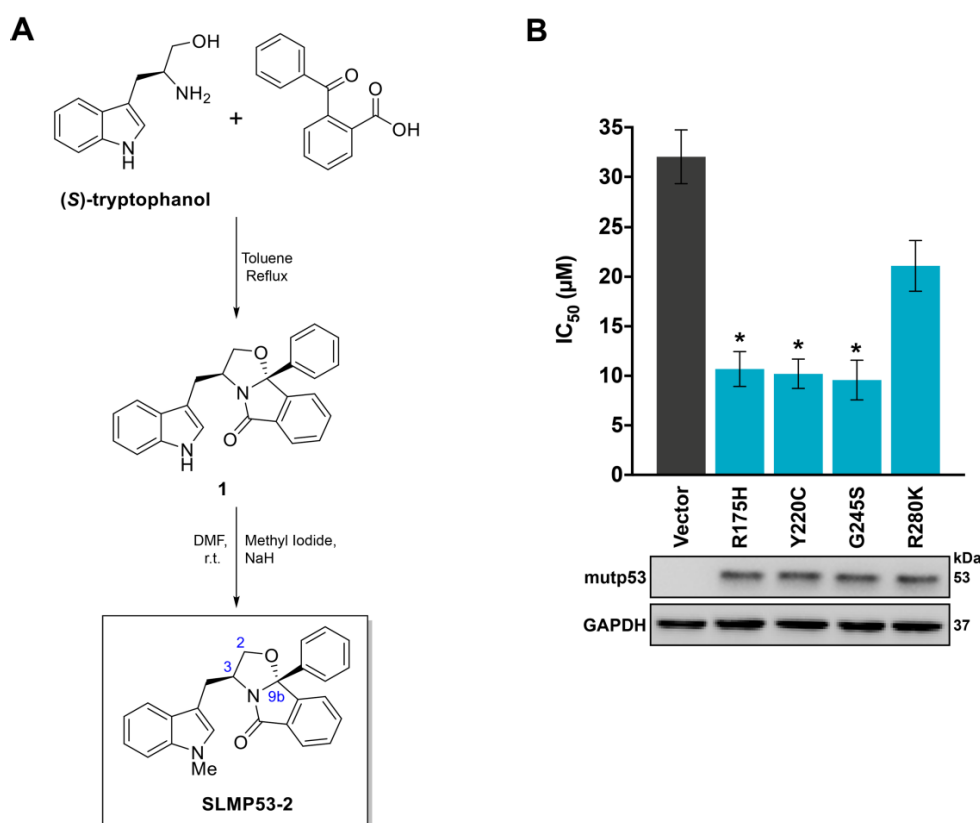


Figure 1. Growth inhibitory effect of SLMP53-2 in human tumor cells is dependent on structural mutp53. **(A)** Chemical synthesis of SLMP53-2. **(B)** IC₅₀ values of SLMP53-2, in p53-null H1299 cells transfected with pcDNA3 expressing different mutp53 or empty vector, were determined by SRB assay after 48h treatment with 3.12–50 µM SLMP53-2; data are mean ± SEM ($n = 5$); values significantly different from pcDNA3-Empty: * $p < 0.05$, one-way ANOVA with Dunnett's multiple comparison test. Mutp53 expression was confirmed by western blot; GAPDH was used as a loading control. Immunoblots represent one of three independent experiments.

For an in-depth analysis of the molecular mechanism of SLMP53-2, we focused on mutp53-Y220C, which is known to have a druggable hydrophobic pocket [13]. First, the growth inhibitory effect of SLMP53-2 against HuH-7 and HCC1419 cells endogenously expressing mutp53-Y220C was evaluated by SRB assay. As expected, SLMP53-2 inhibited the growth of both tumor cells with similar IC₅₀ values (Figure 2A), and higher potency than APR-246 (Figure 2B). Notably, the growth inhibitory activity of SLMP53-2 against non-tumoral HFF-1 cells (IC₅₀ of 50 µM) was significantly lower compared to tumor cells (Figure 2A). In HuH-7 cells, SLMP53-2 displayed a concentration-dependent growth inhibitory effect on colony formation (Figure 2C). We next assessed whether the growth inhibitory effect of SLMP53-2 in HuH-7 cells was associated with DNA damage. However, unlike the positive control (50 µM etoposide), no induction of H2AX phosphorylation (γH2AX) was detected after 14, 28, or 42 µM SLMP53-2 treatments (Figure 2D).

Consistently, 14 μ M SLMP53-2 did not promote mutp53 phosphorylation at Ser15 (Figure 2E), which is a major p53 phosphorylation site in response to genotoxic stresses [14]. A microarray analysis (GSE124021) indicated that 28 and 42 μ M SLMP53-2 led to the differential expression of more than 700 genes (four replicates for each treatment and DMSO (dimethyl sulfoxide) control, adjusted p value < 0.05 , log₂ fold change > 0.6 and < -0.6) in HuH-7 cells (Table S1, Figures S1 and S2). Pathway and upstream regulator analyses (Ingenuity Pathway, Metascape and Enrichr) identified signatures consistent with downregulation of cell cycle progression, upregulation of lipid metabolism and cell death, and ER stress induction (Figure 2F–H, Figures S1 and S2 and Table S2). In SLMP53-2-treated HuH-7 cells, *NUPR1*, *TP53* and *ATF4* were among the top scoring upstream regulators inferred from the gene expression dataset. *NUPR1* is an *ATF4* target and can contribute to ER stress responses, cell proliferation and apoptosis [15]. Gene expression changes showed that most *ATF4* target genes were upregulated, while the majority of *NUPR1* targets were downregulated (Figure 2H). This was expected as several *NUPR1* targets are involved in cell cycle and proliferation. Interestingly, downregulated genes were enriched for targets of miR-34a (Figure S2), which is a well-established p53-inducible microRNA [16]. Gene expression changes identified by microarray analysis were confirmed by qPCR for selected genes (Figure S2). The gene expression signature had similarities with molecules inducing apoptosis, autophagy or inhibiting the proteasome, based on Connectivity Map (Figure S3 and Table S3).

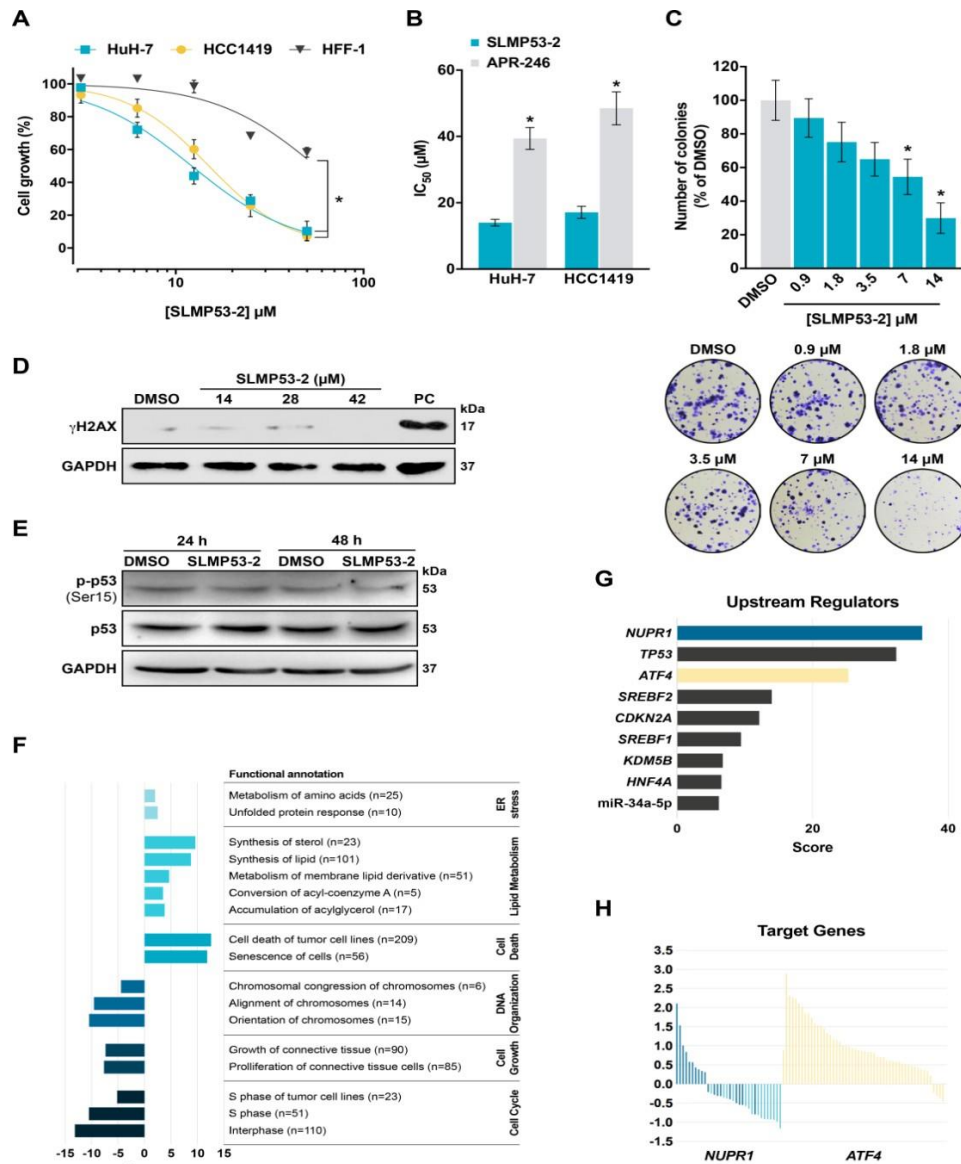


Figure 2. SLMP53-2 inhibits the growth of mutp53-Y220C-expressing tumor cells with no genotoxicity, leading to the differential expression of genes involved in cell cycle and death, lipid metabolism, and endoplasmic reticulum (ER) stress. **(A)** Concentration-response curves for SLMP53-2 in human non-tumoral HFF-1 and tumor mutp53-Y220C-expressing HuH-7 and HCC1419 cells, analyzed by sulforhodamine B (SRB) assay after 48 h treatment with 3.12–50 μM SLMP53-2. Data are mean \pm SEM ($n = 5$); * $p < 0.05$, extra sum-of-squares F test. **(B)** IC₅₀ values of SLMP53-2 and APR-246 in HuH-7 and HCC1419 cells were determined by SRB assay after 48 h treatment with 3.12–50 μM SLMP53-2 or APR-246. Data are mean \pm SEM ($n = 5$); * $p < 0.05$, two-way ANOVA with Sidak's multiple comparison test. **(C)** Effect of SLMP53-2 in HuH-7 cell colony formation, analyzed after 14 days incubation with SLMP53-2; a representative experiment is shown. Data are mean \pm SEM ($n = 5$); values significantly different from DMSO: * $p < 0.05$, one-way ANOVA with Dunnett's multiple comparison test. **(D)** Levels of γH2AX in HuH-7 cells treated with SLMP53-2; 50 μM etoposide was used as a positive control (PC). **(E)** Levels of mutp53 phosphorylation at Ser15 in HuH-7 cells treated with 14 μM SLMP53-2. In **(D,E)**, immunoblots represent one of three independent experiments; glyceraldehyde 3-phosphate dehydrogenase (GAPDH) was used as a loading control. **(F)** Top enriched biological pathways grouped by broad categories based on Ingenuity Pathway Analysis (IPA) starting from the dataset of differentially expressed genes (DEGs) from HuH-7

cells treated with 28 μM SLMP53-2. The number of features for each functional annotation is given in parenthesis. The score combines the \log_{10} p -value and predicted pathway activation or repression status of the corresponding pathway/process, respectively for positive and negative score. The different colors correspond to the different functional annotation categories. (G) Top scoring upstream regulators inferred from the same gene expression dataset. The score is the \log_{10} p -value of the predicted activation status. (H) Gene expression changes of *NUPR1* (blue) and *ATF4* (yellow) target genes in SLMP53-2-treated HuH-7 cells.

In accordance with microarray data, 14 and 28 μM SLMP53-2 induced G0/G1-phase cell cycle arrest (Figure 3A) and apoptosis (Figure 3B), in HuH-7 cells. Moreover, consistently with the induction of an ER stress response, 28 μM SLMP53-2 increased the levels of XBP1 nuclear protein (Figure 3C and Figure S4), spliced XBP1 (sXBP1) mRNA (Figure 3D), and phosphorylated eIF2 α (Figure 3E).

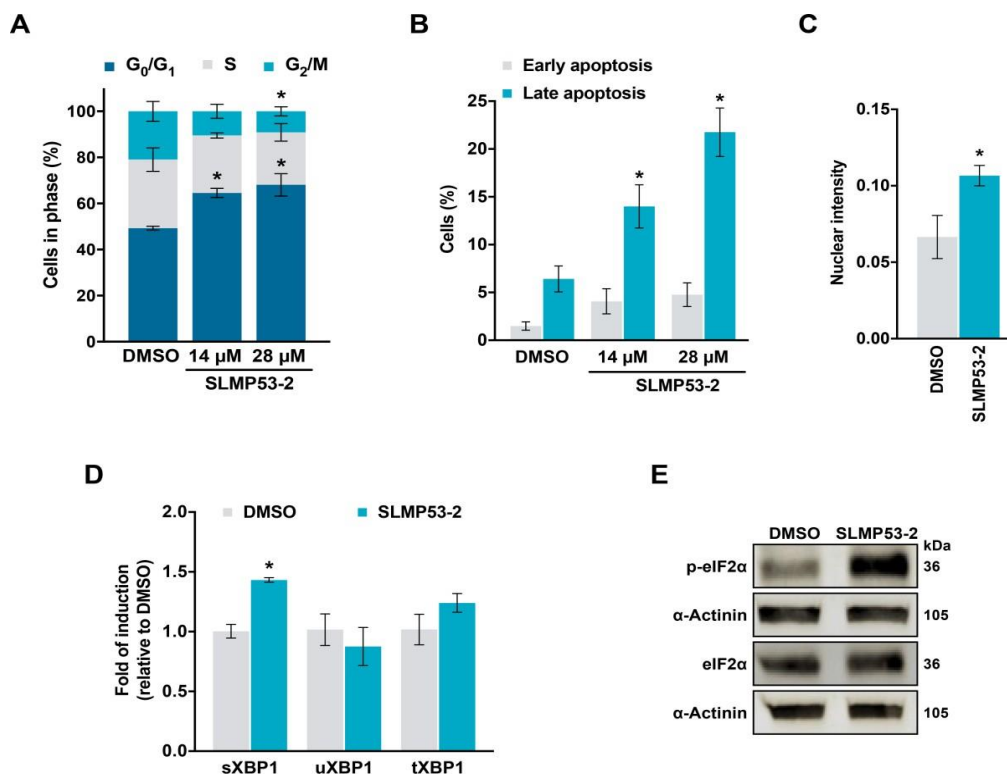


Figure 3. Growth inhibitory effect of SLMP53-2 in hepatocellular carcinoma (HCC) cells is associated with cell cycle arrest, apoptosis, and ER stress. (A) Effect of SLMP53-2 on cell cycle progression of HuH-7 cells after 48 h treatment; values significantly different from DMSO: * $p < 0.05$, two-way ANOVA with Dunnett's multiple comparison test. (B) Effect of SLMP53-2 on apoptosis of HuH-7 cells, after 72 h treatment. Data are mean \pm SEM ($n = 5$); values significantly different from DMSO: * $p < 0.05$, one-way ANOVA with Dunnett's multiple comparison test. (C) Quantification of nuclear fluorescence intensity of XBP1 in HuH-7 cells after 24 h treatment with 28 μM SLMP53-2. Data are mean \pm SEM ($n = 3$); values significantly different from DMSO: * $p < 0.05$, unpaired Student's t -test. (D) mRNA levels of spliced (sXBP1), unspliced (uXBP1), and total XBP1 (tXBP1) in HuH-7 cells after 24 h treatment with 28 μM SLMP53-2, determined by RT-qPCR; fold of induction is relative to DMSO. Data are mean \pm SEM ($n = 3$); values significantly different from DMSO: * $p < 0.05$, two-way ANOVA with Dunnett's multiple comparison test. (E) Protein levels of phosphorylated and total eIF2 α in HuH-7 cells, after 24 h treatment

with 28 μ M SLMP53-2. Immunoblots represent one of three independent experiments; α -actinin was used as a loading control.

2.2. SLMP53-2 Restores WT-Like Conformation and Transcriptional Activity to mutp53-Y220C in HCC Cells

We next evaluated the effect of SLMP53-2 on the expression levels of several p53 target genes. By western blot, it was observed that 14 μ M SLMP53-2 increased the protein levels of MDM2, p21, GADD45, BAX, and KILLER, while downregulating survivin and VEGF, in HuH-7 cells, an effect abolished in HuH-7 p53KO cells (Figure 4A). It is of note that in mutp53-Y220C-expressing HCC1419 cells, 14 μ M SLMP53-2 also interfered with the protein levels of several p53 target genes, increasing MDM2, p21, and KILLER, and decreasing survivin and VEGF (Figure S5).

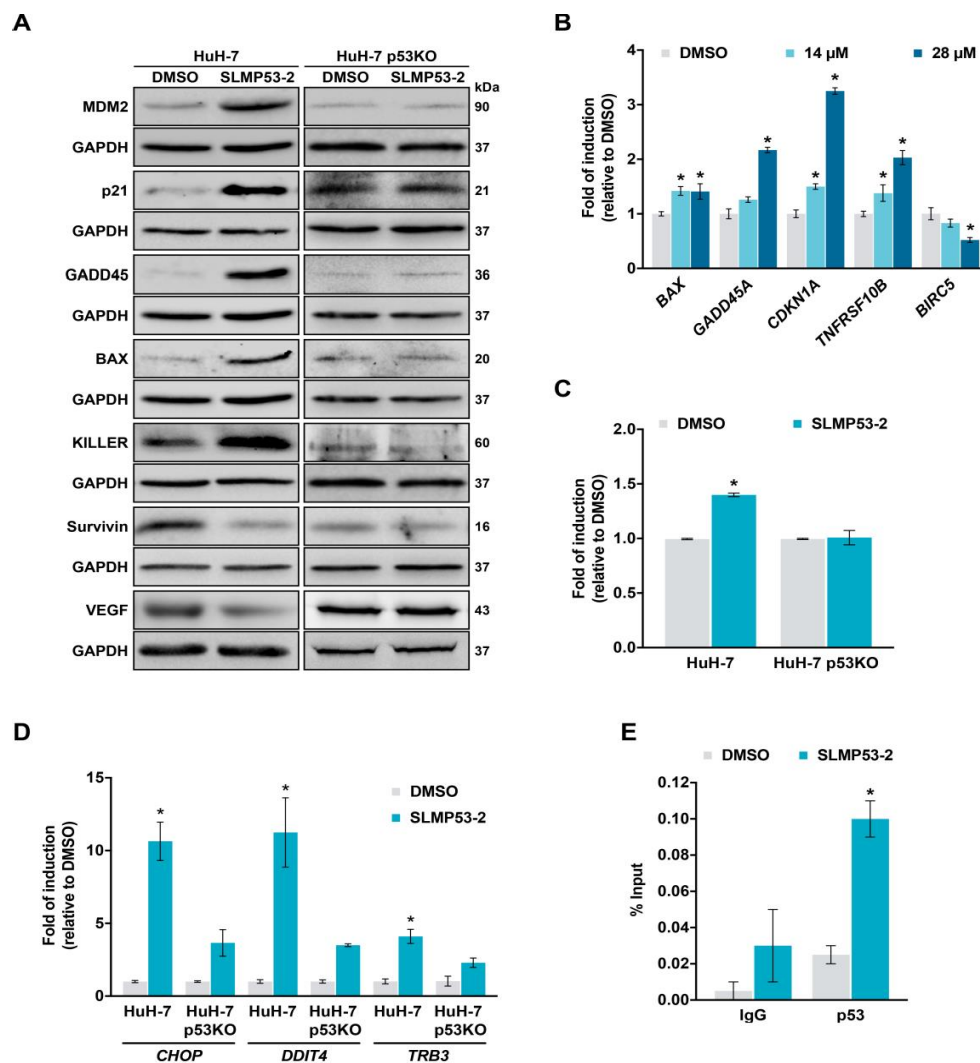


Figure 4. SLMP53-2 induces p53 transcriptional targets, including miR-34a and genes involved in ER stress response, and restores DNA-binding ability to mutp53-Y220C in HCC cells. (A) Protein levels of p53 target genes in parental and p53KO HuH-7 cells, after 16 h (p21), 24 h (survivin, VEGF) or 48 h (MDM2, GADD45, BAX, KILLER) treatment with 14 μ M SLMP53-2. Immunoblots represent one of three independent experiments; GAPDH was used as a loading control. (B) mRNA

levels of p53 target genes, in HuH-7 cells, after 24 h treatment with 14 and 28 μ M SLMP53-2, determined by RT-qPCR; fold of induction is relative to DMSO. (C) miR-34a levels in parental and p53KO HuH-7 cells, after 24 h treatment with 28 μ M SLMP53-2, determined by RT-qPCR; fold of induction is relative to DMSO. (D) mRNA levels of genes involved in the ER stress response, in parental and p53KO HuH-7 cells, after 24 h treatment with 28 μ M SLMP53-2, determined by RT-qPCR; fold of induction is relative to DMSO. (E) Analysis of the occupancy of mutp53-Y220C on the p21 promoter in HuH-7 cells, determined by ChIP, after 24 h treatment with 28 μ M SLMP53-2 or DMSO; immunoprecipitation was performed with an anti-p53 antibody (p53) or an anti-mouse IgG as a negative control (IgG); the enrichment of DNA fragments was analyzed by RT-qPCR using site-specific primers. In A–E, data are mean \pm SEM ($n = 3$); values significantly different from DMSO (B–E): * $p < 0.05$, two-way ANOVA with Dunnett's (B,E) or Sidak's (D) multiple comparison test; * $p < 0.05$, unpaired Student's t -test (C).

In HuH-7 cells, the regulation of p53 target genes by 14 and 28 μ M SLMP53-2 was further confirmed at mRNA level with the upregulation of *BAX*, *GADD45*, *CDKN1A* (p21), and *TNFRSF10B* (KILLER), and the downregulation of *BIRC5* (survivin) (Figure 4B). Consistently with the microarray analysis, 28 μ M SLMP53-2 also upregulated miR-34a in HuH-7, but not in HuH-7-p53KO cells (Figure 4C). Moreover, 28 μ M SLMP53-2 significantly enhanced the expression of p53 target genes involved in the ER stress response, namely *CHOP* and *DDIT4*, as well as of *TRB3* (a *CHOP* target gene [17–19]) in HuH-7, but not in HuH-7-p53KO cells (Figure 4D). The reestablishment of mutp53-Y220C transcriptional activity was further supported by chromatin immunoprecipitation (ChIP). In fact, 28 μ M SLMP53-2 significantly increased mutp53-Y220C occupancy at the p21 promoter (Figure 4E), reflecting the restoration of p53 DNA-binding ability.

As a structural mutp53, we investigated the ability of SLMP53-2 to restore wt-like folding to mutp53-Y220C, through immunoprecipitation (IP) using PAb1620 (wt/folded) and PAb240 (mut/unfolded) conformation-specific antibodies. The results showed that 42 μ M SLMP53-2 visibly increased the amount of p53 precipitated with PAb1620, while decreasing the amount of p53 precipitated with PAb240 (Figure 5A). Consistently, 42 μ M SLMP53-2 visibly increased PAb1620 and decreased PAb240 immunofluorescence staining in HuH-7 cells (Figure S6).

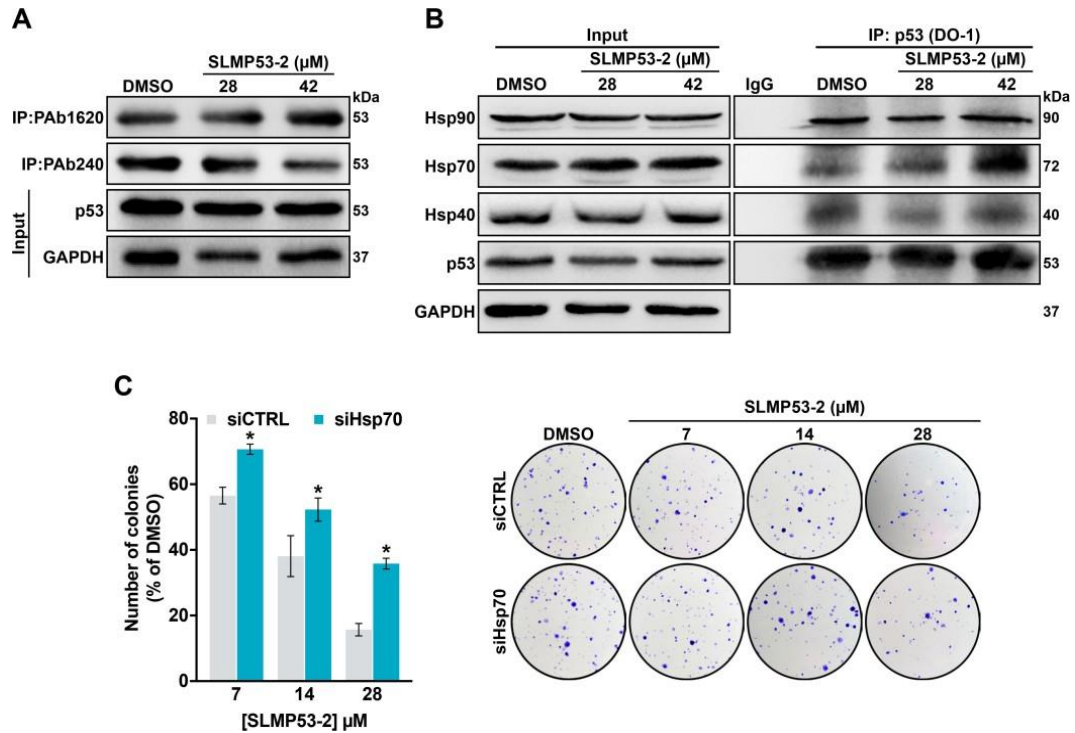


Figure 5. SLMP53-2 restores wt-like folding and promotes mutp53-Y220C interaction with Hsp70. **(A)** Immunoprecipitation of p53 in HuH-7 cells treated with 28 and 42 μM SLMP53-2 for 36 h, using the conformation-specific antibodies PAb240 (mut/unfolded) and PAb1620 (wt/folded), followed by immunoblotting with anti-p53 (DO-1) or anti-Hsp70 antibodies; whole cell lysate (input). Of note that labelling with PAb1620 in DMSO-treated cells may be explained by mutp53-Y220C temperature-sensitivity [20]. **(B)** Co-immunoprecipitation of Hsp40, Hsp70, and Hsp90 with p53 in HuH-7 cells treated with 28 and 42 μM SLMP53-2 or DMSO for 36 h, using anti-p53 antibody (DO-1), followed by immunoblotting with anti-Hsp40, anti-Hsp70, anti-Hsp90, and anti-p53 antibodies; whole cell lysate (input). **(C)** Effect of SLMP53-2 in the cell colony formation of HuH-7 cells transfected with siRNA against Hsp70 (siHsp70) or control siRNA (siCTRL), analysed after 14 days incubation with SLMP53-2; a representative experiment is shown. Data are mean ± SEM ($n = 5$); values significantly different from siCTRL: * $p < 0.05$, one-way ANOVA with Dunnett's multiple comparison test. In **(A,B)**, immunoblots represent one of three independent experiments; GAPDH was used as a loading control.

2.3. Hsp70 is a Potential Mediator of mutp53-Y220C Reactivation by SLMP53-2

To determine the mechanism by which SLMP53-2 would affect mutp53-Y220C function, we checked whether SLMP53-2 could bind to this mutp53. However, despite the presence of a druggable hydrophobic pocket in mutp53-Y220C, no binding of SLMP53-2 to recombinant mutp53-Y220C DBD was detected by heteronuclear single-quantum coherence (HSQC)-NMR (Figure S7).

Chaperones from the Hsp40, Hsp70, and Hsp90 families have long been recognized as mutp53-binding partners capable of folding mutp53 to the wt-like conformation [21–23]. Therefore, we interrogated whether SLMP53-2 could reactivate mutp53-Y220C by promoting its interaction with these chaperones. To investigate potential interactions between mutp53-Y220C and Hsp40/Hsp70/ Hsp90, co-immunoprecipitation (co-IP) experiments were performed in HuH-7 cells. Conversely to that observed with Hsp40 and Hsp90, 42 μ M SLMP53-2 visibly increased the amount of Hsp70 precipitated with p53 (Figure 5B), indicating an enhancement of Hsp70 binding to p53. Moreover, in Hsp70 siRNA silenced HuH-7 cells (Figure S8), the inhibitory effect of SLMP53-2 on colony formation was significantly reduced (Figure 5C). Therefore, SLMP53-2 may restore wt-like conformation to mutp53-Y220C through enhancement of its interaction with Hsp70.

2.4. SLMP53-2 Sensitizes HCC Cells to Sorafenib

A potential synergistic association between SLMP53-2 and sorafenib was assessed by SRB assay, in HuH-7 cells. When combined with 1.5 μ M SLMP53-2, sorafenib displayed significantly higher growth inhibitory effect compared to its effect as a single agent (Figure 6A). Consistently, a synergistic effect ($CI < 1$) was obtained for all tested sorafenib concentrations in combination with 1.5 μ M SLMP53-2 (Figure 6B).

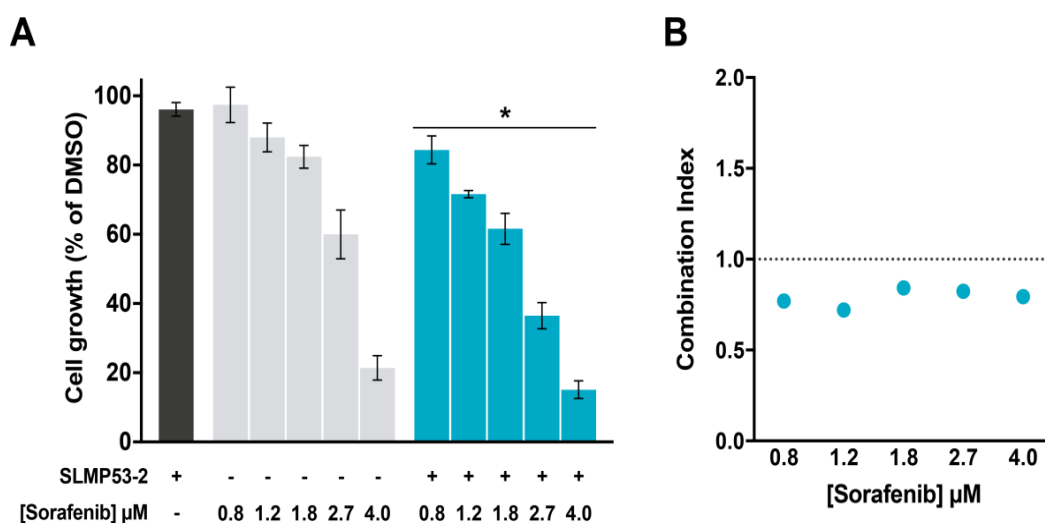


Figure 6. SLMP53-2 synergizes with sorafenib in HCC cells. HuH-7 cells were treated with increasing concentrations of sorafenib, alone and in combination with 1.5 μM SLMP53-2. (A) Cell growth was measured by SRB assay after 48 h treatment; growth obtained with control (DMSO) was set as 100%. Data are mean \pm SEM ($n = 4$); values significantly different from chemotherapeutic alone: * $p < 0.05$, two-way ANOVA. (B) Combination index (CI) values calculated using the CompuSyn software for each combined treatment. $\text{CI} < 1$, synergy; $1 < \text{CI} < 1.1$, additive effect; $\text{CI} > 1.1$, antagonism. CI values were calculated using a mean value effect ($n = 4$).

2.5. SLMP53-2 Displays In Vivo Anti-Tumor Activity in HCC Xenograft Mouse Models, with No Apparent Toxic Side Effects

The toxicity profile of SLMP53-2 was evaluated in Wistar rats subjected to five intraperitoneal administrations of 50 mg/kg SLMP53-2 or vehicle, followed by analysis of hematological and biochemical parameters from blood samples (Table S4). Although a slight reduction of the red cell distribution width and mean platelet volume was observed upon SLMP53-2 treatment, these values were within the reference range [24]. Therefore, no undesirable hematological and biochemical toxicity was induced by SLMP53-2 in vivo.

To evaluate the in vivo anti-tumor activity of SLMP53-2, five intraperitoneal administrations of 50 mg/kg SLMP53-2 or vehicle were performed in nude mice carrying HuH-7 xenografts. A pronounced reduction of tumor volume (Figure 7A) and weight (Figure 7B) was observed in SLMP53-2-treated mice compared to vehicle. Moreover, nude mice showed no significant variation of body weight throughout the experiment (Figure 7C), and no significant differences were observed between the weight of spleen, liver, heart, and kidneys of SLMP53-2-treated mice and vehicle (Figure 7D). These results further supported a favorable therapeutic index of SLMP53-2 in vivo. Additionally, the immunohistochemistry (IHC) staining of tumor sections revealed that SLMP53-2 decreased Ki-67 and VEGF, and increased BAX staining (Figure 7E–G), compared to vehicle. Altogether, these results unveiled a potent in

vivo anti-tumor activity of SLMP53-2 through induction of apoptosis and inhibition of cell proliferation and angiogenesis.

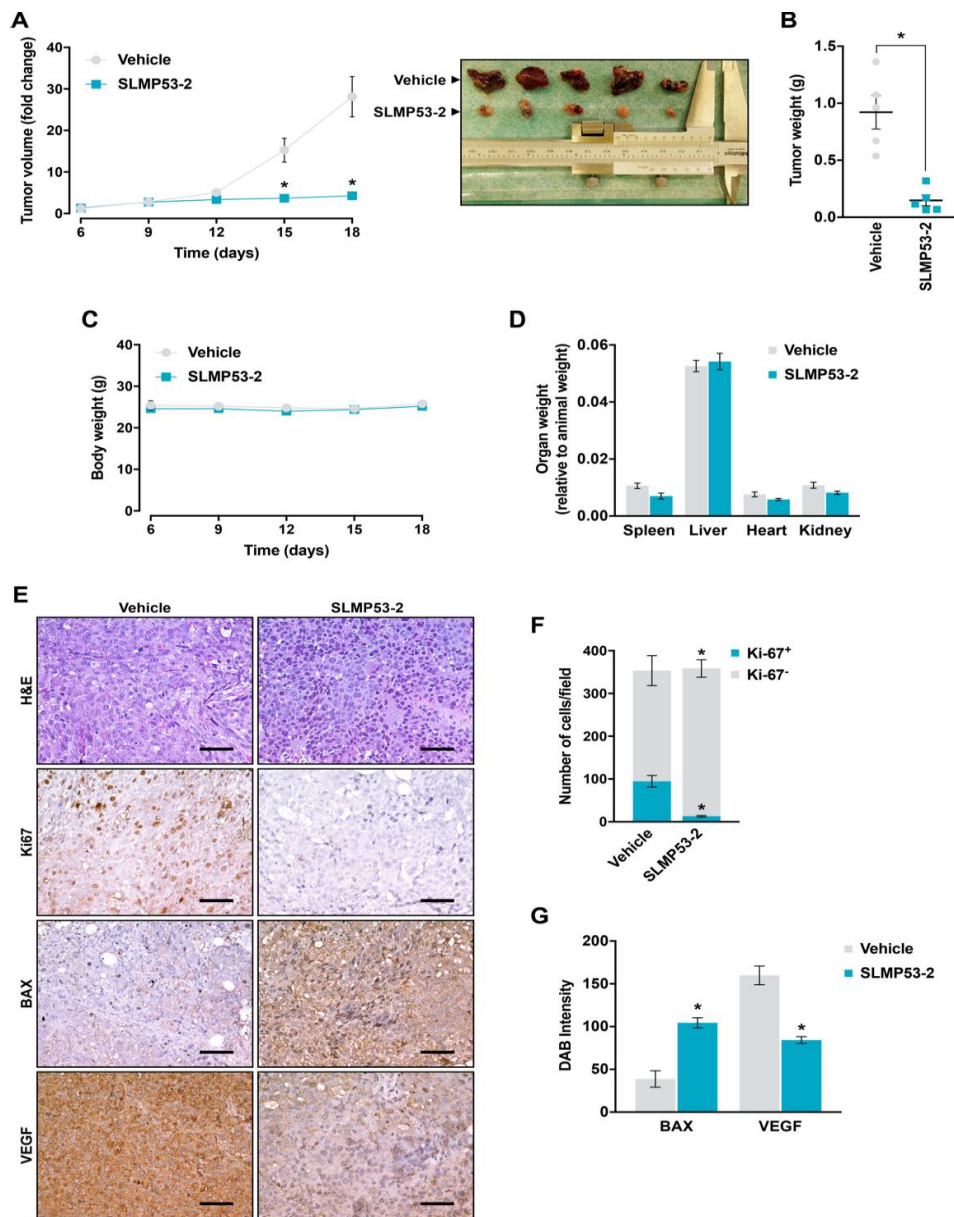


Figure 7. In vivo anti-tumor activity of SLMP53-2. Swiss nude mice carrying HuH-7 xenografts were treated with 50 mg/kg SLMP53-2 or vehicle, by intraperitoneal injection twice a week, for a total of five administrations. **(A)** Tumor volume curves of mice carrying HuH-7 xenografts treated with SLMP53-2 or vehicle; image of vehicle and SLMP53-2-treated tumors at the end of treatment. **(B)** Tumor weights measured at the end of the experiment; value significantly different from vehicle: * $p < 0.05$, unpaired Student's t -test. **(C)** Mice body weight during treatment with SLMP53-2 or vehicle. **(D)** Weight of spleen, liver, heart and kidneys, relative to animal weight, in animals treated with SLMP53-2 or vehicle. **(E)** Representative images of Ki-67, BAX, and VEGF detection in tumor tissues of HuH-7 xenografts treated with SLMP53-2 or vehicle, collected at the end of treatment (scale bar = 20 μ m; magnification = 200 \times); hematoxylin and eosin (H&E).

(F,G) Quantification of immunohistochemistry of HuH-7 xenograft tumor tissues treated with SLMP53-2 or vehicle; in **(F)**, quantification of the number of Ki-67 positive and negative cells ($n = 5$); in **(G)**, BAX and VEGF staining were quantified by evaluation of 3,3'-diaminobenzidine (DAB) intensity ($n = 5$); values significantly different from vehicle: * $p < 0.05$, unpaired Student's t -test. In **(A,D)**, data are mean \pm SEM ($n = 5$). In **(A)** and **(F)**, values significantly different from vehicle: * $p < 0.05$, two-way ANOVA with Sidak's multiple comparison test. In **(C,D)**, values not significantly different from vehicle: $p > 0.05$, two-way ANOVA with Sidak's multiple comparison test.

3. Discussion

The advances in understanding cancer pathobiology have supported the crucial role of mutp53 in all hallmarks of cancer, rendering mutp53 reactivation one of the most promising therapeutic strategies in cancer treatment. The reactivation of mutp53 also poses a great opportunity in combination therapy with conventional chemotherapies known to trigger cancer cell death through an active p53-dependent pathway. Nonetheless, drugging mutp53 has shown to be a challenging task, with no mutp53 reactivators still available for clinical use. In fact, although the potential of reactivating wt-like function to mutp53 with canonical genes transcription has been proven, it does not always translate into halting tumor growth [1,2,4,5].

In this work, we report the identification of SLMP53-2 as a novel reactivator of mutp53, with p53-dependent growth inhibitory effect on human tumor cells through induction of cell cycle arrest and apoptosis. Interestingly, SLMP53-2 stimulates the ER stress response by inducing the expression of several ER stress markers, including the p53-target gene *CHOP*, which triggers ER stress-related cell death [25]. ER stress occurs when the tightly-regulated protein folding environment of the ER is disrupted, causing accumulation of unfolded proteins. This triggers the unfolded protein response (UPR), a mechanism intended to re-establish ER homeostasis. When the UPR fails to restore ER homeostasis, cell death is triggered [25]. In fact, ER stress exacerbation for cell death induction has been proposed as a relevant anticancer therapeutic strategy, specifically against HCC [26]. Particularly, the prodrug of thapsigargin, mipsagargin (a known ER stress inducer through interference with ER calcium levels) was tested in patients with solid tumors, including HCC [27]. Moreover, zebularine (a DNA methyltransferase inhibitor) has been reported to induce p53-dependent ER stress-mediated cell death in colorectal cancer cells [28]. Interestingly, the mutp53 reactivators APR-246 and PK11007 have also been reported to induce ER stress-mediated cell death in mutp53-expressing tumor cells [29,30]. Herein, SLMP53-2 is also shown to restore wt-like folding and DNA-binding ability to mutp53-Y220C. In fact, SLMP53-2 reactivates p53 transcriptional activity, regulating the expression of several p53 transcriptional targets involved in cell cycle arrest (p21, GADD45), apoptosis (BAX, KILLER, survivin), ER stress response (CHOP, DDIT4), and angiogenesis (VEGF). Interestingly, SLMP53-2 causes p53-dependent reduction of the expression levels of survivin, which is frequently overexpressed in HCC, correlating with increased invasion and metastasis, and decreased overall and relapse-free survival [31–33]. Additionally, SLMP53-2 upregulates miR-34a, a p53 transcriptional target. Consistently, the microarray data revealed that SLMP53-2 leads to downregulation of several miR-34a targets. miR-34a is a crucial tumor suppressor that controls cellular processes including proliferation, apoptosis, senescence, and stemness [34]. This is of particular interest in HCC, in which miR-34a downregulation is common and frequently associated with invasion and metastasis [35]. Consistently, MRX34, a liposomal miR-34a mimic, has displayed promising anti-tumor activity in orthotopic HCC models [36], having

recently completed phase I clinical trials for advanced solid tumors, including HCC [37].

Despite its inability to bind to mutp53-Y220C, SLMP53-2 enhances the mutp53-Y220C interaction with chaperone Hsp70. In fact, Hsp70 is a known mutp53 binding partner, leading to its refolding and protein stabilization, with subsequent restoration of DNA-binding and transcriptional activity [21–23]. A similar mutp53 reactivation mechanism was recently reported for chetomin, which restores wt-like function to mutp53-R175H by enhancing its interaction with Hsp40 [38]. Interestingly, the requirement of Hsp70 for mutp53-R175H stabilization, and its contribution to the pancreatic cells malignant transformation have been recently reported [39]. However, these observations were conducted in non-tumoral cells. A cell context-dependence of the Hsp70 effect on mutp53 might justify the distinct observations made in the current work. The anti-proliferative effect of SLMP53-2 on p53-null tumor cells ectopically expressing four prevalent mutp53 forms supports its ability to reactivate structural mutp53 forms, including R175H, Y220C, and G245S. These results are reinforced by the capability of SLMP53-2 to restore mutp53-Y220C transcriptional activity in HCC cells endogenously expressing this mutp53. The activation of mutp53-Y220C transcriptional activity by SLMP53-2 was also evidenced in breast tumor cells expressing this mutp53, indicating its potential to reactivate mutp53 in distinct tumor cell types. It is also worth noting that SLMP53-2 has antitumor activity against wtp53-expressing tumor cells, namely HCC HepG2 cells (IC_{50} of $12.5 \pm 0.8 \mu\text{M}$; Figure S10A). In fact, a wtp53-dependent growth inhibitory effect could be evidenced for SLMP53-2, which showed a two-fold reduction in the IC_{50} value in HCT116 colon tumor cells expressing wtp53 (IC_{50} of $8.4 \pm 1.1 \mu\text{M}$) compared to its isogenic p53-null derivative (IC_{50} of $17.7 \pm 2.3 \mu\text{M}$) (Figure S10B). This is consistent with the proposed mechanism of action of SLMP53-2, since the stabilization of wtp53 by Hsp70 has also been reported [22].

In our previous work, SLMP53-1 was identified as a reactivator of mutp53 [12]. Despite being chemical derivatives, several structural differences can be found between SLMP53-1 and -2. In particular, SLMP53-2 has a phenyl instead of a methyl group in position 9b, and its indole nitrogen is protected with a methyl group. It is well-known that small structural modifications can completely change the activity of a compound on a specific target, since with the introduction of a certain group, the compound may no longer fit into the pocket of the target protein losing its activity. Moreover, it is currently accepted that structurally related drugs often act against distinct targets. In fact, only a small number of drugs that share the same or overlapping targets are structurally related [39]. As such, although both SLMP53-1 and -2 act as mutp53 reactivators, the inability of SLMP53-1 to reactivate the structural mutp53-Y220C, having effect on contact mutp53-R280K, allow us to predict a distinct mechanism of mutp53 reactivation. This hypothesis is supported by the inability of SLMP53-1 to enhance the Hsp70 interaction with mutp53-Y220C in HuH-7 cells (Figure S11), and it may explain their capability to reactivate distinct mutp53, as well as their distinct growth inhibitory activity towards tumor cells. Considering the relevance of mutp53 in the HCC pathogenesis and the lack of therapeutic alternatives for this cancer [10,11], this work also paves

the way to a potential application of SLMP53-2 (alone or in combination therapy) in HCC treatment. Moreover, besides its growth inhibitory activity against HCC cells (superior to that of APR-246, currently in phase Ib/II clinical trials [5]), SLMP53-2 also sensitizes HCC cells to sorafenib, the only drug currently approved for the treatment of advanced HCC [8,9]. Importantly, in the HCC xenograft mouse model, SLMP53-2 displays pronounced antitumor activity associated with induction of apoptosis and inhibition of cell proliferation and angiogenesis. Interestingly, the crucial role of angiogenesis in HCC development and dissemination has been widely explored for the development of targeted therapies [40]. In fact, antiangiogenic agents, like sorafenib, have been the only targeted drugs with positive results in clinical trials for HCC [40]. Notably, SLMP53-2 also displays a favorable in vivo toxicological profile, with no significant alteration of toxicological parameters related to liver function. This is of particular importance in HCC, as patients often display liver cirrhosis that can lead to impaired liver function and consequently increased drug toxicity [41].

4. Materials and Methods

4.1. Compounds and Antibodies

Sorafenib, etoposide, and APR-246 were purchased from Santa Cruz Biotechnology (Heidelberg, Germany), Calbiochem (VWR, Carnaxide, Portugal), and Sigma-Aldrich (Sintra, Portugal), respectively. All antibodies are listed in Table S5.

4.2. Chemical Synthesis of SLMP53-2

4.2.1. General Methods

All reagents and solvents were obtained from commercial suppliers and used without further purification. Reactions were performed under a nitrogen atmosphere. Melting point was determined using a Kofler camera Bock monoscope M (Lisboa, Portugal). Thin layer chromatography was performed using silica gel 60 F₂₅₄ plates (Merck, Darmstadt, Germany) and visualized by ultraviolet (UV) light. For flash column chromatography high purity grade Merck silica gel (200–400 mesh) was used. ¹H- and ¹³C-NMR spectra were recorded on a Fourier 300 Avance instrument (Bruker, Fällanden, Zurich, Switzerland) at 300 MHz (¹H-NMR) and at 75 MHz (¹³C-NMR). ¹H- and ¹³C-NMR chemical shifts are reported in parts per million (ppm, δ) referenced to the solvent used. Proton coupling constants (*J*) are expressed in hertz (Hz). Multiplicities are given as: s (singlet), dd (doublet of doublet), and m (multiplet). The specific rotation value was measured at r.t. on a 241 MC polarimeter (PerkinElmer, Waltham, MA, USA; New University of Lisbon, PT). Compound SLMP53-2 showed purity $\geq 90\%$ by LC-MS, performed in an Alliance 2695 HPLC system (Waters, Dublin, Ireland) equipped with a Waters SunFire C18 column (100 \times 2.1 mm; 5 μ M) at 35 °C, using as mobile phase a gradient from 95% solution A (Milli-Q water containing 0.5%

formic acid (v/v)) to 95% solution B (acetonitrile), and employing a photodiode array detector to scan wavelength absorption from 210 to 600 nm; MS experiments were performed on Micromass[®] Quattro Micro triple quadrupole (Waters[®], Dublin, Ireland) with an electrospray in positive ion mode (ESI+), ion source at 120 °C, capillary voltage of 3.0 kV and source voltage of 30 V, at the Liquid Chromatography and Mass Spectrometry Laboratory, Faculty of Pharmacy, University of Lisbon.

4.2.2. Chemical Synthesis of SLMP53-2

Compound **1** was prepared from (*S*)-tryptophanol (0.16 g, 0.84 mmol, 1.0 equivalent) and 2-benzoyl-benzoic acid (0.21 g, 0.93 mmol, 1.1 equivalent) in 10 mL of toluene, according to the protocol described in reference [42]. To a stirred solution of compound **1** (0.10 g, 0.26 mmol) in anhydrous DMF (3 mL) at 0 °C, and under inert atmosphere of nitrogen, 0.014 g of NaH (0.58 mmol,

2.2 equivalent, 95% anhydrous reagent) was added. After stirring for 30 min, 0.025 mL of methyl iodide (0.39 mmol, 1.5 equivalent) was added and the reaction was slowly allowed to warm to room temperature for 1 h. Ethyl acetate (10 mL) was added, and the organic phase washed with water (6 × 10 mL), with an aqueous saturated solution of NaHCO₃ and then with a brine solution. The organic phase was dried with Na₂SO₄ and concentrated. After flash chromatography (ethyl acetate/*n*-hexane 1:1) and recrystallization from EtOAc, SLMP53-2 was obtained as a white crystalline solid (0.096 g, 89.3%); mp: 134–136 °C; $[\alpha]_D^{20} = +84.5$ ($c = 0.37$, CH₂Cl₂). ¹H-NMR (CDCl₃) δ 7.84–7.77 (m, 1H, ArH), 7.67–7.59 (m, 2H, ArH), 7.53–7.45 (m, 3H, ArH), 7.42–7.35 (m, 3H, ArH), 7.22 (m, 3H, ArH), 7.12–7.05 (m, 1H, ArH), 6.96 (s, 1H, ArH), 4.69 (m, 1H, H-3), 4.46 (dd, $J = 8.6, 7.6$ Hz, 1H, H-2), 3.98 (dd, $J = 8.6, 6.8$ Hz, 1H, H-2), 3.72 (s, 3H, NCH₃), 3.21 (dd, $J = 14.7, 5.5$ Hz, 1H, CH₂-indole), 2.65 (dd, $J = 14.7, 9.3$ Hz, 1H, CH₂-indole); ¹³C-NMR (CDCl₃) δ 174.72 (C = O), 147.29 (Cq), 138.98 (Cq), 136.98 (Cq), 133.38 (ArCH), 131.22 (Cq), 130.20 (ArCH), 128.87 (ArCH), 128.76 (ArCH), 128.01 (Cq), 127.01 (CH-indole), 125.92 (ArCH), 124.48 (ArCH), 123.56 (ArCH), 121.75 (ArCH), 119.01 (ArCH), 110.29 (Cq), 109.26 (ArCH), 101.06 (C-9b), 76.43 (CH-2), 55.91 (CH-3), 32.77 (N-CH₃), 30.15 (CH₂-indole); MS (ESI) m/z calcd for C₂₆H₂₂N₂O₂: 394, found 395 [M + H]⁺.

4.3. Human Cell Culture Conditions

Human non-small cell lung carcinoma NCI-H1299, breast ductal carcinoma HCC1419, and non-tumorigenic foreskin fibroblast HFF-1 cell lines were purchased from ATCC (Rockville, MD, USA). The human HCC HuH-7 cell line was purchased from the JCRB cell bank (Osaka, Japan). The p53 knock-out (KO) HuH-7 cell line was generated using CRISPR editing [43]. Tumor cells were cultured in RPMI-1640 medium with UltraGlutamine (Lonza, VWR, Basel, Switzerland) with 10% FBS (Gibco, Alfacene, Lisboa, Portugal). HFF-1 cells

were cultured in DMEM:F12 (Lonza) with 10% FBS. Cells were maintained in a humidified incubator at 37 °C with 5% CO₂. Routine testing for

Mycoplasma was performed using the MycoAlert™ PLUS detection kit (Lonza).

4.4. *Transfection, Cell Proliferation, and Combination Therapy Assays*

4.4.1. Construction of Mammalian Expression Vectors

The full-length coding sequences of mutp53 were PCR-amplified from pLLS89 yeast vectors (kindly provided by Dr Gilberto Fronza, from IST Istituto Nazionale per la Ricerca sul Cancro, Italy) with Vent DNA polymerase (New England Biolabs, Werfen, Porto, Portugal), using the primers pair 5'^J GGG GTA CCA TGG AGG AGC CGC AGT CAG 3'^J and 5'^J CCG CTC GAG TCA GTC TGA GTC AGG CCC TTC 3'^J, where the restriction sites for KpnI/XhoI (in bold) were included, respectively.

The PCR products and the mammalian expression vector pcDNA3 (Invitrogen, Alfacene, Lisbon, Portugal) were digested with KpnI/XhoI (New England Biolabs, Werfen, Carnaxide, Portugal), purified from agarose gel, and ligated with T4 DNA ligase (Promega, VWR, Carnaxide, Portugal), originating the expression vectors pcDNA3-mutp53. These constructs were propagated in NZY5α *Escherichia coli* cells (NZYTech, Lisbon, Portugal). The sequence of each mutp53 in the constructed vectors was confirmed by sequencing (Eurofins GATC Biotech, Konstanz, Germany) with specific pcDNA3 primers. pcDNA3-mutp53 vectors were extracted using the PureYield™ Plasmid Miniprep System kit (Promega, VWR, Carnaxide, Portugal).

4.4.2. Transfection

For ectopic mutp53 expression, p53-null NCI-H1299 cells were transfected with the previously obtained pCDNA3 plasmid encoding mutp53-R175H, -Y220C, -G245S, or -R280K, or empty pCDNA3. For Hsp70 knockdown, HuH-7 cells were transfected with ON-TARGETplus Human HSPA1A (3303) siRNA SMARTpool or nonspecific siRNAs (Non-targeting Pool) (Dharmacon, Bioportugal, Porto, Portugal). Cells in suspension were transfected using the ScreenFectA reagent and seeded immediately [44].

4.4.3. SRB Assay

5.0×10^3 (HuH-7, NCI-H1299) or 1.0×10^4 (HCC1419, HFF-1) cells/well were seeded in 96-well plates and allowed to adhere overnight, followed by treatment with serial dilutions of compounds. Cell proliferation was measured as described [45]. IC₅₀ values were determined using the GraphPad Prism software v7.0 (La Jolla, CA, USA). In combination therapy assays, combination index (CI) values were determined using the CompuSyn software v1.0 (ComboSyn, Inc., Paramus, NJ, USA) [46,47].

4.4.4. Colony Formation Assay

2.0×10^3 HuH-7 cells/well were seeded in 6-well plates and immediately treated with 0.88–28 μM SLMP53-2. Colonies were fixed and stained after 14 days, as described [47]. Colonies with more than 20 cells were counted.

4.5. Cell Cycle and Apoptosis Analysis

1.5×10^5 HuH-7 cells/well were seeded in 6-well plates and allowed to adhere overnight, followed by treatment with 14 or 28 μM SLMP53-2 or DMSO for 48 h (cell cycle) or 72 h (apoptosis). Cell cycle and apoptosis were analyzed as described [45], using the Accuri™ C6 flow cytometer and the BD Accuri C6 software (BD Biosciences, Enzifarma, Porto, Portugal). FlowJo v10.0.7 (Treestar, Ashland, OR, USA) was used for quantification of cell cycle phases.

4.6. Western Blot

1.5×10^5 HuH-7 or NCI-H1299 cells/well were seeded in 6-well plates and allowed to adhere overnight, followed by treatment with 14 μM SLMP53-2. Sample preparation and western blot were performed as described [48]. Signal detection was carried out using the ECL Prime Amersham kit (GE Healthcare, VWR, Carnaxide, Portugal) and the ChemiDoc™ MP Imaging System (Bio-Rad Laboratories, Amadora, Portugal). Whole blot images (Figure S12) and blot quantifications (Table S7) are provided in supplementary material.

4.7. IP and co-IP

2×10^6 HuH-7 cells were seeded in 75 cm^2 flasks, allowed to adhere overnight, followed by 36 h treatment with 28 or 42 μM SLMP53-2 or DMSO. The Pierce Classic Magnetic IP/Co-IP Kit (Thermo Scientific, Dagma, Carcavelos, Portugal) was used according to manufacturer's instructions. For IP, 1 $\mu\text{g}/\text{mL}$ PAb1620 (wt/folded) or PAb240 (mut/unfolded) conformation-specific anti-p53 antibodies were used. For Co-IP, 1 $\mu\text{g}/\text{mL}$ anti-p53 antibody was used. Hsp40/Hsp70/Hsp90, p53, and GAPDH (loading control) were detected by western blot, in immunoprecipitated fractions and whole cell lysates (input), as described above.

4.8. RNA Extraction and RT-qPCR

1.5×10^5 HuH-7 cells/well were seeded in 6-well plates and allowed to adhere overnight, followed by 24 h treatment with 14 or 28 μM SLMP53-2 or DMSO.

4.8.1. Gene Expression Analysis

Total RNA extraction and RT-qPCR were performed as described [49], using specific primers for each analyzed gene (Table S6) (Eurofins, MWG, Milan, Italy); GAPDH and B2M were used as reference genes.

4.8.2. miRNA Analysis

Total RNA was extracted using TRIzol reagent (Invitrogen, Carlsbad, CA, USA) according to manufacturer's instructions. RNA concentration and purity were measured in NanoDrop™ 1000 (Thermo Fisher Scientific, Waltham, MA, USA). 260/280 nm and 260/230 nm ratios ranged around 1.8–2.2. RNA integrity was

assessed by gel electrophoresis. miRNA levels were evaluated using TaqMan miRNA assays (Applied Biosystems, Foster City, CA, USA). cDNA was synthesized (MyCycler Thermal Cycler, Bio-Rad) using RNA, TaqMan MicroRNA Reverse Transcription Kit (Applied Biosystems) and stem-loop Reverse Transcription primers (hsa-miR-34a-5p; Applied Biosystems). qPCR reactions were performed in CFX96 Touch™ Real-Time PCR Detection System (Bio-Rad) using cDNA, miR-34a or snRNA U6 TaqMan probes (Applied Biosystems) and SsoAdvanced™ Universal Probes Supermix (Bio-Rad, Hercules, CA, USA). snRNA U6 was used as reference gene. Relative expression levels were calculated using the quantification cycle (Cq) method, according to MIQE guidelines [50].

4.9. *ChIP*

1.5×10^6 HuH-7 cells were seeded in 150 mm dishes and allowed to adhere overnight, followed by 24 h treatment with 28 μ M SLMP53-2 or DMSO. ChIP protocol was performed as described [51]. p53 occupancy at the p21 promoter was measured by RT-qPCR (primers are listed in Table S6).

4.10. *Microarray Experiments*

2.0×10^6 HuH-7 cells were seeded in 6-well plates and allowed to adhere overnight, followed by 24 h treatment with 28 or 42 μ M SLMP53-2 or DMSO. Total RNA was extracted using Illustra™ RNAspin Mini (GE Healthcare, Chicago, IL, USA), purity and concentration were measured by Nanodrop and Agilent 2100 Bioanalyzer (Agilent Technologies, Santa Clara, CA, USA). Samples with RIN (RNA integrity number) ≥ 8 were used for the one-Color Microarray-Based Gene Expression Analysis protocol (Agilent Technologies, Santa Clara, CA, USA) and hybridized on Agilent-014850 4x44K Whole Human Genome Microarrays. Slides were scanned on the Agilent DNA Microarray Scanner (G2505C) using the Agilent HD_GX_1Color Profile of Agilent ScanControl v8.1.3 (Agilent Technologies, Santa Clara, CA, USA). Four biological replicates per treatment were prepared and analyzed. Microarray data have been deposited in Gene Expression Omnibus database (GSE124021). The scanned TIFF images were analyzed numerically and background-corrected using the Agilent Feature Extraction Software v10.7.7.1 (Agilent Technologies, Santa Clara, CA, USA), according to the Agilent GE1_107_Sep09 standard protocol. The output of Feature Extraction was analyzed with the R software environment for statistical computing (<http://www.r-project.org/>) and the Bioconductor packages (<http://www.bioconductor.org/>). The array Quality Metrics package was used to check the quality of the arrays. Low signal Agilent probes, identified by a repeated “not detected” flag across the majority of the arrays in every condition, were filtered out from the analysis. Signal intensities across arrays were background corrected (Edwards method) and normalized with the quantile normalization method. DEGs were determined using a double threshold based on: (1) the magnitude of the change (fold change greater than ± 2); (2) the statistical significance of the change, measured with a multiple-test-correction adjusted *p*-value less than 0.05 using limma package. The IPA (v2017) resource was used for enrichment analysis of the transcriptome DEGs lists. The IPA Ontologies are derived from manually curated collections of experimental data and are utilized to infer functional enrichment of different type of relationships. The significance of gene list over-representations was determined using a Fisher exact *p*-value threshold of 0.05 with multiple-test-correction. In particular, the bio-functions and the up-stream regulators analysis were used. The graphical representation of the IPA results was performed in R/Bioconductor environment.

4.11. *Immunofluorescence*

Immunofluorescence staining of HuH-7 cells was performed basically as described [52].

4.11.1. XBP1 Staining

HuH-7 cells were seeded in 24-well plates at 1.5×10^5 cells/well density and allowed to adhere overnight, followed by 24 h treatment with 28 μM SLMP53-2 or DMSO. After treatments, cells were fixed with 4% formaldehyde/PBS for 20 min at room temperature (RT), were blocked with BSA 5% and Triton 0.1% for 1h at RT, incubated with anti-XBP1 antibody overnight at 4 °C, followed by incubation with an Alexa Fluor 488-conjugated secondary antibody for 1 h at RT, and staining with Hoechst (ThermoFisher Scientific, Waltham, MA, USA; 1:10,000). Images were visualized with a Zeiss Axio Observer Z1 microscope (Carl Zeiss, Oberkochen, Germany) using Zeiss AxioVision v4.8.1. Nuclear signal was quantified using CellProfiler™ software v3.1.5 (Broad Institute, Cambridge, MA, USA).

4.11.2. PAb240/PAb1620 Staining

HuH-7 cells were seeded in chambered cell culture slides at 1×10^4 cells/well density and allowed to adhere overnight, followed by 36 h treatment with 42 μM SLMP53-2 or DMSO. After treatment, the cell monolayer was fixed with 4% formaldehyde/PBS for 30 min at RT, permeabilized with 0.1% Triton for 20 min at 4 °C, blocked with 5% BSA for 1h at RT, incubated with PAb240, PAb1620, or DO-1 anti-p53 antibodies overnight at 4 °C, followed by incubation with Alexa Fluor 488-conjugated secondary antibody for 1h at RT, and staining with DAPI. Cells were photographed (Nikon DS-5Mc camera; Nikon Eclipse E400 fluorescence microscope; Nikon ACT-2U software, Izasa, Carnaxide, Portugal).

4.12. *HSQC-NMR*

The stabilized DBD of the mutp53-Y220C (T-p53C-Y220C) was expressed and purified as described [29]. For expression of its ^{15}N -labeled form, M9 minimal medium with $^{15}\text{NH}_4\text{Cl}$ (1 g/L) as sole nitrogen source was used. ^1H - ^{15}N HSQC spectra of ^{15}N -labeled T-p53C-Y220C (70 μM) and different compound concentrations were recorded and analyzed as described [29]. Briefly, the spectra were recorded at 293 K on a Bruker Avance-800 spectrometer using a 5-mm inverse cryogenic probe. Compound samples were mixed with protein immediately before the NMR measurement. Analysis of spectra was performed using Sparky 3.11430 (San Francisco, CA, USA) and Bruker Topspin 2.0 software (Coventry, UK).

4.13. *In Vivo Anti-Tumor and Toxicity Assays*

All animal experiments were conducted following the EU Directive 2010/63/EU and National Authorities. The study was approved by the local Animal Welfare Body (Ref. ORBEA-5-2016). Swiss nude mice (CharlesRiver

Laboratories, Barcelona, Spain) were housed under pathogen-free conditions in ventilated cages. 7.5×10^6 HuH-7 cells (in PBS/Matrigel 1:1; Corning, Enzifarma, Porto, Portugal) were subcutaneously inoculated in the dorsal flank of female Swiss nude mice (five animals/group). Tumors were routinely measured using a caliper for calculation of tumor volume by the formula $(a \times b^2)/2$ (a and b represent the longest and shortest tumor axes, respectively). Twice-weekly intraperitoneal injections of 50 mg/kg SLMP53-2 or vehicle were started for tumors with approximately 100 mm^3 (5 days after the grafts). Five administrations were performed with continuous monitoring of tumor volume, animal weight, and signs of morbidity. At the end of treatment, animals were sacrificed by cervical dislocation. For toxicity assays, female Wistar rats were treated with 50 mg/kg SLMP53-2 or vehicle (DMSO) by intraperitoneal injection, twice a week. After five administrations, blood samples were collected for toxicological analysis. Each experimental group was composed of four animals.

4.14. Immunohistochemical (IHC) Analysis

IHC of xenograft tumor tissue was performed as described [49]. Evaluation of DAB intensity and quantification were performed using ImageJ v1.8.0. (Madison, WI, USA).

4.15. Statistical Analysis

Data were statistically analyzed using the GraphPad Prism software v7.0 (GraphPad Inc., La Jolla, CA, USA). Appropriate statistical tests were applied to each dataset; $p < 0.05$ was considered statistically significant.

5. Conclusions

The present work brings a new mutp53-reactivating compound with a distinct mechanism of action from those currently reported. Notably, SLMP53-2 may also represent a new hope in cancer treatment, either alone or in combination therapy, particularly against HCC. In addition, it represents a lead compound and therefore a valuable starting material for new optimized derivatives. In fact, this work highlights the tryptophanol-derived oxazoloisindolinones as a promising chemical family for the development of more effective anticancer therapeutic options by targeting a larger set of mutp53 forms.

6. Patents

The compound SLMP53-2 is protected under an international patent (European patent EP3013833 and US patent 20160347765).

Supplementary Materials: The following are available online at <http://www.mdpi.com/2072-6694/11/8/1151/s1>, Figure S1: Clustering analysis of the microarray data, Figure S2: Microarray data analysis related to Figure 2, Figure S3: Connectivity map results, Figure S4: Representative images of XBP1 immunofluorescence in HuH-7 cells treated with 28 μM SLMP53-2 or DMSO for 24 h, Figure S5: Protein levels of p53 target genes in HCC1419 cells, after 24 h (KILLER) or 48 h (MDM2, p21, survivin, and VEGF) treatment with 14 μM SLMP53-2, Figure S6: Representative images of p53 immunofluorescence

staining of HuH-7 cells treated with 42 μ M SLMP53-2 or DMSO for 36 h, Figure S7: Overlay of $^1\text{H}/^{15}\text{N}$ -HSQC NMR spectra of T-p53C-Y220C with varying concentrations of SLMP53-2, showing no significant chemical shift, Figure S8: Western blot analysis of Hsp70 protein levels in HuH7 cells transfected with sipHsp70 or siCTRL, Figure S9: ^1H NMR and ^{13}C NMR data for SLMP53-2, Figure S10: Concentration-response curves for SLMP53-2 in (A) HCT116 p53^{+/+}, HCT116 p53^{-/-}, and (B) HepG2 cells, analyzed by SRB assay after 48h treatment with 3.12–50 μ M SLMP53-2, Figure S11: Co-immunoprecipitation of Hsp70 with p53 in HuH-7 cells treated with 34 and 68 μ M SLMP53-1 or DMSO for 36 h, using anti-p53 antibody (DO-1), followed by immunoblotting with anti-Hsp70 and anti-p53 antibodies, Figure S12: Whole blots.

Table S1: Gene expression data (see Table S1.xlsx file), Table S2: Ontology, Pathways and Upstream Regulators analyses by Ingenuity Pathway and Metascape (see Table S2.xlsx file), Table S3: Connectivity Map results by Ingenuity Pathway analysis of the microarray data (see Table S3.xlsx file), Table S4: Biochemical and haematological data of SLMP53-2 in Wistar rats, Table S5: List of antibodies used in western blot (WB), immunofluorescence (IF), immunohistochemistry, and immunoprecipitation, Table S6: List of primers, Table S7: Quantification of western blots.

Author Contributions: Conceptualization, A.I., M.M.M.S. and L.S.; formal analysis, S.G., B.B., A.B., M.I.A., S.P., A.I.; investigation, S.G., B.B., J.B.L., H.R., L.R., J.S., N.N., V.B., C.O., A.B., M.R.B., J.P.B., M.I.A., S.P., C.G., F.R.;

Resources, C.G., F.R., A.R.F., L.D., M.I.A., A.I., M.M.M.S., L.S.; writing—original draft preparation, S.G., L.S.;

Writing—review and editing, S.G., B.B., J.B.L., H.R., L.R., J.S., N.N., V.B., L.D., C.O., A.B., S.P., M.R.B., J.P.B., M.I.A.,

C.G., F.R., A.R.F., A.I., M.M.M.S., L.S.; funding acquisition, A.I., M.M.M.S., L.S.; project administration, L.S.

Funding: This work was supported by National Funds through Fundação para a Ciência e Tecnologia, I.P. via the projects UID/QUI/50006/2019 and PTDC/QUI-QOR/29664/2017.

Acknowledgments: Authors acknowledge the financial support from European Union (FEDER funds POCI/01/0145/FEDER/007728 through Programa Operacional Factores de Competitividade—COMPETE) and National Funds (FCT/MEC, Fundação para a Ciência e Tecnologia and Ministério da Educação e Ciência) under the Partnership Agreement UID/DTP/04138/2019 (iMed.Ulisboa), UID/NEU/04539/2013, UID/NEU/04539/2019.CENTRO-01-0145-FEDER-000012-HealthyAging2020, UID/BIO/04469/2019, BioTecNorte operation (NORTE-01-0145-FEDER-000004), and the projects (3599-PPCDT) PTDC/DTP-FTO/1981/2014—POCI-01-0145-FEDER-016581, and POCI-01-0145-FEDER-028736. We also thank FCT for the financial support through the grant CEECIND/01772/2017 (M. M. M. Santos), and fellowships SFRH/BD/96189/2013 (S. Gomes), PD/BD/143126/2019 (V. Barcherini), SFRH/BD/117949/2016 (L. Raimundo), SFRH/BD/119144/2016 (H. Ramos), SFRH/BD/128673/2017 (J. B. Loureiro), and the Programa Operacional Potencial Humano (POCH), specifically the BiotechHealth Programme (Doctoral Programme on Cellular and Molecular Biotechnology Applied to Health Sciences; PD/00016/2012). We also acknowledge the support from the Italian Association for Cancer Research, AIRC (IG#18985 to AI).

Conflicts of Interest: One international patent protecting the compound disclosed in this manuscript has been filed by the following authors S.G., J.S.,

M.M.M.S, and L.S. The funders had no role in the design of the study; in the collection, analyses, or interpretation of data; in the writing of the manuscript, or in the decision to publish the results. The other authors declare no conflict of interest.

References

1. Kasthuber, E.R.; Lowe, S.W. Putting p53 in Context. *Cell* **2017**, *170*, 1062–1078. [[CrossRef](#)]
2. Schulz-Heddergott, R.; Moll, U.M. Gain-of-Function (GOF) Mutant p53 as Actionable Therapeutic Target. *Cancers* **2018**, *10*, 188. [[CrossRef](#)] [[PubMed](#)]
3. Joerger, A.C.; Fersht, A.R. Structure-function-rescue: The diverse nature of common p53 cancer mutants. *Oncogene* **2007**, *26*, 2226–2242. [[CrossRef](#)] [[PubMed](#)]
4. Lopes, E.A.; Gomes, S.; Saraiva, L.; Santos, M. Small Molecules Targeting Mutant P53: A Promising Approach for Cancer Treatment. *Curr. Med. Chem.* **2018**. [[CrossRef](#)] [[PubMed](#)]
5. Bykov, V.J.N.; Eriksson, S.E.; Bianchi, J.; Wiman, K.G. Targeting mutant p53 for efficient cancer therapy. *Nat. Rev. Cancer* **2018**, *18*, 89–102. [[CrossRef](#)] [[PubMed](#)]
6. Ferlay, J.; Ervik, M.; Lam, F.; Colombet, M.; Mery, L.; Piñeros, M.; Znaor, A.; Soerjomataram, I.; Bray, F. *Global Cancer Observatory: Cancer Today*; International Agency for Research on Cancer: Lyon, France, 2018; Available online: <https://gco.iarc.fr/today> (accessed on 4 February 2019).
7. Nouredin, M.; Rinella, M.E. Nonalcoholic Fatty liver disease, diabetes, obesity, and hepatocellular carcinoma. *Clin. Liver Dis.* **2015**, *19*, 361–379. [[CrossRef](#)]
8. Vogel, A.; Cervantes, A.; Chau, I.; Daniele, B.; Llovet, J.; Meyer, T.; Nault, J.C.; Neumann, U.; Rieke, J.; Sangro, B.; et al. Hepatocellular carcinoma: ESMO Clinical Practice Guidelines for diagnosis, treatment and follow-up. *Ann. Oncol.* **2018**, *29*, iv238–iv255. [[CrossRef](#)]
9. Lin, S.; Hoffmann, K.; Schemmer, P. Treatment of hepatocellular carcinoma: A systematic review. *Liver Cancer* **2012**, *1*, 144–158. [[CrossRef](#)]
10. Bevant, K.; Coulouarn, C. Landscape of genomic alterations in hepatocellular carcinoma: Current knowledge and perspectives for targeted therapies. *Hepatobiliary Surg. Nutr.* **2017**, *6*, 404–407. [[CrossRef](#)]
11. Comprehensive and Integrative Genomic Characterization of Hepatocellular Carcinoma. *Cell* **2017**, *169*, 1327–1341. [[CrossRef](#)]
12. Soares, J.; Raimundo, L.; Pereira, N.A.; Monteiro, A.; Gomes, S.; Bessa, C.; Pereira, C.; Queiroz, G.; Bisio, A.; Fernandes, J.; et al. Reactivation of wild-type and mutant p53 by tryptophan-derived oxazoloisoindolinone SLMP53-1, a novel anticancer small-molecule. *Oncotarget* **2016**, *7*, 4326–4343. [[CrossRef](#)] [[PubMed](#)]

13. Boeckler, F.M.; Joerger, A.C.; Jaggi, G.; Rutherford, T.J.; Veprintsev, D.B.; Fersht, A.R. Targeted rescue of a destabilized mutant of p53 by an in silico screened drug. *Proc. Natl. Acad. Sci. USA* **2008**, *105*, 10360–10365. [[CrossRef](#)] [[PubMed](#)]
14. Yogosawa, S.; Yoshida, K. Tumor suppressive role for kinases phosphorylating p53 in DNA damage-induced apoptosis. *Cancer Sci.* **2018**, *109*, 3376–3382. [[CrossRef](#)] [[PubMed](#)]
15. Niessner, H.; Sinnberg, T.; Kosnopfel, C.; Smalley, K.S.M.; Beck, D.; Praetorius, C.; Mai, M.; Beissert, S.; Kulms, D.; Schaller, M.; et al. BRAF Inhibitors Amplify the Proapoptotic Activity of MEK Inhibitors by Inducing ER Stress in NRAS-Mutant Melanoma. *Clin. Cancer Res.* **2017**, *23*, 6203–6214. [[CrossRef](#)] [[PubMed](#)]
16. Raver-Shapira, N.; Marciano, E.; Meiri, E.; Spector, Y.; Rosenfeld, N.; Moskovits, N.; Bentwich, Z.; Oren, M. Transcriptional activation of miR-34a contributes to p53-mediated apoptosis. *Mol. Cell* **2007**, *26*, 731–743. [[CrossRef](#)] [[PubMed](#)]
17. Liu, T.; Laurell, C.; Selivanova, G.; Lundeberg, J.; Nilsson, P.; Wiman, K.G. Hypoxia induces p53-dependent transactivation and Fas/CD95-dependent apoptosis. *Cell Death Differ.* **2007**, *14*, 411–421. [[CrossRef](#)] [[PubMed](#)]
18. Ohoka, N.; Yoshii, S.; Hattori, T.; Onozaki, K.; Hayashi, H. TRB3, a novel ER stress-inducible gene, is induced via ATF4-CHOP pathway and is involved in cell death. *EMBO J.* **2005**, *24*, 1243–1255. [[CrossRef](#)]
19. Riley, T.; Sontag, E.; Chen, P.; Levine, A. Transcriptional control of human p53-regulated genes. *Nat. Rev. Mol. Cell Biol.* **2008**, *9*, 402–412. [[CrossRef](#)]
20. Di Como, C.J.; Prives, C. Human tumor-derived p53 proteins exhibit binding site selectivity and temperature sensitivity for transactivation in a yeast-based assay. *Oncogene* **1998**, *16*, 2527–2539. [[CrossRef](#)]
21. Hainaut, P.; Milner, J. Interaction of heat-shock protein 70 with p53 translated in vitro: Evidence for interaction with dimeric p53 and for a role in the regulation of p53 conformation. *EMBO J.* **1992**, *11*, 3513–3520. [[CrossRef](#)]
22. Walerych, D.; Olszewski, M.B.; Gutkowska, M.; Helwak, A.; Zylicz, M.; Zylicz, A. Hsp70 molecular chaperones are required to support p53 tumor suppressor activity under stress conditions. *Oncogene* **2009**, *28*, 4284–4294. [[CrossRef](#)] [[PubMed](#)]
23. Wawrzynow, B.; Zylicz, A.; Zylicz, M. Chaperoning the guardian of the genome. The two-faced role of molecular chaperones in p53 tumor suppressor action. *Biochim. Biophys. Acta Rev. Cancer* **2018**, *1869*, 161–174. [[CrossRef](#)] [[PubMed](#)]
24. Giknis, M.; Clifford, C.B. *Clinical Laboratory Parameters for CRL: WI (Han)*; Charles River Laboratories: Wilmington, MA, USA, 2008.
25. Kim, I.; Xu, W.; Reed, J.C. Cell death and endoplasmic reticulum stress: Disease relevance and therapeutic opportunities. *Nat. Rev. Drug Discov.* **2008**, *7*, 1013–1030. [[CrossRef](#)] [[PubMed](#)]
26. Gorrini, C.; Harris, I.S.; Mak, T.W. Modulation of oxidative stress as an

- anticancer strategy. *Nat. Rev. Drug Discov.* **2013**, *12*, 931–947. [[CrossRef](#)] [[PubMed](#)]
27. Mahalingam, D.; Wilding, G.; Denmeade, S.; Sarantopoulos, J.; Cosgrove, D.; Cetnar, J.; Azad, N.; Bruce, J.; Kurman, M.; Allgood, V.E.; et al. Mipsagargin, a novel thapsigargin-based PSMA-activated prodrug: Results of a first-in-man phase I clinical trial in patients with refractory, advanced or metastatic solid tumours. *Br. J. Cancer* **2016**, *114*, 986–994. [[CrossRef](#)]
28. Yang, P.M.; Lin, Y.T.; Shun, C.T.; Lin, S.H.; Wei, T.T.; Chuang, S.H.; Wu, M.S.; Chen, C.C. Zebularine inhibits tumorigenesis and stemness of colorectal cancer via p53-dependent endoplasmic reticulum stress. *Sci. Rep.* **2013**, *3*, 3219. [[CrossRef](#)]
29. Bauer, M.R.; Joerger, A.C.; Fersht, A.R. 2-Sulfonylpyrimidines: Mild alkylating agents with anticancer activity toward p53-compromised cells. *Proc. Natl. Acad. Sci. USA* **2016**, *113*, E5271–E5280. [[CrossRef](#)]
30. Lambert, J.M.; Moshfegh, A.; Hainaut, P.; Wiman, K.G.; Bykov, V.J. Mutant p53 reactivation by PRIMA-1MET induces multiple signaling pathways converging on apoptosis. *Oncogene* **2010**, *29*, 1329–1338. [[CrossRef](#)]
31. Liu, J.L.; Zhang, X.J.; Zhang, Z.; Zhang, A.H.; Wang, W.; Dong, J.H. Meta-analysis: Prognostic value of survivin in patients with hepatocellular carcinoma. *PLoS ONE* **2013**, *8*, e83350. [[CrossRef](#)]
32. Jin, Y.; Chen, J.; Feng, Z.; Fan, W.; Wang, Y.; Li, J.; Tong, D. The expression of Survivin and NF-kappaB associated with prognostically worse clinicopathologic variables in hepatocellular carcinoma. *Tumour Biol.* **2014**, *35*, 9905–9910. [[CrossRef](#)]
33. Su, C. Survivin in survival of hepatocellular carcinoma. *Cancer Lett.* **2016**, *379*, 184–190. [[CrossRef](#)] [[PubMed](#)]
34. Slabakova, E.; Culig, Z.; Remsik, J.; Soucek, K. Alternative mechanisms of miR-34a regulation in cancer. *Cell Death Dis.* **2017**, *8*, e3100. [[CrossRef](#)] [[PubMed](#)] Li, N.; Fu, H.; Tie, Y.; Hu, Z.; Kong, W.; Wu, Y.; Zheng, X. miR-34a inhibits migration and invasion by down-regulation of c-Met expression in human hepatocellular carcinoma cells. *Cancer Lett.* **2009**, *275*, 44–53. [[CrossRef](#)] [[PubMed](#)]
35. Daige, C.L.; Wiggins, J.F.; Priddy, L.; Nelligan-Davis, T.; Zhao, J.; Brown, D. Systemic delivery of a miR34a mimic as a potential therapeutic for liver cancer. *Mol. Cancer Ther.* **2014**, *13*, 2352–2360. [[CrossRef](#)] [[PubMed](#)]
36. Beg, M.S.; Brenner, A.J.; Sachdev, J.; Borad, M.; Kang, Y.K.; Stoudemire, J.; Smith, S.; Bader, A.G.; Kim, S.; Hong, D.S. Phase I study of MRX34, a liposomal miR-34a mimic, administered twice weekly in patients with advanced solid tumors. *Investig. New Drugs* **2017**, *35*, 180–188. [[CrossRef](#)]
37. Hiraki, M.; Hwang, S.Y.; Cao, S.; Ramadhar, T.R.; Byun, S.; Yoon, K.W.; Lee, J.H.; Chu, K.; Gurkar, A.U.; Kolev, V.; et al. Small-Molecule Reactivation of Mutant p53 to Wild-Type-like p53 through the p53-Hsp40 Regulatory Axis. *Chem. Biol.* **2015**, *22*, 1206–1216. [[CrossRef](#)] [[PubMed](#)]

38. Polireddy, K.; Singh, K.; Pruski, M.; Jones, N.C.; Manisundaram, N.V.; Ponnella, P.; Ouellette, M.; Van Buren, G.; Younes, M.; Bynon, J.S.; et al. Mutant p53(R175H) promotes cancer initiation in the pancreas by stabilizing HSP70. *Cancer Lett.* **2019**, *453*, 122–130. [[CrossRef](#)]
39. Raoul, J.L.; Gilabert, M.; Adhoute, X.; Edeline, J. An in-depth review of chemical angiogenesis inhibitors for treating hepatocellular carcinoma. *Expert Opin. Pharm.* **2017**, *18*, 1467–1476. [[CrossRef](#)]
40. Kudo, M. Systemic Therapy for Hepatocellular Carcinoma: 2017 Update. *Oncology* **2017**, *93* (Suppl. S1), 135–146. [[CrossRef](#)]
41. Pereira, N.A.; Monteiro, A.; Machado, M.; Gut, J.; Molins, E.; Perry, M.J.; Dourado, J.; Moreira, R.; Rosenthal, P.J.; Prudencio, M.; et al. Enantiopure Indolizinoindolones with in vitro Activity against Blood- and Liver-Stage Malaria Parasites. *Chem. Med. Chem.* **2015**, *10*, 2080–2089. [[CrossRef](#)]
42. Baud, M.G.J.; Bauer, M.R.; Verduci, L.; Dingler, F.A.; Patel, K.J.; Horil Roy, D.; Joerger, A.C.; Fersht, A.R. Aminobenzothiazole derivatives stabilize the thermolabile p53 cancer mutant Y220C and show anticancer activity in p53-Y220C cell lines. *Eur. J. Med. Chem.* **2018**, *152*, 101–114. [[CrossRef](#)] [[PubMed](#)]
43. Gomes, S.; Raimundo, L.; Soares, J.; Loureiro, J.B.; Leao, M.; Ramos, H.; Monteiro, M.N.; Lemos, A.; Moreira, J.; Pinto, M.; et al. New inhibitor of the TAp73 interaction with MDM2 and mutant p53 with promising antitumor activity against neuroblastoma. *Cancer Lett.* **2019**, *446*, 90–102. [[CrossRef](#)] [[PubMed](#)]
44. Soares, J.; Raimundo, L.; Pereira, N.A.; dos Santos, D.J.; Perez, M.; Queiroz, G.; Leao, M.; Santos, M.M.; Saraiva, L. A tryptophanol-derived oxazolopiperidone lactam is cytotoxic against tumors via inhibition of p53 interaction with murine double minute proteins. *Pharmacol. Res.* **2015**, *95–96*, 42–52. [[CrossRef](#)] [[PubMed](#)]
45. Chou, T.-C.; Talalay, P. Quantitative analysis of dose-effect relationships: The combined effects of multiple drugs or enzyme inhibitors. *Adv. Enzym. Regul.* **1984**, *22*, 27–55. [[CrossRef](#)]
46. Raimundo, L.; Espadinha, M.; Soares, J.; Loureiro, J.B.; Alves, M.G.; Santos, M.M.M.; Saraiva, L. Improving anticancer activity towards colon cancer cells with a new p53-activating agent. *Br. J. Pharm.* **2018**, *175*, 3947–3962. [[CrossRef](#)] [[PubMed](#)]
47. Soares, J.; Pereira, N.A.; Monteiro, A.; Leao, M.; Bessa, C.; Dos Santos, D.J.; Raimundo, L.; Queiroz, G.; Bisio, A.; Inga, A.; et al. Oxazoloisindolinones with in vitro antitumor activity selectively activate a p53-pathway through potential inhibition of the p53-MDM2 interaction. *Eur. J. Pharm. Sci.* **2015**, *66*, 138–147. [[CrossRef](#)] [[PubMed](#)]
48. Soares, J.; Espadinha, M.; Raimundo, L.; Ramos, H.; Gomes, A.S.; Gomes, S.; Loureiro, J.B.; Inga, A.; Reis, F.; Gomes, C.; et al. DIMP53-1: A novel small-molecule dual inhibitor of p53-MDM2/X interactions with multifunctional p53-dependent anticancer properties. *Mol. Oncol.* **2017**, *11*, 612–627. [[CrossRef](#)] [[PubMed](#)]

49. Bustin, S.A.; Benes, V.; Garson, J.A.; Hellemans, J.; Huggett, J.; Kubista, M.; Mueller, R.; Nolan, T.; Pfaffl, M.W.; Shipley, G.L.; et al. The MIQE guidelines: Minimum information for publication of quantitative real-time PCR experiments. *Clin. Chem.* **2009**, *55*, 611–622. [[CrossRef](#)]
50. Alessandrini, F.; Pezze, L.; Menendez, D.; Resnick, M.A.; Ciribilli, Y. ETV7-Mediated DNJC15 Repression Leads to Doxorubicin Resistance in Breast Cancer Cells. *Neoplasia* **2018**, *20*, 857–870. [[CrossRef](#)]
51. Vazquez, C.; Beachboard, D.C.; Horner, S.M. Methods to Visualize MAVS Subcellular Localization. *Methods Mol. Biol.* **2017**, *1656*, 131–142. [[CrossRef](#)]

© 2019 by the authors. Licensee MDPI, Basel, Switzerland. This article is an open access article distributed under the terms and conditions of the Creative Commons Attribution (CC BY) license (<http://creativecommons.org/licenses/by/4.0/>).



MANIO: Mechanism of wild-type and mutant p53 activation and therapeutic potential in colorectal cancer

*Ramos H, Soares MI, Raimundo L, Silva J, Gomes C, Reis F, Monteiro F, Nunes C, Reis S, Chlapek P, Veselska R, Dmingues L, **Bosco B**, Piazza S, Inga A, Pinho e Melo MVDT, Saraiva L*

***In revision on Cell Reports**

In this study, also developed as a collaboration with the Saraiva group, I analyzed a newly synthesized molecule called MANIO and its effect in p53 activation. In detail, MANIO was tested on a number of cancer cell lines comprising p53 wild type and mutant, and it showed a markedly lower IC₅₀ compared to p53-null cells. MANIO treatment activated cell cycle arrest and apoptosis. Indeed, we showed that this molecule engages a p53-dependent response in HCT116 cells and that its effects persist and increase over at least a 48-hour time window. Then, we established that MANIO binds the DNA-binding domain restoring p53 wild-type like properties, with a higher effect in mutp53 R248W and R248Q. Interestingly, MANIO showed potent antitumor activity both in patient-derived colorectal cancer (CRC) cells and in CRC xenograft mouse models with no apparent toxic side effects. In this work our group performed, analyzed, and validated transcriptome changes induced by MANIO treatment by an RNA Sequencing experiment in HCT116 cells. The list of differentially upregulated genes confirmed that MANIO induced a p53-response signature. Instead, MANIO treatment led to the repression of many genes, which, however, lacked the expected signature of indirect p53 repression.

My contributions to this study have been: i) cell cycle and apoptosis analysis of MANIO treated HCT116 p53 wild type and p53 null cells; ii) validation of RNA Seq results by qRT-PCR at different time points; iii) analysis of DREAM complex components, that should be repressed by p53 activation; iv) studies of p53 targets up-regulation or down-regulation upon MANIO treatment at different timepoints.

This study is related to the main theme of my thesis as MANIO treatment results not only in cell cycle arrest but to significant levels of apoptosis in HCT116. This effect may be related to the finding that the p53 transcriptional network is modulated asymmetrically, in that the p21-dependent modulation of the DREAM repressive complex is lacking or much delayed. Based on the previous work performed from our laboratory, Rizzotto D et al. demonstrated that p53 activation upon Nutlin-3 treatment induces cell cycle arrest in HCT116 cells, while the same treatment leads the cells to apoptosis when DHX30 was depleted. Even if the correlation between p53 and DHX30 is still unclear, I hypothesized that DHX30 depletion could have a regulatory effect on p53. In detail, the silencing of DHX30 could increase the kinetics of p53 activation waves or reduces the threshold of p53-dependent apoptosis, enhancing cell death upon drug treatments such as Nutlin-3 and possibly also MANIO.

The small molecule MANIO activates an atypical p53-dependent transcriptional response in HCT116 cells

In an attempt to find new p53-activating agents endowed with antitumor activity, the Saraiva lab at the University of Porto has investigated the anti-proliferative activity of a small chemical library of 6,7-bis(hydroxymethyl)-1*H*,3*H*-pyrrolo[1,2-*c*] thiazoles exploiting a panel of human cancer cells with different p53 status. Based on the half-maximal inhibitory concentration (IC₅₀) values obtained for the tested compounds, the (3*S*)-6,7-bis(hydroxymethyl)-5-methyl-3-phenyl-1*H*,3*H*-pyrrolo[1,2-*c*]thiazole (herein called MANIO) was selected due to its noticeable selectivity to cancer cells expressing p53. In fact, MANIO IC₅₀ values ranged from 0.20 – 0.97 μM or 0.088 – 2.90 μM in wtp53- or mutp53-expressing cells, respectively, while it ranged between 26.20 – 48.25 μM in p53-null cells.

I performed an RNA-seq experiment in biological quadruplicates to examine the transcriptional response of HCT116 p53^{+/+} cells were treated with 1 μM MANIO (IC₅₀ concentration) for 24 hours. Cells were collected 24 hours after treatment and total RNA was extracted using the Illustra™ RNAspin Mini RNA Isolation Kit (GE Healthcare Life Sciences, Milan, Italy). RNA integrity was checked by the Agilent 2100 Bioanalyzer (Agilent Technologies), discarding preparations with RIN (RNA integrity number) values ≤8. Sequencing libraries were produced following the TruSeq RNA Library kit v2 protocol (Illumina) and using 1 μg of RNA as input. A total of eight samples, four treatment and four controls were sequenced using HiSeq 2500, obtaining ≈25M raw reads per sample. Raw sequence files were subjected to quality control analysis using FastQC (v 1.3) (<http://www.bioinformatics.babraham.ac.uk/projects/fastqc/>).

Data analysis was performed by Dr. Silvano Piazza. Transcript quantification was conducted with STAR (v2.5.3a) {Dobin, 2013} (assigned to a gene using the GENCODE annotation (v27) using the STAR function “quantMode GeneCounts”) mapped to the human genome version GRCh38 and with reference annotation. Read counts generated by STAR were analysed by using DESeq2 package for detecting genes that were differentially expressed. An adjusted p-value cut off of 0.05 was decided as threshold for detection of DEGs. Starting from the expression matrix, genes that were considered as differentially regulated, were analyzed using hierarchical clustering method (cluster function, stats package). Visualization of the clustering and heatmap of log₂-normalized counts (TMM method) were obtained gplots package. To explore the high-dimensional property of the data we used the PCA Principal Component Analysis, as dimensionality reduction algorithm implemented in stats package. For the Functional annotations analyses we used Enricher web tools. The enriched annotation table results, obtained in the web site, were then downloaded to be processed in R/bioconductor and visualized using ggplot2 package. The combined score is a combination of the logarithm of the p-value computed using the Fisher's exact test and the rank score computed using a modification to Fisher's exact test in which we compute a z-score for deviation from an expected rank.

Results indicate that MANIO treatment led to broad changes in gene expression with nearly 900 Upregulated and 500 Downregulated DEGs genes (four replicates for each treatment and DMSO control; log fold change < -1 or > 1 , multiple tests correction adjusted p-value < 0.05 ; data is deposited in GEO - GSE145482 (**Figure 2A, 2B**). Gene ontology, pathway, and upstream regulator enrichment analysis using the enrichR webtool (Kuleshov M. *et al.*, 2016) showed strong evidence for the activation of the p53-response pathway (**Figure 2C, upper panel**). Instead, the list of genes repressed by MANIO diverged from a canonical p53-dependent signature, as it was not enriched for cell proliferation, DNA repair, DNA replication, or cell division (**Figure 2C, lower panel**). Similar results were obtained using GSEA or Metascape (**Figure S2A, S2B and data not shown**). Indeed, about 65 established p53 target genes were upregulated by MANIO in the RNA-sequencing data (**Figure 2D, upper panel**). Hence, the upregulated gene signature of MANIO-treated HCT116 p53^{+/+} cells is indisputably p53-related. p53-dependent gene repression is thought to be mostly indirect and largely dependent on the modulation of the DREAM complex via p21 (Engeland K., 2018), that is induced by MANIO. Hence, we compared MANIO downregulated DEGs with an extended list of DREAM complex targets, and found a very small overlap (**Figure S2C**). However, we observed a trend for down-modulation by MANIO of several dream targets (**Figure S2D**). We then explored if the lack of a canonical p53-dependent gene repression signature could be dependent on the timepoint of our RNA-seq analysis and we followed four targets treating cells with MANIO for 16, 24, and 48 hours (**Figure S2E**). Results confirmed the RNA-seq data and showed the same trend also for the earlier time point, while the 48-hour treatment showed a trend for downregulated, paralleled by higher induction of p21. Hence, it appears that MANIO engages the p53-dependent response and its effects persists and increase over at least a 48-hour time window.

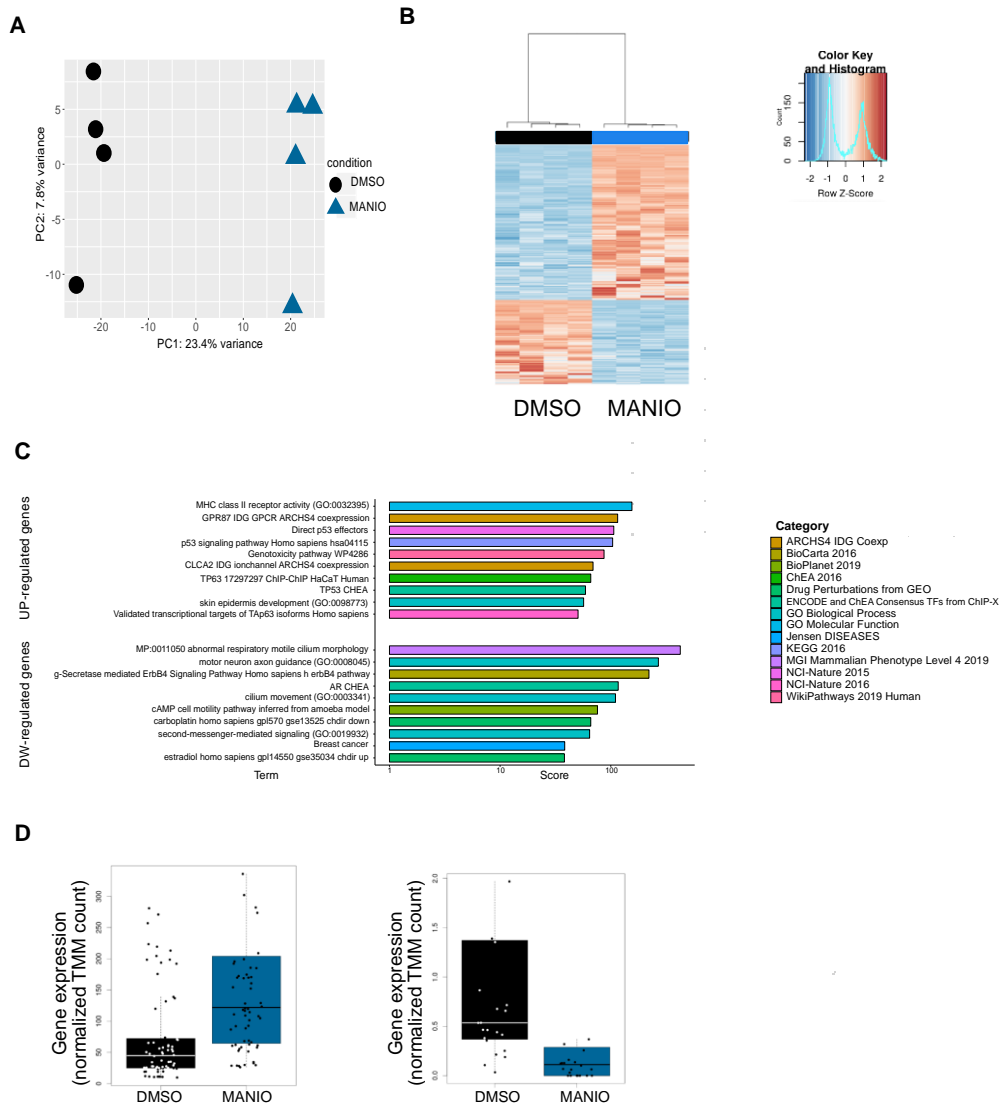


Figure 2. Gene expression profile changes in human cancer cells by MANIO reveal a p53-activation signature.

A) Principal component analysis (PCA) of the gene expression counts (log₂ normalized Trimmed Mean of M-values (TMM) method counts) showing the first versus the second principal component (PC). In the axes the percentage of the explained variance by the component is reported. Samples in the two conditions (DMSO, MANIO 1microM) are highlighted in different colors and different shapes.

B) Heatmap showing the differentially expressed genes (log Fold change < -1 or > 1, multiple tests correction adjusted p-value<0.05) in the comparison MANIO vs DMSO. Gene expression counts were normalized by the Trimmed Mean of M-values (TMM) method), hierarchically clustered with average linkage and uncentered correlation metric was applied. Two main clusters of genes were obtained: the first one is composed by the genes upregulated through the samples cluster and a second one composed by the genes downregulated.

C) Barplot graphs represent the enrichment of the biological terms based on the Combined score (x-axis), as calculated by the enrichR web tool (upper panel: Upregulated gene cluster;

bottom panel: Downregulated gene cluster). All terms have multiple tests correction adjusted p-value less than 0.05. **D**) Boxplot representations of the RNA-seq based gene expression for one element from the Upregulated gene cluster (p53 signaling pathway, top panel) and one example from the Downregulated gene cluster (bottom panel).

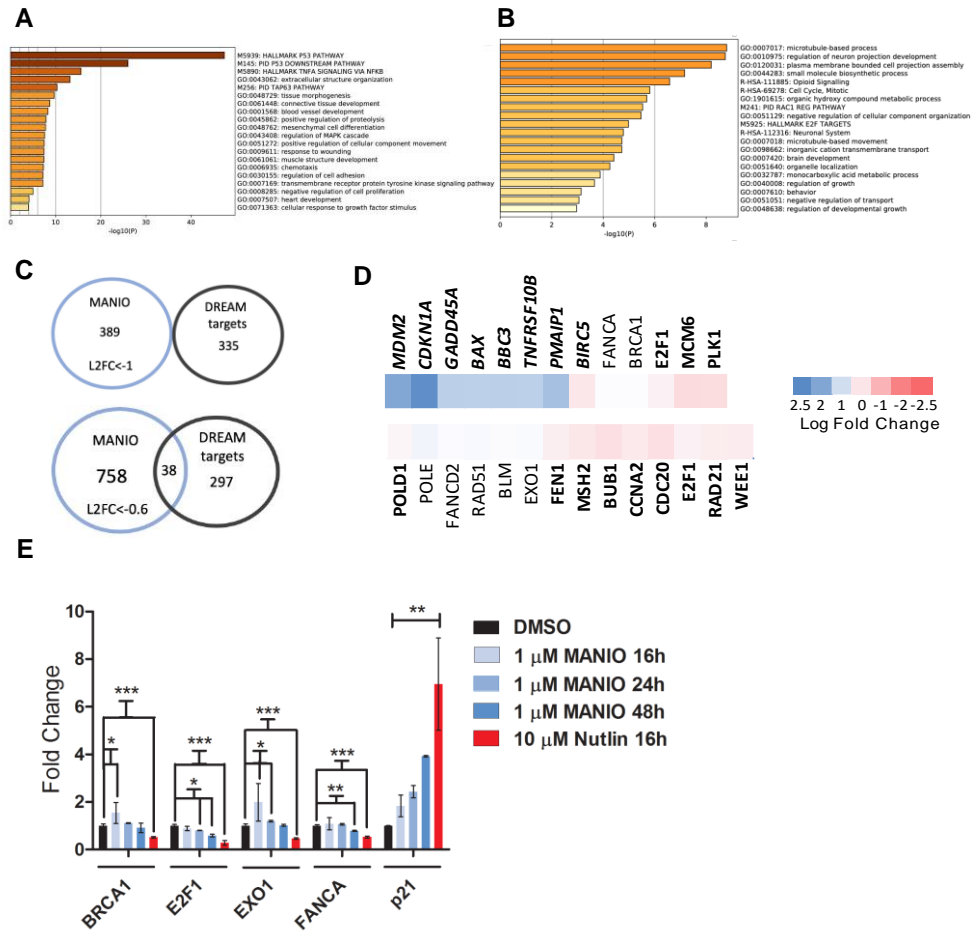


Figure S2. Pathway analysis and features of the repressed gene signature elicited by MANIO treatment in HCT116 cells.

A) Metascape results obtained with the differentially Upregulated gene list confirm that the p53 pathway signature as the most enriched semantic terms. See enrichR data presented in Figure 2. **B)** Metascape results obtained with the differentially Downregulated gene list confirm the weak enrichment for terms related to cell cycle arrest. See enrichR data presented in Figure 2. **C)** Venn Diagram comparing the list of coding genes differentially Downregulated by MANIO treatment and an established list of genes that are modulated by the DREAM complex and can thus be indirectly repressed by p53 via the modulation of p21 (Engeland K., 2018). Genes significantly repressed by MANIO selected based on $\log_2FC \leq -1$, or on $\log_2FC \leq -0.6$ were used for the comparison respectively in the upper and lower panels. **D)** Heatmap-view of the RNA-sequencing results for a selection of DREAM targets. The gene expression changes of direct p53 target genes validated in the paper are included as control (gene name italic). While few dream targets are significantly Downregulated by MANIO considering the minimum fold change threshold ($\log_2 FC < -0.6$), there is a general trend for repression that is statistically

significant for several genes (gene names in bold, adjusted p value < 0.05). **E**) Impact of MANIO treatment at different time points. qPCR data for the indicated DREAM target genes and for p21(CDKN1A) is presented as average fold change and standard deviation of three biological replicates. B2M and YWHAZ were used as reference genes. Nutlin was used as a control of non-genotoxic p53 activation. Repression of E2F1 and FANCA was apparent after 48 hours of MANIO treatment, a time point where the induction of p21 was highest.

References:

- Engeland K. Cell cycle arrest through indirect transcriptional repression by p53: I have a DREAM. *Cell Death Differ.* 2018; 25(1):114-132. doi:10.1038/cdd.2017.172
- <http://www.bioinformatics.babraham.ac.uk/projects/fastqc/>
- Kuleshov M V., Jones MR, Rouillard AD, et al. Enrichr: a comprehensive gene set enrichment analysis web server 2016 update. *Nucleic Acids Res.* 2016;44(W1):W90-W97. doi:10.1093/nar/gkw377

Other publications

- Monti P, **Bosco B**, Gomes S, Saraiva L, Fronza G, Inga A. Yeast as a chassis for developing functional assays to study human P53: background, protocols and examples. *Journal of Visualized Experiments* (2019), **150**, doi: 10.3791/59071.
- **Bosco B**, Defant A, Messina A, Incitti T, Sighel D, Bozza A, Ciribilli Y, Inga A, Casarosa S and Mancini I. Synthesis of 2,6-Diamino-Substituted Purine Derivatives and Evaluation of Cell Cycle Arrest in Breast and Colorectal Cancer Cells. *Molecules* (2018), **23**, doi:10.3390/molecules23081996.
- Dassi, E, Ferretti P, Covello G, **HTM-CMB-2015**, Bertorelli R, Denti MA, De Sanctis V, Tett A, and Segata N. The short-term impact of probiotic consumption on the oral cavity microbiome. *Scientific Reports* (2018), **8**, doi:10.1038/s41598-018-28491-x.